UNIVERSITY OF CALIFORNIA, SAN DIEGO

Study of Intense Proton Beams: Generation and Transport in Solid Density Matter

A dissertation submitted in partial satisfaction of the
requirements for the degree
Doctor of Philosophy

in

Engineering Sciences (Engineering Physics)

by

Joohwan Kim

Committee in charge:

Farhat Beg, Chair
Carlos Coimbra
Christopher McGuffey
Clifford Surko
Mark Tillack
David Tytler

2016

The dissertation of Joohwan Kim is approved, and it is acceptable in quality and form for publication on microfilm and electronically:

_____

_____

_____

_____

_____

_____

Chair

University of California, San Diego

2016

DEDICATION

To my family for being there always

TABLE OF CONTENTS

LIST OF FIGURES

LIST OF TABLES

ACKNOWLEDGEMENTS

I would first like to thank my advisor Prof. Farhat Beg for his guidance and support to reach this goal. He has generously given me opportunities to pursue interesting research through the computational method and many experiments with high-tech facilities. I also appreciate all opportunities he has given me to attend so many conferences to present and learn sciences.

I could not have completed this work without the encouragement Chris McGuffey provided. His sincere mind helped me to focus, discuss and present physics effectively. Bin Qiao gave me useful guidance to begin with simulations. I thank him for giving me the direction of computational studies.

Great thanks to Mingsheng Wei and Richard Stephens for providing me instructions from their extensive knowledge. I am grateful to Paul Grabowski, whose contribution has been valuable for papers to be published. I am especially appreciative of Harry Mclean for his support in LLNL and Scott Wilks for his encouragement and discussion about LSP simulations.

I would like to express my thanks to all my colleagues in High Energy Density Physics Group for their help and friendly atmosphere. Thanks go to Bhooshan Paradkar, Teresa Bartal, Sugreev Chawla, Derek Mariscal, Charlie Jarrott, Anna Sorokovikova, Jonathan Peebles, Gilbert Collins IV, Rohini Mishra, Christine Krauland, Julio Ahumada, Jinquing Yu, Rui Hua and Shu Zhang. I also appreciate all collaborators from various institutions for their help in many experiments.

Last but not least, to my family: my mother, father, sister and my grandmother. Thank you for your endless love.

This work was performed under the auspices of the U.S. DOE contract DE-SC0001265, DOE/NNSA National Laser User Facility program, Contract DE-NA0002034 and by the AFOSR under Contract FA9550-14-1-0346.

Chapter 3 and 5, in part, are reprints of the material as it appears in

J. Kim, B. Qiao, C. McGuffey, M. S. Wei, P. Grabowski and F. N. Beg, "Self-Consistent Simulation of Transport and Energy Deposition of Intense Laser-Accelerated Proton Beams in Solid-Density Matter", *Physical Review Letters 115, 054801 (2015)* and **J. Kim**, C. McGuffey, B. Qiao, M. S. Wei, P. Grabowski and F. N. Beg, "Varying stopping and self-focusing of intense proton beams as they heat solid density matter", *Physics of Plasmas 23, 043104 (2016).* The dissertation author was the primary investigator and author of these papers.

VITA

2003	B. E. in Electronic Electrical Engineering, Hongik University
2005	M. E. in Electrical, Information and control Engineering, Hongik University
2010-2015	Graduate Research Assistant, University of California, San Diego
2016	Ph. D. in Engineering Sciences (Engineering Physics), University of California, San Diego

PUBLICATIONS

J. Kim, C. McGuffey, B. Qiao, M. S. Wei, P. Grabowski and F. N. Beg, "Varying stopping and self-focusing of intense proton beams as they heat solid density matter", *Physics of Plasmas 23, 043104* (2016)

J. Kim, B. Qiao, C. McGuffey, M. S. Wei, P. Grabowski and F. N. Beg, "Self-consistent simulation of transport and energy deposition of intense laser accelerated proton beams in solid-density matter", *Physical Review Letters 115, 054801* (2015)

G. W. Collins IV, M. P. Valdivia, T. O. Zick, J. Kim, D. M. Haas, A. C. Forsman, R. B. Stephens, and F. N. Beg, "Investigation into the dynamics of laser-cut foil X-pinches and their potential use for high repetition rate operation", *Applied Physics Letters 105, 024101* (2014)

A. Morace, C. Bellei, T. Bartal, L. Willingale, J. Kim, A. Maksimchuk, K. Krushelnick, M. S. Wei1, P. K. Patel, D. Batani, N. Piovella, R. B. Stephens, and F. N. Beg, "Improved laser-to-proton conversion efficiency in isolated reduced mass targets", *Applied Physics Letter 103, 054102* (2013)

L. Willingale, A. G. R. Thomas, A. Maksimchuk, A. Morace, T. Bartal, J. Kim, R. B. Stephens, M. S. Wei, F. N. Beg, and K. Krushelnick, "Investigation of relativistic intensity laser generated hot electron dynamics via copper K alpha imaging and proton acceleration", *Physics of Plasmas 20, 123112* (2013)

P. A. Ni, S. M. Lund, C. McGuffey, N. Alexander, B. Aurand, J. J. Barnard, F. N. Beg, C. Bellei, F. M. Bieniosek, C. Brabetz, R. H. Cohen, J. Kim, P. Neumayer, M. Roth, and B. G. Logan, "Initial experimental evidence of self-collimation of target-normal-sheath-accelerated proton beam in a stack of conducting foils", *Physics of Plasmas 20, 083111* (2013)

G. W. Collins, D. Marsical, D. M. Haas, R. E. Madden, K. Gunasekara, J. Kim, M. L. L. Abarr, S. C. Bott, F. N. Beg and J. P. Chittenden, "Effect of the global to local magnetic field ratio on the ablation modulations on x-pinches driven by 80 kA peak current", *New journal of Physics 14, 043021* (2012)

J. L. Peebles, S. C. Bott, K. Gunasekera, J. Kim, L. Harpster, "Examination of Bow-Shock Formation in Supersonic Radiatively Cooled Plasma Flows", *IEEE transaction on Plasma Science 39, 2422* (2011)

D.M. Haas, S.C. Bott, J. Kim, D.A. Mariscal, R.E. Madden, Y. Eshaq, U. Ueda, G. Collins IV, K. Gunasekera, F.N. Beg, J.P. Chittenden, N. Niasse, C.A. Jennings, "Supersonic jet formation and propagation in x-pinches", *Astrophysics and Space Science 336, 33-40* (2011)

ABSTRACT OF THE DISSERTATION

Study of Intense Proton Beams: Generation and Transport in Solid Density Matter

by

Joohwan Kim

Doctor of Philosophy in Engineering Sciences (Engineering Physics)

University of California, San Diego, 2016

Professor Farhat Beg, Chair

Intense proton beams are appealing research subjects in high energy density physics and fast ignition of inertial confinement fusion as they are advantageous to isochoric heating and local energy deposition deep in the medium. A leading method for generation of proton beams utilizes high-power lasers to accelerate protons to energies over MeV. For applications, generation of these intense beams must be controlled, and understanding of the physics of beam transport in a new intensity regime is required. This thesis contains experimental findings, as well as computational studies, on the generation of intense proton beams and their transport in solid density matter.

Experiments were carried out to compare proton beam focusing from different target geometries irradiated by an intense laser. Compared to a free standing target, enclosed targets show a narrower and brighter K_α radiation emission spot on a foil placed behind the target, indicating higher beam focusability. Numerical simulations have confirmed that the cause of the experimentally measured focusing effect is a field on the target enclosing structures. Furthermore, the long laser pulse duration (10 ps) was beneficial to keep providing radial electric fields for beam focusing.

This thesis presents a simulation of the transport and energy deposition for such an intense proton beam in solid-density matter, where both collective effects and the individual proton slowing-down are taken into account in a self-consistent, dynamically coupled manner. To achieve this, a new proton stopping power module covering warm dense matter states has been implemented in the hybrid PIC code LSP where the proton stopping power is updated with the varying local target thermodynamic state at each simulation grid and time step.

Detailed analyses were undertaken to comprehend the collective effects taking place in these system. As an example, a self-generated magnetic field can develop during beam transport at high current density. In the case of a narrow beam, it can be strong enough to pinch the beam, leading to the local target heating up to hundreds of eV.

Finally, simulations showing consistent results with experimental data demonstrate that varying stopping power in different materials during proton beam transport can significantly alter the target heating profiles.

Chapter 1

Introduction

This chapter discusses the motivations for continued research into intense proton beams. High Energy Density Science (HEDS) and Inertial Confinement Fusion (ICF) are suitable applications of proton beams, as both areas require efficient energy delivery and deposition. A brief introduction to each topic and discussion about the strengths that proton beams can bring to them will be given in the following subchapters.

1.1 Ion Beams and High Energy Density Science

High energy density science (HEDS) is an active and rapidly growing field with its potential for various applications and scientific discoveries. A broad range of research topics, including understanding of astrophysical observation, material science, nuclear physics, and fusion energy science, are deeply related to the field of high energy density. As one can infer from its name, HEDS resides in physical environments where the energy density is high, exceeding $10^{11} J/m^3$, which corresponds to pressure above 1 Mbar. With this pressure condition, a solid density material becomes an ionized medium called dense plasma that is colder than traditional plasma (ionized gas), while low-density matter becomes a high temperature state. For example, air in the order of atmospheric density has a temperature of 10 keV ($\sim 10^8 K$) at 1 Mbar [1]. In order to explore the physical phenomena of HEDS, tools producing high energy density conditions are necessary. With the

advances in technology, the laser has been extensively applied to create high energy density conditions. Energetic lasers, such as National Ignition Facility (NIF, > Megajoule) and Omega Laser Facility (>40 kJ), can deliver high energy to a small volume (< cubic mm) resulting in pressure greater than 1 Mbar. Along with lasers, the pulsed power device, Z-machine, producing high energy x-rays (> MJ) and particle accelerators that send numerous relativistic particles have also contributed exploration of experimental studies for HEDS.

Herein, we will focus on ion beams in HEDS. Ion beams are closely related to HEDS as they are advantageous for the creation and diagnosing of the condition of high energy density. A unique characteristic of ions is their energy deposition, whereby the rate of energy deposition is highest at the end of their stopping range, contrary to other sources, such as electron and laser. For energy deposition in a medium, problems caused by injected electron beams and lasers are, respectively, high divergence and the laser's wavelength limiting the heating to only the surface of a target. However, ions provide relatively deep penetration depth and volumetric heating profiles. These properties are advantageous for the creation of high energy density conditions, particularly the warm dense matter (WDM) state. The WDM is a partially or fully ionized state with temperature conditions from 1 to 100 eV and a density of 0.1-10x solid that exists in the middle of states, being neither plasma nor solid. Due to its properties that overlie the boundaries of plasma physics and condensed matter, there are many questions regarding physical phenomenon, and thus, WDM has been a subject of great interest. The laser-driven proton beams are widely used in experiments for WDM studies, due to the capability that these beams can be intense enough to heat a target up to 10s of eV. In the experiments, various materials, such as carbon, aluminum, and graphite, were isochorically heated by proton beam for fundamental studies, including measurement of equation of state and electron-ion energy relaxation. [2] [3] [4]

Isochoric heating, provided by an intense proton beam, is beneficial not only for WDM studies but also proton fast ignition concept of inertial confinement fusion. As a possible application, ICF is the longtime goal remaining in the field of HEDS. In the following subchapter, we will begin with the review of ICF to discuss

how proton beams play a crucial role in ICF through the fast ignition concept.

1.2 Inertial Fusion Energy

Nuclear fusion has been of great interest since the early 1900s with a rich scientific history, including Arthur Eddington's suggestion that the fusion of hydrogen into helium is the energy source of the sun. Nuclear fusion is the process by which light nuclei fuse together to become a heavier one with the mass change resulting in energy release via mass-energy equivalence of Einstein's famous formula. The difficulty of this fusion reaction comes from the Coulomb repulsion force between charged nuclei, but if a system (plasma) is sufficiently hot, energetic nuclei can overcome the Coulomb barrier and collide. The most efficient fusion reaction in terms of reactivity per given energy is the deuterium-tritium (DT) reaction described as

$$ {}^{2}_{1}\mathrm{D} + {}^{3}_{1}\mathrm{T} \rightarrow {}^{4}_{2}\mathrm{He}\,(3.5\,\mathrm{MeV}) + \mathrm{n}\,(14.1\,\mathrm{MeV}) \qquad (1.1) $$

This is because the DT case has a high fusion cross section which leads to high reaction rate. As shown in Fig.1.1, the DT reaction shows the largest cross section over other processes for kinetic energy up to about 200 keV.

To achieve fusion ignition (enough a fusion reaction to generate energy greater than energy loss), this DT fuel heated to high temperature (above keV) needs to be confined for sufficient time. As a way of confining the fuel, Magnetic Confinement Fusion (MCF) uses the magnetic field to confine DT plasma in a toroidal reactor of a 10 m scale. Another technical approach of confining the fuel for fusion is Inertial Confinement Fusion (ICF), which is what we will focus on here.

Contrary to MCF of large scale, ICF uses a compressed DT capsule (diameter of compressed DT plasma is only $\sim 100\ \mu m$) as fuel for the fusion reactions. DT fuel as a gas is contained in a spherical shell of DT ice on the inner surface and CH or Si-doped material on the outer surface. In the ICF process, this outer surface (ablator layer) is blown out by an intense radiation driver, giving an inward pressure due to momentum conservation, and resulting in implosion and fuel

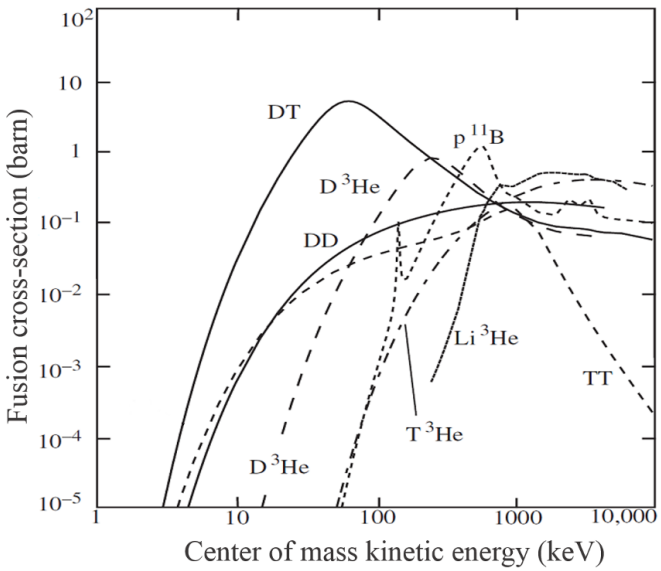

Figure 1.1: Fusion cross sections as functions of center-of-mass energy for various reactions of fusion energy. The curve labeled as DT has the highest cross section.(extracted from [5])

compression. The implosion process is maintained by the inertia of the fuel, but this compressed fusing fuel disassembles by its internal high pressure.

There are two schemes to irradiate the ablator layer of the fuel capsule, direct drive and indirect drive. A direct drive uses laser beams to directly irradiate the ablator layer of the capsule, whereas, in an indirect drive, soft x-rays produced by laser interactions in a hohlraum are used to irradiate the ablator. A hohlraum is typically a cylindrical shape with laser entrance holes, and is made of high-Z materials (typically Au). When the interior walls of a hohlraum are heated by intense lasers, they emit Planckian thermal radiation, which drives implosion of the fuel capsule. Since an indirect drive has an extra process to irradiate the capsule, only $\sim 15\%$ of the laser energy is coupled to the ablation layer of the capsule. This coupling is lower than in the case of a direct drive ($\sim 50\%$). However, x-rays in an indirect drive scheme uniformly irradiate the fuel capsule and this uniformity is a crucial condition for ICF and an ideal implosion.

For the implosion, meeting the requirement for the entire fuel to ignite at once would be inefficient, bringing a relatively low energy gain because the high

driving energy for compression is required until all the fuel becomes hot enough to ignite. However, if a small portion of the fuel is heated for ignition and the alpha particles, as fusion products, heat the rest of fuel, relaxed driving energy will lead high energy gain.

The conventional ignition method with this implosion approach is central hot spot (CHS) ignition, which is the approach undertaken at the NIF. During the compression, DT gas experiences volumetric compression to a greater extent than the DT ice, and a series of shocks launched by the driver converge at the center. Through heating of this adiabatic process and the shocks, a central hot spot with an ignition temperature $kT \sim 5keV$ is formed, and surrounded by relatively cold and high density ($\sim 1000g/cm^3$) solid DT ice. Here, the areal density ρr of the hot spot is $\sim$0.3 g/cm^2, which is approximately the range of the alpha particle. Thus, alpha particles produced from the hot spot can be reabsorbed, resulting in thermonuclear burn wave into the surrounding cold fuel [6].

In the process of an ICF implosion, Rayleigh-Taylor (RT) instability [7] is inevitably excited, since the ablator (low-density plasma) pushes higher density fuel layer. This instability can cause the mixing of ablator and DT fuel, which drops hot spot temperature and fusion yield, and thus, the RT instability has been known as a major issue for ICF implosion. Through reducing the instability with the high-foot driver scheme at the NIF, a high yield [8] and fuel gain above unity in ICF was reported in [9].

The high-foot laser pulse has a higher first peak and shorter pulse duration compared to low-foot pulse, as shown in Fig.1.2. This driver pulse shape is designed for relatively high radiation temperature of the hohlraum, which drives faster ablation velocity and stronger first shock to enhance the adiabat of the implosion. The benefit of implosion with these conditions is reducing the growth rate of RT instability between the ablation front and the DT-fuel, resulting in higher yield implosion. A comparison of DT neutron yield between two pulse schemes is shown in Fig.1.2, where a higher contribution of α particle to total yield is seen (above 1.5 $\times$ in the plot). Further studies regarding the high-foot scheme [9] [10] have reported that self-heating yield is close to compression yield for ICF implo-

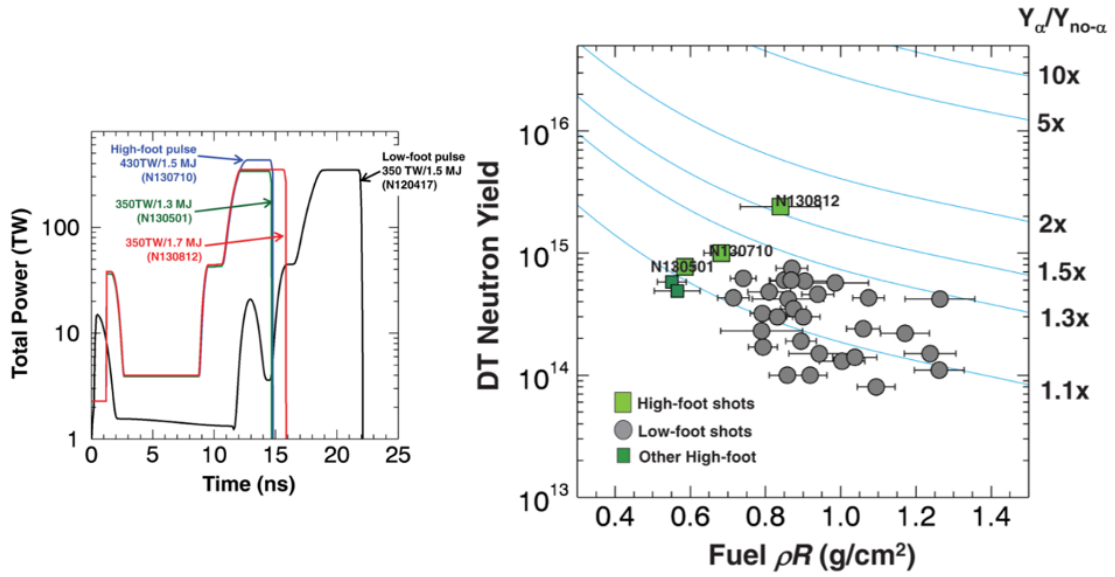

Figure 1.2: Comparison of laser powers in time of low-foot pulse and high-foot pulse shape (left) DT neutron yield as a function of fuel areal density for both pulse shapes (right). Contours shown as the blue curves indicate α-heating multiplication (taken from [8]).

sions. However, for this scheme, there is a trade-off between the benefit of stability and relatively less fuel compression [11]. Additionally, output fusion energy from this approach is still far below ($\sim$ two orders of magnitude) the input drive energy (laser energy $> 1MJ$), so significant improvement is required for successful applications of fusion energy. In order to increase the energy efficiency of fusion reaction (high yield with low driver energy), alternative approach such as fast ignition and shock ignition have been studied. In the following subchapter, we will review the fast ignition (FI) concept with a focus on FI using ion beams.

1.2.1 Fast Ignition with ion beams

The Fast Ignition (FI) scheme differs from CHS through decoupling of DT fuel compression and ignition triggering. These separated processes aim for increased overall efficiency by relaxing the fuel compression requirement compared to CHS, but applying an external energy source to more directly raise the temperature in a fast ignition hot spot. Fig.1.3 shows a comparison of CHS and FI schemes

in terms of the DT fuel density and temperature in the fuel spatial profile. In the CHS scheme, a hot spot of low density is surrounded by cold high density plasma, while the FI scheme has a uniform density for both hot spot and compressed fuel (isochoric ignition). Compared to CHS, the FI (isochoric) scheme compresses more fuel mass to a lower peak density (300 g/cm^3), and, by reducing the compression requirement, a reduced driver energy can be used. More mass to burn with relaxed driver energy results in high yield and gain. Additionally, this low required compression in FI is beneficial for a reduction in the growth of Rayleigh-Taylor instability. To create an ignition hot spot under Fast Ignition conditions (ρr ~0.5 g/cm^2 and T_{hot} ~12 keV), a high amount of energy must be delivered through the external source (laser or particle beams). The parametric 2D simulation study with an assumption of a cylindrical beam model [12] shows that the external source should have energy ~20 kJ with size $radius < 20\mu m$ for triggering ignition. The source pulse duration needs to be shorter than the confinement time (~ 20 ps) for a fuel density of 300 g/cm^3. [6]

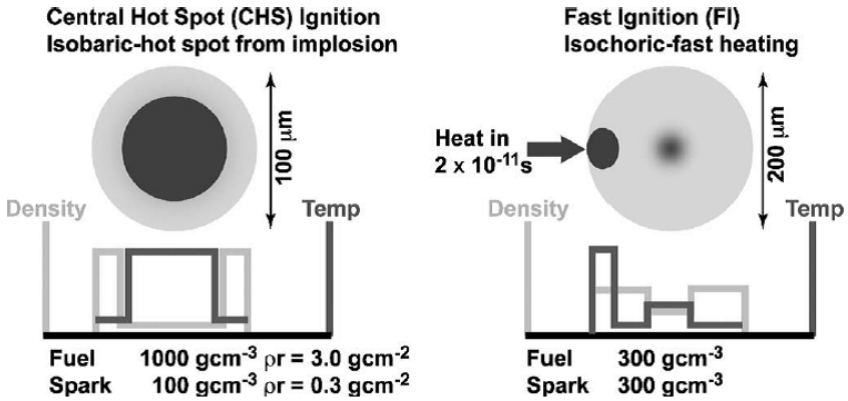

Figure 1.3: The density and temperature profiles of compressed DT fuel in ICF ignition with CHS and FI schemes. (from [6])

With the advantages of FI mentioned above, extensive studies have been conducted for FI, including various possible external sources such as laser [13], electron beams [14], and ion beams. Inevitable complications of laser penetration into dense plasma and electron beam spread are issues that have arisen, respectively, for laser and electron beam cases, whereas the ion FI scheme can be advantageous

due to its energy delivery where the ion beams propagate with relatively small spread. Moreover, localized beam energy deposition (Bragg peak like) characteristics of ion beams are promising for the FI scheme. Figure 1.4(left) illustrates the proton FI concept, where a proton beam is generated at the rear surface of a target by strong electric field formed with laser-accelerated electrons, called target normal sheath acceleration (TNSA). We will review the TNSA mechanism in the next chapter.

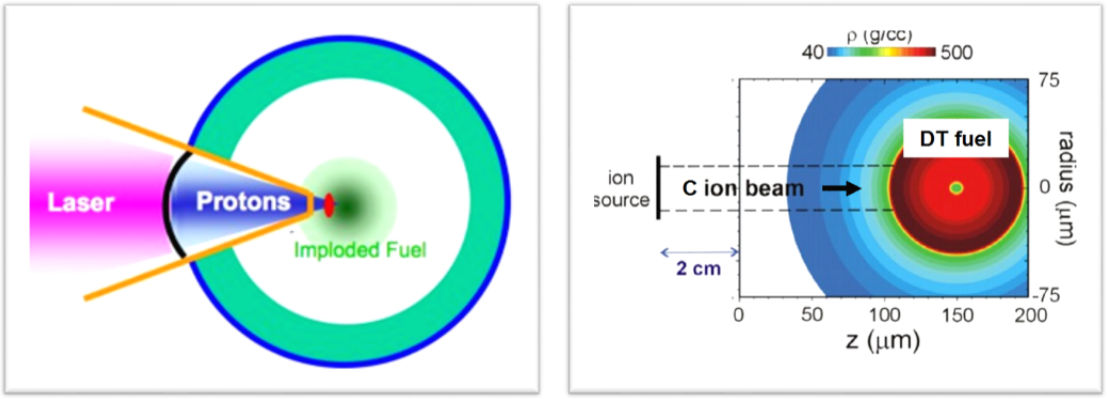

Figure 1.4: Illustration of envisioned ion FI scheme. (left) Proton FI concept with cone-guided structure. (right) Carbon beam FI concept shown with fuel density map. Images from [15] [16]

In order to increase the efficiency of the power density (proton to fuel), the majority of focused proton beam needs to reach into the compressed fuel. To fulfill this requirement, the cone-guided design shown in the illustration is required. As the Au cone in the shell allows the space between the proton source and the DT fuel, proton beam flying a relatively short distance can arrive at dense fuel, avoiding beam divergence or complex transport in the fuel. Also, proton beam focusing by a curved target with TNSA mechanisms can be applied as the curved target is placed near the fuel under the protection of the cone structure.

The main parameters for proton FI were reported by Atzeni [17], based on analysis of 2-D numerical simulations. Since deposited proton energy in the fuel depends on the proton stopping power, the slowing down of protons with different initial energies were analyzed as a function of plasma temperature. As shown in Fig.1.5 (a), proton ranges in the fuel showing constant values at low

temperatures rise with an increase in plasma temperature as proton stopping power decreases. With this energy dependent proton range, a proton beam of broad energy distribution, generated by the TNSA mechanism, can deposit its energy within a narrow region of DT fuel (i.e. the faster protons preheat the fuel, the slower protons experiencing reduced stopping that can reach a similar distance where the faster ones stop). Taking into account the variant proton range, the required proton beam energy for ignition of compressed DT fuel of $400 g/cm^3$ was analyzed from 2D simulations. Required beam energy versus beam temperature (average of energy distribution) is shown in Fig.1.5(b). Herein, d is the distance from the beam source to the compressed fuel. Since the proton beam has an exponential energy distribution, the beam spreads out (velocity dispersion) during its transit. Thus, shorter distance, d, enables the proton beam to be less dispersed resulting in the reduction of the required beam energy. The minimum required energy ~16 kJ for $d = 1mm$ is much lower than the energy ~40 kJ of the long distance case ($d = 4mm$). Considering energy-conversion efficiency from laser to proton beam (10%), a laser having 160 kJ energy is needed for proton-FI.

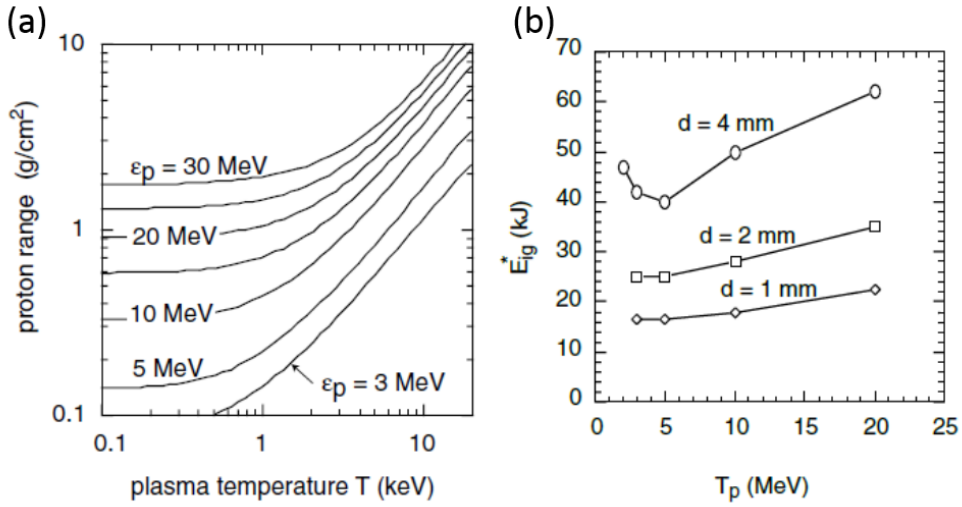

Figure 1.5: Proton range with various initial proton energy in DT fuel having density of 400 g/cm^3 as a function of DT temperature (a). Minimum beam total energy for fast ignition versus proton average energy of exponential energy spectrum with different distances from the beam source to the DT fuel (b). (from [17])

Along with proton beams, alternative ion species that are heavier than proton have also become candidates for FI with advances in heavier ion acceleration. Recent studies have shown the possibility of ion acceleration to high energies with a narrow energy spectrum (quasi-monoenergetic) using laser interaction with a thin foil, known as radiation pressure acceleration (RPA) [18] or the break-out afterburner (BOA) mechanism [19]. Applying one of these ion acceleration methods, a FI scheme with carbon ions can be envisioned as illustrated in Fig 1.4(right). Contrary to the proton FI case, a carbon beam source may be located far away from the fuel without a cone-guided structure since the required beam energy spectrum for carbon-FI is different from the proton-FI case. For ions heavier than protons, the effect of increasing stopping range with plasma temperature is weaker than the proton case. Therefore, the ion beam with a narrow energy spectrum (monoenergetic) would be suitable for local energy deposition for ion-FI. Since ions need to propagate sufficiently long distance into the compressed fuel, a high kinetic energy for carbon ($>$ 200 MeV) is also required [20].

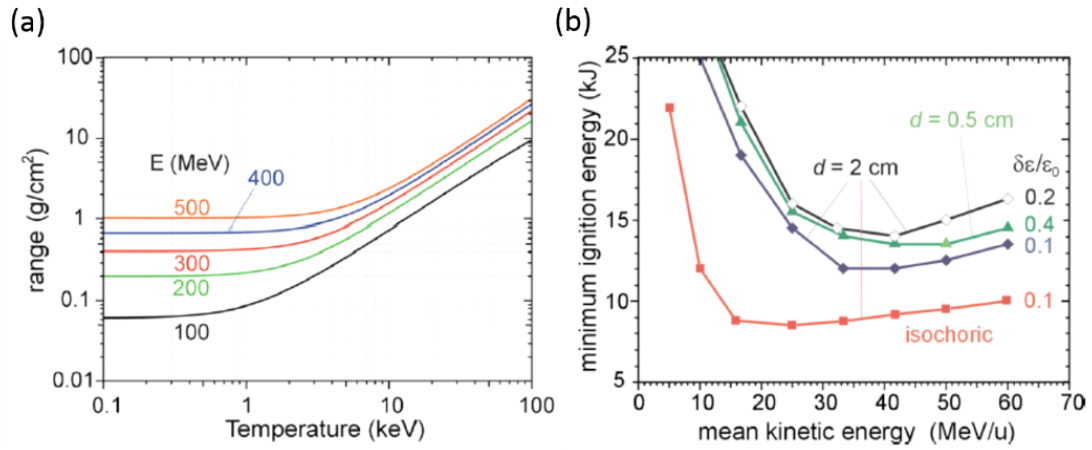

Figure 1.6: Range of carbon ion with various carbon kinetic energy in DT fuel of density 400 g/cm^3 as a function of DT temperature (a). Minimum beam energy for FI ignition versus carbon kinetic energy with different energy spreads $\delta\varepsilon/\varepsilon_0$ (b). [16]

With monoenergetic carbon ions, required beam energy for FI was reported by Honrubia [16]. As shown in Fig.1.6 (a), the trend of varying carbon range with DT plasma temperature is similar to the one for proton (Fig.1.5(a)), but

a much higher kinetic energy is required for carbon ions to propagate deep into the compressed fuel. For the monoenergetic carbon case, the minimum required ignition energy is relatively insensitive to the distance d from the beam source to the compressed fuel, as shown in Fig.1.6 (b). Instead, energy spread $\delta\varepsilon/\varepsilon_0$ has been found to be important for affecting the minimum ignition energy and low energy spread ($\delta\varepsilon/\varepsilon_0$=0.1) brings a low minimum required ignition energy. Additionally, the super-Gaussian density distribution of DT fuels can lower the ignition energy, as shown with label isochoric in the plot. However, the assumption for these estimations is that the energy conversion efficiency from laser to carbon ion is 10%. This conversion efficiency is challenging to achieve, but needs to be demonstrated experimentally for the application of ion-FI.

As can be seen from this discussion, an accurate understanding of intense ion beam transport and energy deposition in warm and hot plasmas will be critical for achieving ion-FI.

1.3 Outline of the Dissertation

Chapter 2 provides the theoretical description of laser-matter interaction that begins from single electron motion in a laser to fast electron acceleration with a high-intensity laser. Mechanisms of ion acceleration, depending on laser parameters, are discussed. For an understanding of ion beam transport, theories of ion stopping power in different conditions of matter are presented.

Chapter 3 begins with an overview of the particle-in-cell simulation technique and describes the algorithms in the LSP code which is used for the computational study of proton beam transport and modelling of experimental results in this thesis. Details of code implementation for proton stopping power calculation in LSP are discussed, as well as a presentation of various stopping power calculations of protons within different conditions of proton and matter. Also, the simulation of ion acceleration using the LSP code is presented.

Chapter 4 gives two experimental results regarding proton beam generation. The first set of results shows a proton beam focusing effect with structures

attached to the main target of proton generation, where electric fields driven by hot electrons positioned on the structure enable the beam focusing. Simulation modeling giving further understanding of the experimental data is presented, followed by experimental results showing different emissions of Cu K_α depending on beam focusing. The second set of experimental results show the dependence of conversion efficiency from laser to proton on target geometry, in which an isolated target results in a higher number of protons, raising the conversion efficiency.

Chapter 5 presents computational studies of proton beam transport and stopping in solid density matter. Firstly, the dynamics of stopping for a proton beam is dependent on beam conditions and the target materials presented. Then, charge and current neutralization of the proton beam during its transport are discussed. Associated with the return current, beam collective effects become crucial in terms of generation of magnetic field and beam focusing. An analytical model and simulation results describe these beam collective effects, including the influence of beam kinetic energy and target temperature. Lastly, target heating mechanisms are discussed.

Chapter 6 gives the details of the experimental results conducted on the Trident short pulse laser. Measuring the size and the intensity of proton heating on different target materials provides material effects that act on proton beam transport. The experimental data show material dependent XUV emission (wider and brighter emission with low Z material). LSP simulations provide explanation that varying proton stopping power with a thermodynamic state change in the heating profiles of targets.

Chapter 7 summarizes the experimental and simulation results and concludes the findings of this work. Topics that warrant additional future research for possible ion beam applications are also discussed.

1.4 Role of the Author

For the computational study of ion beam transport and stopping, the author implemented a new stopping calculation module covering WDM state in hybrid

PIC code LSP, where the local stopping power of protons in solid density matter was updated based on the matter thermodynamic state, as presented in Chapter 3. With this capability, the author performed the self-consistent simulation of proton beam transport in matter to investigate beam dynamics depending on varying stopping power, collective effects, and energy deposition of the beam to the matter. Code development, benchmarking, and numerous test cases were carried out by the author. Additionally, simulation results were analyzed and compared with analytical models, as discussed in Chapter 5.

In experiments conducted on the T-cubed laser at the University of Michigan and Trident laser at Los Alamos National Laboratory, shown in Chapter 4 and 6, the author was involved in setting up targets and diagnostics, as well as analyzing the data obtained from the experiments.

To further understand the results from the Trident experiment and Omega experiment, presented in Chapter 4, the author ran simulations to model the experiment and provided the explanation of the beam transport properties of different materials and field effects of assembled targets on intense proton beams.

Chapter 2

Theoretical Background

2.1 Physics of relativistic laser matter interaction

2.1.1 Electron Motion in Laser Fields

When a laser, electromagnetic wave, interacts with the plasma, electrons in plasma primarily feel oscillating electric field, $\mathbf{E} = E_0 cos\omega t$. Electron motion in the field can be described as $m_e d\mathbf{v}/dt \approx e\mathbf{E}$, where m_e and e are the electron mass and charge, respectively. Integral of this momentum equation over time gives this oscillation velocity of the electron known as quiver velocity [21], $v_{osc} = eE_0/m_e\omega$, where ω is the frequency of laser field. The ratio of quiver velocity to speed of light is used as a scaling parameter known as the normalized vector potential

$$a_0 = \frac{v_{osc}}{c} = \frac{eE_0}{m_e c\omega} \tag{2.1}$$

The normalized vector potential higher than or equal to unity, $a_0 \geq 1$, indicates laser field is relativistic where quiver momentum exceeds $m_0 c$. Solving for the E_0 such that $v \sim c$ and laser intensity, $< S >= E_0^2/2\mu_0 c = \epsilon_0 c E_0^2/2$, a practical estimation of relativistic regime can be defined as

$$a_0 = \sqrt{\frac{I_L \lambda_L^2}{1.37 \times 10^{18}}} \tag{2.2}$$

Where I_L and λ_L are the laser intensity in units of Wcm^{-2} and wavelength of laser in μm. Therefore the injected laser with an intensity of $\sim 10^{18} Wcm^{-2}$ and $1\mu m$ wavelength drive electrons relativistic motion. When relativistic, electron motion can be described with Lorentz force

$$\frac{d\mathbf{p}}{dt} = q[\mathbf{E} + \mathbf{v} \times \mathbf{B}] \tag{2.3}$$

where $\mathbf{P}$ is $\gamma m_e \mathbf{v}$ and the relativistic factor γ is described as $\gamma = \sqrt{1 + a_0^2}$. As $\mathbf{v}$ is close to c, $\mathbf{v} \times \mathbf{B}$ becomes important while it is ignored for non-relativistic case.

Oscillating electron motion by ideal EM wave is varied in intense short pulse laser which has a strong radial gradient of intensity over a few wavelengths. In this condition, electrons drift over long timescales, and the force causing this drift is called the ponderomotive force. The ponderomotive force pushes electrons near the center of a laser field (high laser intensity) toward the weak field area (low intensity). Considering the non-relativistic case, this force can be found from single electron motion oscillating under the electric field, $\mathbf{E} = E_0 cos\phi = E_0 cos(kz - \omega t)$. Then the equation of motion, Lorentz equation, can be described as

$$\frac{\partial v_x}{\partial t} = -\frac{e}{m}\mathbf{E} = -\frac{e}{m}E_0(x)cos\phi \tag{2.4}$$

by the truncated Taylor expansion of the electric field, $\mathbf{E} \simeq E_0(x)cos\phi + x\frac{\partial E_0(x)}{\partial x}cos\phi$, with the assumption that spatial variation of laser field is relatively smaller than the spatial variation of oscillation. By integrating this equation 2.4, the velocity and position of a single electron are given as

$$v_x = -\frac{eE_0(x)}{m\omega}sin\phi \tag{2.5}$$

$$x = \frac{eE_o(x)}{m\omega^2}cos\phi \tag{2.6}$$

Substituting the equation 2.6 into the second order terms of equation 2.4 gives

$$\frac{\partial v_x}{\partial t} = -\frac{e^2 E_0(x)}{m^2\omega^2}cos\phi\frac{\partial E_0(x)}{\partial x}cos\phi = \frac{-e^2}{m^2\omega^2}\frac{\partial^2 E_0(x)}{2\partial x^2}cos^2\phi \tag{2.7}$$

Taking the cycle-average of this equation gives the ponderomotive force of the electron as [21]

$$f_p \equiv \left\langle m\frac{\partial v_x}{\partial t}\right\rangle = -\frac{e^2}{4m\omega^2}\nabla E_0^2 \tag{2.8}$$

As shown in the equation, the force is proportional to the gradient of the electric field (laser inensity) indicating that an electron near the peak of electric field (usually center of laser beam) will drift away toward low field area. Also, the force depends on the particle's mass but not on the charge polarity meaning that heavier ions require much stronger laser intensity to be moved.

2.1.2 Propagation of a Laser in Plasma

For the situations considered in this thesis, injected laser light propagates into plasmas. Even for the solid target, a laser passing through a plasma is inevitable due to the pre-formed plasma near solid density. Since the propagation of a laser in plasma is of widespread importance in plasma science, we will now discuss how a plasma modifies the propagation of the laser. We begin with describing the plasma electron fluid responding to the high frequency field $\mathbf{E} = E_0 exp(ikx - i\omega t)$,

$$m_e \frac{\partial \mathbf{v_e}}{\partial t} = -e\mathbf{E} \tag{2.9}$$

where $m_e, v_e$and e are respectively electron mass, electron velocity and charge. Since the current density is $\mathbf{J} = -n_e e v_e$, integral of equation 2.9 gives the electron current density

$$\mathbf{J} = \frac{ie^2 n_e \mathbf{E}}{\omega m_e} = \frac{i\omega_p^2}{4\pi\omega}\mathbf{E} = \sigma\mathbf{E} \tag{2.10}$$

where ω_p is the plasma frequency and the conductivity of the plasma σ is $i\omega_p^2/4\pi\omega$. Substituting this σ into Ampere's law and using the Fourier transform give

$$\nabla \times \mathbf{B} = -\frac{i\omega}{c}\epsilon\mathbf{E} \tag{2.11}$$

$$\epsilon = 1 - \frac{\omega_p^2}{\omega^2} \tag{2.12}$$

Using a vector identity $\nabla \times (\nabla \times B) = \nabla(\nabla \cdot B) - \nabla^2 B$, the curl of this equation turns out

$$\nabla^2\mathbf{B} + \frac{\omega^2}{c^2}\epsilon\mathbf{B} = 0 \tag{2.13}$$

Since $\nabla = ik$, the final dispersion relation for laser (electromagnetic wave) in plasma becomes

$$\omega^2 = \omega_p^2 + k^2c^2 \tag{2.14}$$

Comparing to the vacuum relation, $\omega^2 = k^2c^2$, it can be found that plasma oscillation term ω_p^2 is added. The dispersion relation 2.14 includes cutoff phenomenon which is that k^2 becomes zero with a certain density (or frequency ω_p^2) indicating that the light can not propagate in the plasma. This plasma density is called critical density and can be found from the condition of $\omega^2 = \omega_p^2 = \frac{n_c 4\pi e^2}{m_e}$.

$$n_{cr} = \frac{m_e \omega^2}{4\pi e^2} \tag{2.15}$$

Practically, this equation can be written as [22]

$$n_{cr} = \frac{1.1 \times 10^{21}}{\lambda_L^2} (cm^{-3}) \tag{2.16}$$

When a laser is incident on the critical density from a less dense side, it reflects but the evanescent wave can propagate a short distance, called the skin depth, into the target. This is because the wave has a spatial dependence $exp(ikx)$, it is exponentially attenuated if k is imaginary.

$$e^{ikx} = e^{-|k|x} = e^{-x/\delta} \tag{2.17}$$

The skin depth δ is

$$\delta = |k|^{-1} = \frac{c}{(\omega_p^2 - \omega^2)^{1/2}} \tag{2.18}$$

2.1.3 Laser Absorption and Hot Electron Generation

The laser absorption and the hot electron generation have been extensively studied and they are still interesting topic because the understanding of energy transfer from the laser to electrons and hot electron characters are crucial for many applications such as laser heating, ion beam generation and inertial confinement fusion with concepts of the shock ignition and fast ignition.

We will begin with the collisional absorption. As the laser is incident on plasmas, electrons in plasmas oscillate via a high frequency field $E(x)exp(-i\omega t)$ of the laser. These electrons transfer laser energy to the plasma by collisions with stationary ions, and the laser absorption through this process is the collisional absorption which is also known as inverse bremsstrahlung absorption. Closely

following [22], this condition can be described with motion equation

$$m\frac{\partial \mathbf{v_e}}{\partial t} = -e\mathbf{E} - m\nu_{ei}\mathbf{u_e} \tag{2.19}$$

where ν_{ei} is electro-ion collision frequency. This equation is arranged as

$$\mathbf{v_e} = \frac{-ie\mathbf{E}}{m(\omega + i\nu_{ei})} \tag{2.20}$$

Substituting this electron velocity to the plasma current density, $\mathbf{J} = -n_e e\mathbf{u_e}$ gives the plasma conductivity σ from $\mathbf{J} = \sigma\mathbf{E}$

$$\sigma = \frac{i\omega_p^2}{4\pi(\omega + i\nu_{ei})} \tag{2.21}$$

From Ampere's law, the plasma dielectric function can be derived

$$\nabla \times \mathbf{B} = \frac{4\pi}{c}\sigma\mathbf{E} - \frac{i\omega}{c}\mathbf{E} = -\frac{i\omega}{c}\epsilon\mathbf{E} \tag{2.22}$$

$$\epsilon = 1 - \frac{\omega_p^2}{\omega(\omega + i\nu_{ei})} \tag{2.23}$$

Taking the curl of Faraday's law and equation 2.22 gives the wave dispersion relation

$$\nabla \times (\nabla \times \mathbf{E}) = \frac{i\omega}{c}\nabla \times \mathbf{B} = \frac{\omega^2}{c^2}\epsilon\mathbf{E} \tag{2.24}$$

$$k^2c^2 = \omega^2\epsilon \tag{2.25}$$

k is from $E(x) \sim exp(ikx)$. Substituting the dielectric function into the above equation, the final dispersion relation turns out

$$\omega^2 = k^2c^2 + \omega_p^2\left(1 - \frac{i\nu_{ei}}{\omega}\right) \tag{2.26}$$

From the expression of $\omega = \omega_r - i\nu/2$ and the equation 2.26, the energy damping rate, ν is given as

$$\nu = \frac{\omega_p^2}{\omega_r^2}\nu_{ei} \tag{2.27}$$

Here, electron-ion collision frequency in plasmas can be written using a impact parameter, b, as $\nu_{ei} \simeq n_i\pi b^2 v_{th}$. b is arranged from the energy conservation,

$$\frac{Ze^2}{b} \simeq \frac{m_e v_{th}^2}{2},\ b \simeq \frac{2Ze^2}{m_e v_{th}^2} \tag{2.28}$$

Plugging in the b into ν_{ei} with an assumption of quasi-neutral condition ($Zn_i = n_e$) gives

$$\nu_{ei} \propto \frac{n_e Z}{T_e^{3/2}} \tag{2.29}$$

This gives an indication that high Z material has more collisions and thus laser can be damped easily.

When a laser is incident obliquely in inhomogeneous plasma, there is an absorption called resonance absorption. If laser incidence angle θ is between the laser vector k and the direction of plasma density gradient z, the laser reflects where $\omega_p = \omega cos\theta$. Since the dielectric function of plasma is $\epsilon = 1 - \omega_p^2/\omega^2$ as seen in the equation 2.12, reflection happens when $\epsilon(z) = sin^2\theta$. However, if the electric field vector of the laser lies in the plane of incidence (P-polarized), this electric field can tunnel into the critical density and electrons are oscillated by the electric field along the density gradient at near the critical density. This electric field $\mathbf{E_d}$ oscillating electrons and the absorbed energy flux I_{abs} are given as [22]

$$\mathbf{E_d} = \frac{\mathbf{E_{FS}}}{\sqrt{2\pi\omega L/c}}\phi(\tau) \tag{2.30}$$

$$I_{abs} \simeq \frac{\omega L \mathbf{E_d}^2}{8} \tag{2.31}$$

Here, $\mathbf{E_{FS}}$ is electric field value of the light in vacuum and L is the density scale length. The field $\mathbf{E_d}$ decreases when the $\tau = (\omega L/c)^{1/3}$ goes to 0 as $\phi(\tau) \simeq 2.3\tau exp(-2\tau^3/3)$. This indicates that the driver field is dependent on the light angle. The oscillation of the electrons causes charge density fluctuation and this fluctuation frequency is equal to the electron plasma frequency at the critical region. Thus, the fluctuation can be enhanced resonantly and this fluctuation drives the electrostatic field (electron plasma wave) into the plasma. Eventually this wave is damped by collisions or Landau damping. Comparing to the collisional absorption, resonance absorption is dominant absroption mechanism for high laser intensities because high intensity laser heats a plasma to become the collisionless plasma state ($\nu_{ei} \propto T_e^{-3/2}$). Typically, this resonance absorption is the main absorption mechanism for laser density over $10^{15} W/cm^2$ but not in the case of relativistic intensity ($> 10^{18} W/cm^2$). It needs to be noted that even for the extremely high laser intensity, there is generally some pre-plasma on front surface

of a target, the resonant absorption plays an important role to the laser energy deposition. It has been found that the distribution of electrons in this process becomes a roughly high energy tail of Maxwellian, superimposed on the background temperature. The temperature of these hot electrons is scaled as [23]

$$T_{hot} \approx 10[T_{keV} I_{15} \lambda_L^2]^{1/3} keV, \tag{2.32}$$

where T_{keV} and I_{15} are the background electron temperature and the laser intensity in units of $10^{15} W/cm^2$, respectively.

The laser absorption mechanisms show different aspects for the sharp electron density gradient on the front of a target which is possible with a high-contrast intense laser light. The absorption of intense laser is mostly collisionless process such as Vacuum heating (Brunel heating) [24] and $\mathbf{J} \times \mathbf{B}$ heating [25]. Both absorption mechanisms have a similarity with the resonance absorption as the electric field of laser affect electrons motion but now, density gradient scale length is smaller than the laser wavelength not giving an enough space that allows resonance absorption. By electric fields, electrons are pushed and pulled at near the interface between vacuum and target front surface forming a sheath field. In the Brunel mechanism, electrons are accelerated normal to the interface by the laser electric field or the sheath field but for the $\mathbf{J} \times \mathbf{B}$ heating case, the direction of electron acceleration is identical to the laser propagation direction. This is because the ponderomotive force is the main source of the acceleration of electrons where as we reviewed before, electrons oscillate at twice the laser frequency and are accelerated with the direction of the laser axis. With an increase in the laser intensity and relativistic electrons, this $\mathbf{J} \times \mathbf{B}$ heating becomes crucial mechanism and the effects from the electric field direction (p-polarization and s-polarization) is reduced. Since the ponderomotive force drives electron acceleration, we can use the ponderomotive potential $U_p = mc^2(\gamma - 1)$ to characterize accelerated electrons (hot electron generation). From the relativistic ponderomotive potential given as

$$U_p = mc^2 \left(\sqrt{1 + \frac{I_L \lambda_L^2}{1.37 \times 10^{18}}} - 1 \right) \tag{2.33}$$

the effective temperature of the hot electrons are derived as [26]

$$T_{hot} \approx 0.511MeV\left(\sqrt{1+\frac{I_L\lambda_L^2}{1.37\times10^{18}}}-1\right) \tag{2.34}$$

Following this equation, for instance, a laser having a intensity of $4\times10^{18}W/cm^2$ with $1\mu m$ wavelength produce electrons with $T_{ehot} \approx 0.5MeV$. The hot electron temperature was empirically demonstrated by Beg et al. [27] for laser intensities up to $10^{19}W/cm^2$. Hot electron temperature is scaled as

$$T_{hot} \approx 100keV(I_L\lambda_L^2/10^{17})^{1/3} \tag{2.35}$$

2.2 Theory of Ion Acceleration

2.2.1 Target Normal Sheath Acceleration (TNSA)

Ion beam generation via target normal sheath acceleration (TNSA) mechanism has been demonstrated through extensive studies experimentally [28] [29] as well as numerical analysis [30] [31]. When a laser pulse irradiates a target, which can be solid or liquid, hot electrons travel through the target with a broad emittance angle. Some hot electrons escape from the target but many of electrons form an electron cloud at the rear surface of the target due to a coulomb potential. These hot electrons relax to a Boltzmann equilibrium, $N_e \sim exp(-e\Phi/kT_{hot})$ where hot electrons spread over a sharp ion density profile. By the charge separation at this region, a strong electric sheath is built up with a scale length of Debye length of the hot electrons [32].

$$E_{sheath} \approx \frac{k_BT_{ehot}}{el}\left(\frac{MV}{\mu m}\right) \tag{2.36}$$

$$l \sim \lambda_D = \sqrt{\frac{kT_{ehot}}{4\pi n_{ehot}e^2}} \tag{2.37}$$

This electric field, generally above TV/m, is strong enough to ionize atoms at the rear surface of the target where a contaminant layer (hydrocarbon), naturally formed or pump-oil vapor, generally locates at this region. Protons in this layer,

having the highest charge-to-mass ratio, are accelerated normal to the target surface. These protons propagate in vacuum with electrons forming a quasi-neutral plasma. At the edge of expanding plasma, the hot electron Debye length is greater than the ion scale length where a charge sheet is retained providing further energy transfer from electron to ions. This process of proton acceleration is drawn in Fig.2.1.

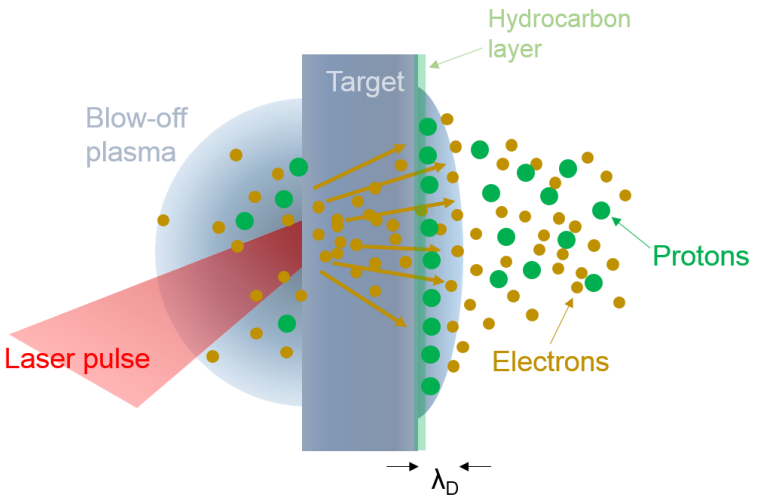

Figure 2.1: Cartoon showing TNSA mechanism. Hot electrons driven by a laser pulse travel through the target setting up a sheath field with a Debye length on the back surface. Protons in the hydrocarbon layer are ionized by the electric sheath field and accelerated normal to the target surface.

For the analytical estimate of TNSA mechanism, 1D plasma expansion model can be employed [33] [30]. We will discuss 1D models beginning with reviewing the self-similar expansion model. [31]

The initial assumption of the model is that a plasma occupies the half-space $x < 0$ at time $t = 0$. The ions are at rest with density $n_i = n_{i0}$ $(x < 0)$ and no ions for $x > 0$ showing a sharp ion boundary. Whereas, the electrons have continuous profile corresponding to a Boltzmann distribution

$$n_e = n_{e0} exp\left(\frac{e\phi}{k_B T_e}\right) \tag{2.38}$$

where n_{e0}, ϕ and T_e are the initial electron density, electrostatic potential and electron temperature, respectively. The Poisson equation is feasible for potential

description.

$$\epsilon\frac{\partial^2\phi}{\partial x^2} = e(n_e - Zn_i) \tag{2.39}$$

where Z is the ion charge number. For a quasi-neutral state, $\phi = 0$, $n_e = Zn_i$. The continuity equation and equation of motion for the ion needs to be employed here to estimate the density and velocity of the expanding ions.

$$\frac{\partial n_i}{\partial t} + \frac{\partial(n_i v_i)}{\partial x} = 0 \tag{2.40}$$

$$m_i n_i\big(\frac{\partial v_i}{\partial t} + v_i\frac{\partial v_i}{\partial x}\big) = eZn_iE \tag{2.41}$$

In a quasi-neutral condition, substituting the Boltzmann equation 2.38 into the equation of motion, equation 2.41, gives

$$\frac{\partial v_i}{\partial t} + v_i\frac{\partial v_i}{\partial x} = -\frac{C_s^2}{n_i}\frac{\partial n_i}{\partial x} \tag{2.42}$$

$C_s = \sqrt{\frac{Zk_BT_e}{m_i}}$ is the ion sound speed and m_i is the ion mass. With an assumption of the isothermal condition, constant electron temperature, the plasma expansion can be described with the velocity, $\xi = x/t$. In order to solve equation 2.42, the continuity equation 2.40 needs to be used with the dimensionless variables defined as

$$(v_i - \xi)\frac{dn_i}{d\xi} = -n_i\frac{dv_i}{d\xi} \tag{2.43}$$

$$(v_i - \xi)\frac{dv_i}{d\xi} = -\frac{C_s^2}{n_i}\frac{dn_i}{d\xi}$$

The ion velocity from the equations above is

$$v_i = C_s + \frac{x}{t} \tag{2.45}$$

This ion velocity can be used with the continuity equation 2.40 to find a self-similar solution for the ion density. Also, for the integral, the boundary condition $n = n_0$ is applied for $x = -C_st$ at time t, meaning that a rarefaction wave moves toward $-x$ with the speed of C_s while the plasma expanding in $+x$. The ion density profile turns out to

$$n_i = n_0 exp\big(-\frac{x}{C_st} - 1\big) \tag{2.46}$$

In order to find a self-similar electric field, the momentum equation of electron is used which is

$$\frac{\partial P}{\partial x} + en_e E = 0 \tag{2.47}$$

where, $P = n_e k_B T_e$. Plugging in the eqution 2.46 into the 2.47 yields the electric field

$$E = -\frac{k_B T_e}{en_e}\nabla n_e = \frac{k_B T_e}{eC_s t} \tag{2.48}$$

Lastly, the ion energy spectrum can be obtained by combining two self-similar solutions of v (2.45) and n_i (2.46). i.e., using a relation between the kinetic energy and velocity, $\varepsilon_i = (m_i v_i^2)/m_i$ and taking the derivative with respect to ε_i, the number of ions per surface area and per energy is

$$\frac{dN}{d\varepsilon_i} = \frac{n_{i0} C_s t}{\sqrt{2\varepsilon_i Z k_b T_e}} exp\left(- \sqrt{\frac{2\varepsilon}{Z k_b T_e}} \right) \tag{2.49}$$

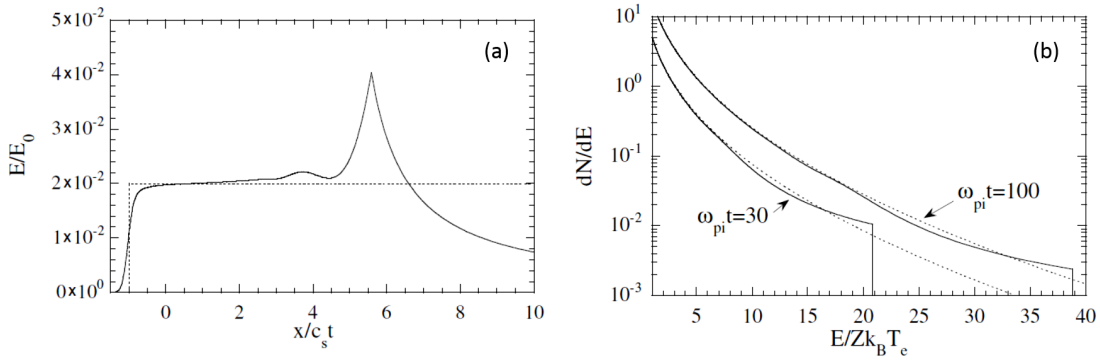

Figure 2.2: Results of Mora's 1D expansion model. The electric field at time $\omega_{pi} = 50$ showing a peak at the ion front position (a). Expanding ion spectrum per unit surface at $\omega_{pi}t = 30$ and 100. The energy and the number of ions are normalized by Zk_BT_e and $n_{i0}\lambda_{D0}/Zk_BT_e$ (b). The dotted lines indicate the usual self-similar solution for both plots.(images from [31])

Mora [31] found that this self-similar model is not valid when the initial Debye length becomes larger than the self-similar density scale length, $C_s t$, and expansion velocity goes to infinity without a limit. He extended the 1D expansion model to obtain more realistic approximation providing solutions of the electric field and the maximum ion energy during an expansion. The electric field at the

ion front is expressed as

$$E_{front} \simeq \frac{2E_0}{\sqrt{2e + \omega_{pi}^2 t^2}} \tag{2.50}$$

where ω_{pi} is the ion plasma frequency. In Fig.2.2(a), the evolution of this electric field is compared with self-similar model. The electric field estimated from his model clearly shows there is a peak at the ion front position. Using a ion front velocity he derived the cutoff energy, ε_{max}

$$\varepsilon_{max} \simeq 2\varepsilon_0[ln(2\tau)]^2. \tag{2.51}$$

Here, $\tau = \omega_{pi}t/\sqrt{2e}$ and $e \approx 2.7182...$ is Euler's number. This cutoff energies are presented on the ion energy spectrum in Fig.2.2(b) compared with the self-similar solution. The isothermal model however has a problem with its initial assumption that the electron energy is not dissipated in time over estimating the maximum ion energy. Based on 1D expansion model, further studies have been carried out. The adiabatic model was introduced [34] assuming that electrons lose their energy as they transfer energies to accelerating ions. Additionally, the adiabatic model with the thin foil case was studied with the evolution of the electron distribution function [35] explaining the rarefaction wave during the target expansion. The dependence of the proton energy on target thickness was in investigated by Sentoku [36]. He pointed out that electron recirculation is occurred not only at the rear side of the target but also at the front side by the sheath field for the thin foil. Thus, the peak proton energy is enhanced inversely proportional to the target thickness.

The plasma expansion models of isothermal [31] and adiabatic [34] are compared with the experimental results as a function of laser intensity [19] in Fig.2.4. As we reviewed before isothermal prediction (green circle) shows higher maximum proton energy than experimental data while the adiabatic model (two-phases model shown with green square) and the same model with 3D effects mimicked show more similar proton energies to experiment results. The trend that can be found from all models and experimental data is increase in maximum proton energy as the laser intensity rises. This is due to the increase of hot electron temperature depending on the laser intensity as reviewed from previous sub chapter. Additionally experimental data presents higher proton energy with thinner targets ($10\mu m$) than

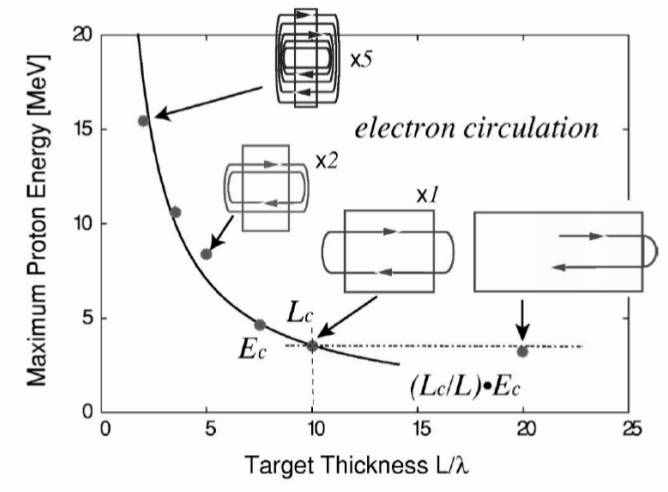

Figure 2.3: The maximum proton energy as a function of the target thickness obtained from 1D-PIC simulations. L is the target thickness and L_c is $2\times$ hot electron beam length. (from [36])

$25\mu m$ targets which is consistent with electron recirculation modeling as shown in Fig.2.3.

The laser energy as well as the intensity are crucial parameters affecting proton energy. In Fig.2.5, experimental data of the peak proton energy as a function of the laser pulse energy is shown. As target materials, the metal, dielectric and gas are presented with the squares, circles and triangles respectively. It shows generally, high proton energies from high laser energy in ps duration with the metal targets. As seen from the plot, high proton energies reported up to now are above 50 MeV; 58 MeV from a dielectric target with laser energy of 423 J ([28] shown in no.1 in the plot), 55 MeV from $10\mu m$ Al target with 310 J laser ([37] shown in no.15) and 67.5 MeV proton from a flat-top cone Cu target with 82 J laser ([38] shown in no.27).

2.2.2 Radiation Pressure Acceleration (RPA)

In the field of ion acceleration with a laser, radiation pressure acceleration (RPA) has become a topic of wide interest due to several computational studies which showed promise for producing high quality ion beams. Here, a brief mechanism of RPA will be presented closely following [19]. A high-intensity laser produce

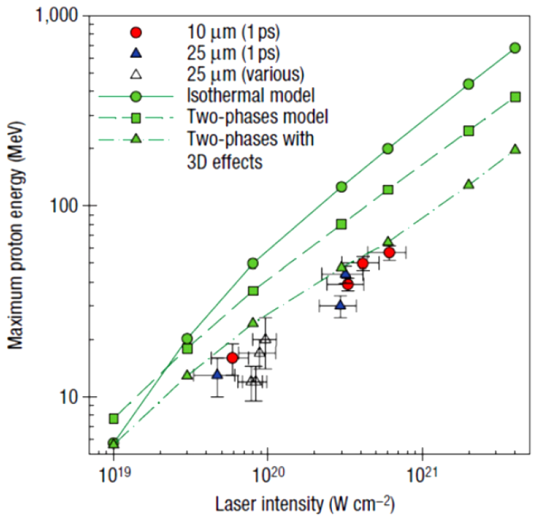

Figure 2.4: Peak proton energy as a function of laser intensity showing a comparison of plasma expansion models (isothermal and adiabatic models) with experimental data. (taken from [19])

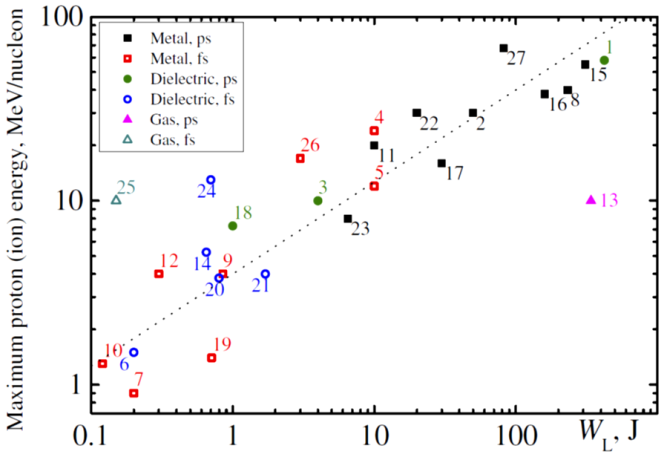

Figure 2.5: Experimental data showing the peak proton energy as a function of the laser pulse energy. The target material of the metal, dielectric and gas are denoted with the square, circle and triangles, respectively. The numbers correspond to references on the table2 in Daido's review [19] (image is extracted from [19])

an enormous radiation pressure at the reflection point on a foil surface, which push forward the electrons first. Due to a slow moving ions, the local electron-ion displacement forms and ions are accelerated through the ensuing space-charge field. If ions respond rapidly as those velocity is similar to electrons' velocity in a strong charge separation field, the distance between the electrons and ions will remain relatively small, and there will be no enough time for instabilities to be developed. The second stage is 'light sail' paradigm where the co-moving ions and electrons represent a relativistic mirror moving with the laser pulse. At a later time, a target is highly reflective with the laser frequency downshift in the co-moving frame. Also, double Doppler effect changes the frequency of the reflected light resulting in reducing reflected light energy meaning that the most of laser energy is transferred to the foil.

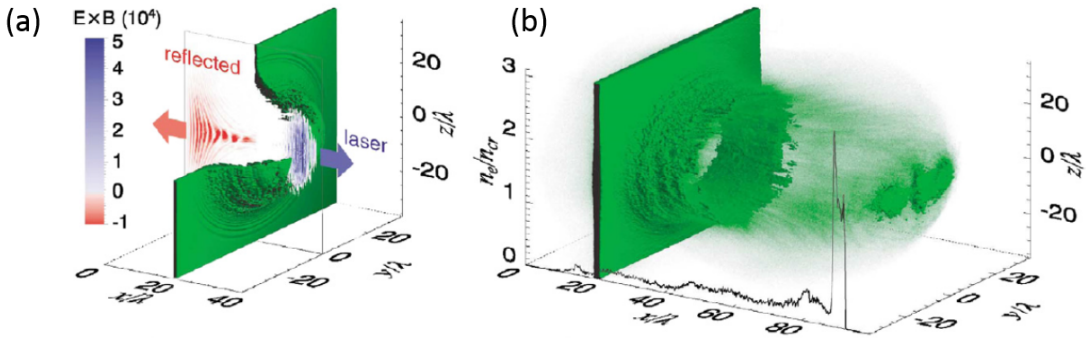

Figure 2.6: Snap image of 3D PIC simulation of ion acceleration. (a) Ion density isosurface for $n_i = 8n_{cr}$. Normalized pointing vector in the (x; y=0; z) plane, $t = 40 \times 2\pi/\omega$. (b) Ion density isosurface for $n_i = 2n_{cr}$ at $t = 100 \times 2\pi/\omega$. The ion density line out along the laser axis is shown in the black curve. (taken from [39]).

Esirkepov [39] showed 3D PIC simulation of the RPA regime. The extremely high laser intensity ($I > 10^{23}$) with pulse length of $ct_o = 8\ \lambda_o$ accelerates ions up to an energy of 1.5 to 3 GeV. Here, the non-relativistic instability growth time is 2.5fs (at the beginning of the pulse) while relativistic instability growth time is 0.06 fs. The target is accelerated as a whole without significant perturbation at the beginning. However, some instabilities cause proton energy spectrum which is close to mono-energetic but not a perfect one. If a target is relatively thick, the 'light sail' RPA mechanism is varied to 'hole boring' or 'collisionless shock' acceleration

process. Although, a laser pulse is reflected in a thick foil, an electron spike in front of the pulse forms charge-separation field driving ion acceleration. This process in a 1D model is described in Fig.2.7 showing the sharp rear edge of the ion and electron density and field between the ions and electrons. For this process, a circularly polarized laser pulse with target normal incidence have an advantage for ion acceleration due to that unperturbed electrons and ions, contrary to the ones oscillating in linearly polarized pulse, can be reflected by the laser ponderomotive force.

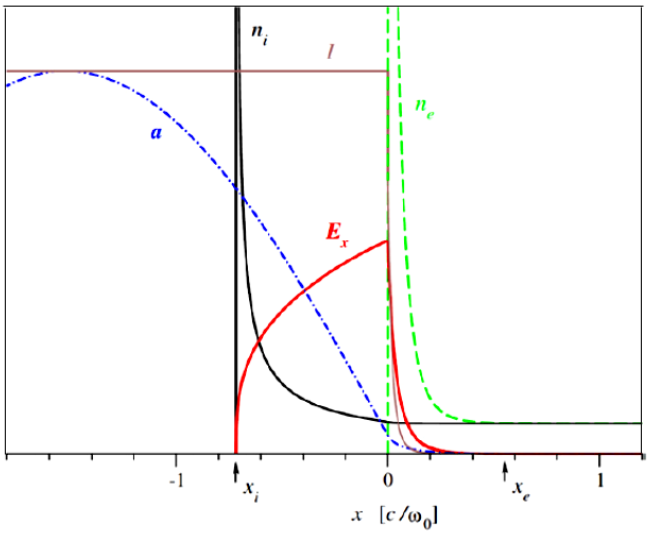

Figure 2.7: Quasi-stationary 1D model of hole boring process. The label n_i, n_e and E_x show ion density, electron density and charge-separation field. a and l indicate the amplitude and intensity of the standing wave by the incident and reflected waves. (from [40]).

The reasons of RPA mechanism attracting much attention recently is the accelerated ion energy and laser-ion conversion efficiency. Moreover, the RPA mechanism allows production of ion beams with solid density ($10^{22} - 10^{23}/cm^3$), which is significantly denser than the ion beam obtained from TNSA mechanism or classical accelerators. Mono-energetic characteristic of the ion beam can be also advantageous for wide range of applications.

2.3 Ion Transport and Stopping Power

There has been great interest in the energetics of charged particles moving through matter ever since the discovery of such particles. Studying this topic has extensively grown with the progress of theories for the atom and material structures providing better estimation of particles energy loss in a matter. This particle slowing down, generally called stopping power, is directly related to its energy deposition and transport dynamics and thus a big portion of physics that needs to be taken into account in our study. Here we will review theories of ion stopping power in different categories; stopping power in a cold matter, plasma and partially ionized states. We will begin with a general definition of stopping closely following [41] [42]. When a projectile such as proton, alpha particle or heavy ion, traverses a layer (thickness of Δx) of a medium, a portion of its kinetic energy, T_j, is transfered to the medium by collisions with the target atoms. The average energy a projectile loses by collisions, n_j of type j can be written as

$$< \Delta E >= \sum_j < n_j > T_j \tag{2.52}$$

Since the average number of collisions, $< n_j >$, is equivalent to $N\Delta x\sigma_j$, the equation 2.52 becomes

$$< \Delta E >= N\Delta x \sum_j T_j\sigma_j \tag{2.53}$$

where N is number density and σ_j is the energy loss cross section. Thus the stopping power can be described as

$$\frac{< \Delta E >}{\Delta x} = NS = N\sum_j T_j\sigma_j \tag{2.54}$$

Here, $S = \sum_j T_j\sigma_j$ is the stopping cross section. If we think about the case of a continuous energy loss, the stopping cross section will be

$$S = \int T\, d\sigma \tag{2.55}$$

where the differential energy loss cross section, $d\sigma = \frac{d\sigma(T)}{dT}dT$. Considering the impact parameter, p the closest perpendicular distance between a projectile and a

charged particle before deflection, in an ideal medium with free nuclei and electrons, differential energy loss cross section will be

$$d\sigma = 2\pi p dp \tag{2.56}$$

Then, the equation 2.55 turns out to be

$$S = \int T(p)\, 2\pi p dp \tag{2.57}$$

Solving this equation is essential concept for the stopping power of a charged projectile and is a starting point of Bohr's approach which is one of the stopping power calculation with the Bethe-Bloch model for a cold medium. Both approaches show similarities treating electronic stopping cross section but Bohr used the classical mechanics concept as we will briefly review. In Bohr's approach, each target electron is treated as a harmonic oscillator having a resonance frequency of ω_0 and its motion responding the electric field, $E(r,t)$ of the projectile is

$$\frac{d^2r}{dt^2} + \omega_0^2 r = -\frac{e}{m}E(r,t) \tag{2.58}$$

Here, the only term contributing to the energy transfer from the projectile to the target electron is the electric field. The transferred energy, T, can be found using the velocity of the electron which is from the solution of the equation 2.58. (detail derivations can be found in [41]).

$$T = \frac{1}{2m}\Big| \int_{-\infty}^{+\infty} dt(-eE(t))e^{i\omega_0 t}\Big|^2 \tag{2.59}$$

Now, we have the $T(p)$ for the equation 2.57. Integration of right hand side gives the electronic energy loss as a function of an impact parameter. To determine the range of the impact parameter for the integral, Bohr adopted Rutherfor's law for close collisions. Thus the impact parameters of minimum and maximum become Z_1e^2/mv^2 and v/ω, respectively. After insertion of impact parameters, the final Bohr's stopping model is given as

$$S = \frac{4\pi e_1^2 e^2}{mv^2} ln \frac{Cmv^3}{|e_1 e|\omega_0} \tag{2.60}$$

where $C = 1.1229$ and $e_1 = Z_1 e$.

With developing of quantal concepts, the first quantum stopping model was built by Bethe applying Born approximation, the perturbation theory of quantal scattering. In the Born approximation, the stopping cross section of an atom can be described as

$$S = \int Q d\sigma_R(Q) \sum_j f_{j0}(Q) \tag{2.61}$$

where $Q = \hbar^2 q^2/2m$ is an energy transfer, $d\sigma_R(Q)$ is the free Coulomb cross section and f_{j0} is the dipole oscillator strength. Solving the equation 2.61 is done similarly to Bohr's approach but instead of distinguishing collisions within a finite range of impact parameters, Bethe considered collisions based on the amount of momentum transfer. The integral of the equation 2.61 can be split into the low-Q contribution (S_{dist}) and high-Q contribution (S_{close}) with a criteria $(\hbar\omega_0)^2 < Q_0 < 2mv^2$. The final Bethe model turns out to

$$S = S_{close} + S_{dist} = \frac{4\pi e_1^2 e^2}{mv^2} Z_2 ln \frac{2mv^2}{I} \tag{2.62}$$

where lnI is the mean logarithmic excitation energy. For a heavy projectile, the relativistic Bethe formula is

$$S = \frac{4\pi e_1^2 e^2 Z_2}{mv^2} \sum_j f_{j0} \left[ln \frac{2mv^2}{\hbar\omega_{j0}} - ln(1-\beta^2) - \beta^2 \right] \tag{2.63}$$

Here, β is v/c. From the criteria for the integral above and $Q_0 << \hbar\omega_0$ for a harmonic oscillator provide a valid range for Bethe's model shown as

$$2mv^2 >> \hbar\omega_0 \tag{2.64}$$

indicating that the speed of projectile must be higher than the electron speed in a target.

As shown in the equations, 2.60 and 2.62, two models of Bohr and Bethe have a similarity. Later Bloch evaluated the differences and combined two models. His approach is using a cylinder confining electrons and introduced transverse momentum components under the electromagnetic interaction. With this approach, he found that Bethe's plane-wave approach for low momentum transfer and Bohr's classical approach for large momentum transfer are correct. His stopping formula

can be written as

$$L_{Bloch} = L_{Bethe} + \psi(1) Re\psi\big(1 + i\frac{Z_1 e^2}{\hbar v}\big) \tag{2.65}$$

Where $\psi(1)$ indicates the digamma function. In Fig.2.8, this stopping number L is compared with the Bohr and Bethe logarithm showing that Bloch's formula bridges two models.

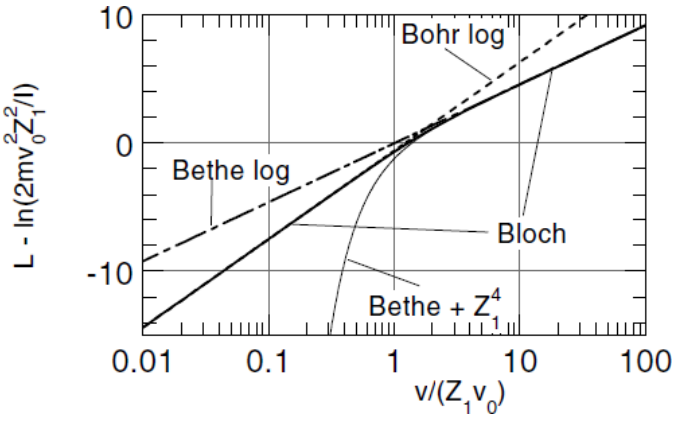

Figure 2.8: Bloch formula compared with Bohr and Bethe logarithm. (taken from [41])

The stopping theories we have reviewed are based on the binary collisions between a projectile and electrons in a target. Contrary to this approach, Lindhard described electrons excitations with a dielectric response function. We will review this approach beginning with a brief introduction of the stopping power in a free electron gas model following [43] [44]. In an ideal medium (uniform free electrons at zero temperature), a charged particle propagating in this medium induces an electric field due to a polarization of the medium. i.e., the response of this medium to a perturbation is the electric field and this field inhibits the particle propagation causing its energy loss. This electric field is associated with medium dielectric function $\varepsilon(k, \omega)$. Using the dielectric function of free electron gas found by Lindhard and Winther [43], the stopping power of an ion moving with velocity V can be described as

$$\frac{dE}{dx} = -\frac{4\pi}{m}\big(\frac{Z_1 e^2}{V}\big)^2 \rho L(\rho, V) \tag{2.66}$$

Where m, ρ are electron mass and density. L is the stopping function written as

$$L(\rho, V) = \frac{i}{\pi\omega_0^2} \int_0^{infty} \frac{dk}{k} \int_{-kV}^{kV} \omega dw \big(\frac{1}{\varepsilon(k,\omega)} - 1 \big) \tag{2.67}$$

Here, ω_0 is the plasma frequency.

The description of this stopping interaction function, $L(\rho, V)$, also includes the charge screening and plasma density fluctuations. Thus, in Lindhard's dielectric approach, both electron excitation and collective plasmon excitation are taken into account. For a case that electrons are formed nonuniformly in a medium, Lindhard model can be extended with local density approximation (LDA) where nonuniform electron medium is divided into small volume components and each component has uniform electron density. The stopping power of a projectile is calculated in each component and averaged value turns out to be the final stopping power. From this method, the ion stopping power can be written as

$$\big(\frac{dE}{dx}\big) = -\frac{4\pi}{m} \big(\frac{Ze^2}{V}\big)^2 \int_0^{\infty} \rho(r) L(\rho, V) 4\pi r^2 dr \tag{2.68}$$

$\rho(r)$ is the radial electron density distribution function. As expected from this approach, electron local density is important for the stopping power. To provide reasonable electron density, average atom model SCAALP can be applied [45]. We will compare stopping powers calculations of 'Bound+free model' and SCAALP model for a case of partially ioniezed matter in the Chapter 3.

Wang [44] extended Lindhard's model (zero temperature medium) to the stopping poewr for finite temperature case. The temperature dependent stopping was formulated by taking advantage of the random phase approximation (RPA) dielectric function developed by Maynard and Deutsch [46]. Now the general form of stopping power including temperature effects can be described as

$$\big(\frac{dE}{dx}\big) = -\frac{4\pi}{m} \big(\frac{Ze^2}{V}\big)^2 \int_0^{\infty} \rho(T, N, r) L(T, \rho, V) 4\pi r^2 dr \tag{2.69}$$

and the stopping function $L(T, \rho, V)$ is devided into two cases depending on the interpolation boundary velocity. Detail derivation of the stopping function will be skipped here.

In a dense plasma, strongly coupled system, the Debye length and the number of electrons in a Debye sphere are small. i.e., a Debye length is of the

order of the inter-particle spacing in a solid state plasma. When a charged particle (ion) propagates in this medium, it should experience collisions with electrons but also collective response of electrons (plasmon excitations) from beyond one Debye radius. Thus, ion stopping calculation in this regime needs to include both binary and collective processes. As we reviewed earlier, a plasma dielectric response function (in a free electron gas model) can be used for collective process outside the Debye sphere and binary collision theory can be applied within a Debye sphere. Following this approach, the plasma electron stopping power for an ion moving with speed V is introduced as [41] [47] [48].

$$\left(\frac{dE}{dx}\right)_{free} = \frac{(\omega_p Z_{eff} e)^2}{v^2} G(y_e) ln\Lambda_{free} \tag{2.70}$$

Where $G(\xi)$ is the Chandrasekhar function described with the error function as $erf(\xi) - 2\xi/\pi exp^{-\xi}$. y_e and Λ_{free} are $\left(\frac{m_e v^2}{2T_e}\right)$ and $\frac{0.764V}{b_{min}\omega_p}$, respectively.

$$b_{min} = max\left(\frac{e^2 Z_1}{m_{12}u^2}, \frac{\hbar}{2m_{12}u}\right) \tag{2.71}$$

Each term in the bracket is the impact parameter from classical(left) and quantal (right). m_{12} indicates the composition of the projectile mass and electron mass as shown as, $\frac{m_1 m_2}{m_1+m_2}$.

When an intense ion beam traverses a solid target, the target rapidly becomes a partially ionized warm or hot dense matter state. In order to study this beam transport and target heating, it is necessary to discuss the ion stopping power in a partially ionized (plasma) state. We already reviewed the dielectric approach with the local density approximation that can be applied for this partially ionized state but the most commonly used method (with its simplicity) for this regime is dividing the stopping power contribution from bound electrons and free electrons, called as bound + free model [47] [49] [50] [51]. The number of bound electrons and free electrons can be determined by the effective charge state of a target using the equation of state (EOS) or solving the Saha equation. This effective charge state Z_{eff} can be inserted in the general stopping power equation as

$$\left(\frac{dE}{dx}\right)_{total} = \left(\frac{dE}{dx}\right)_{bound} + \left(\frac{dE}{dx}\right)_{free} = K \times N\{(Z_2 - Z_{eff}) \times f_{bound} + Z_{eff} \times f_{free}\} \tag{2.72}$$

where N is the ion density, Z_2 is the target atomic number, f_{bound} and f_{free} respectively represent the bound and free electron contribution functions which could be specified by various models. For the computational studies presented in this work, the Bethe-Bloch model was chosen for the bound electronic stopping contribution and a stopping model of plasma free electron was adopted for the free electronic stopping contribution. These assumptions provide reasonably accurate results [47] [51]. The details about implementation of this stopping model for partially ionized systems are presented in chapter 3.

Chapter 3

Particle-In-Cell Simulation

A computational method for the study of plasmas is an effective approach to discovering novel physics, explaining the experimental observation, and is also a growing method with improving capabilities with high performance of computing. In computational simulations of plasmas, fundamentally different approaches, such as kinetic, fluid and molecular dynamics, can account for different regimes of physics in the plasma system. For simulations of laser-driven ions and ion-plasma interaction, the kinetic approach is suitable due to its capability of accurate and efficient interpretation for dynamics of high energy particles with a time scale from fs to 10s ps. In this kinetic approach, there are two plasma simulations, Particle-In-Cell (PIC) simulation and Vlasov continuum methods. The limitations found in each method are, respectively, the numerical noise from discrete particle effects in PIC simulation and the numerical dissipation as disposing of filamentations of the distribution function in the Vlasov method [52]. If a simulation requires many domains, it is known that PIC provides better resolution in velocity space. Since the kinetic simulation used for this work is a PIC simulation, more detailed information on the PIC simulation will, therefore, be discussed.

PIC code simulates the kinetics of plasma system using the sampling of particles, which move in space, including electromagnetic fields, and move under the force driven from those fields. Herein, these particles, called macroparticle, represent some large number of actual particles, such as ions and electrons. Therefore, the charge to mass ratio of macroparticles is the same as real particles, but obvi-

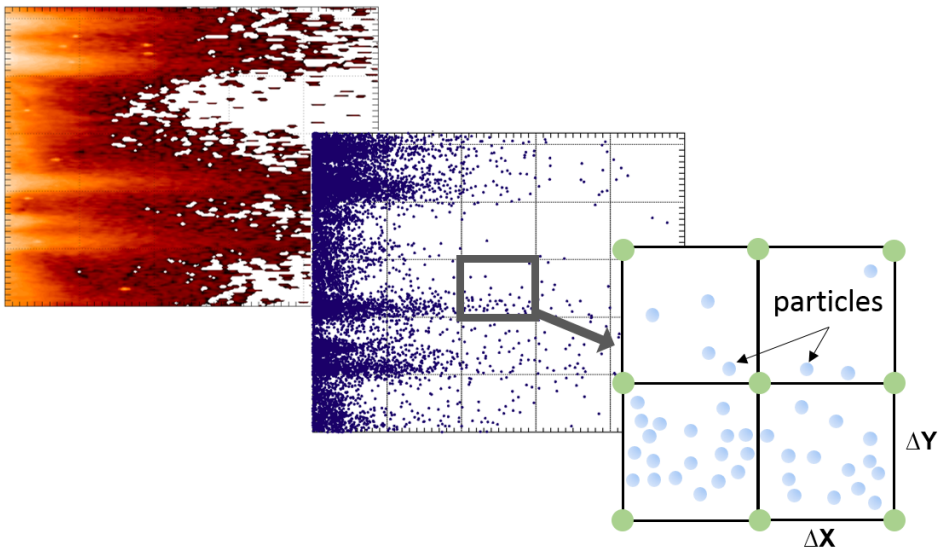

Figure 3.1: Macro particles in space represent real particles, ions and electrons. Shown images are (from left) density of hydrogen plasma, macroparticles representing continuous plasma and cartoon of macroparticles existing in grid cells

ously macroparticles have a higher charge and mass than real particles. As shown in Fig. 3.1, the quantities of macroparticles can be summed within single "cells" of a fixed grid to obtain continuous quantities, such as temperature, density, and current, which can then be used to solve for fields using Maxwell's equations. After the solving of electric and magnetic (EM) fields at discrete grid positions, these fields are interpolated to particle locations for particle push. This cycle, shown in Fig. 3.2, is a basic algorithm for PIC simulation and is repeated during the entire simulation time. An update of the EM field was conducted through Maxwell's equations and particle motion was driven by Lorentz force.

For PIC simulations, many studies have been carried out to develop methods and algorithms for interpretation of nature. Some of these methods and criteria in PIC will be introduced here, based on [53]. For communication of information, such as charge, current, and EM field, between particles in cell and grid points, particles are required to have a finite size or shape. The integral of these shape functions is the weight function, which indicates the fraction of particles in a cell, depending on particle shape and its position. Shape functions are commonly top hat (nearest grid point), triangle (linear), or spline. Among these, higher order

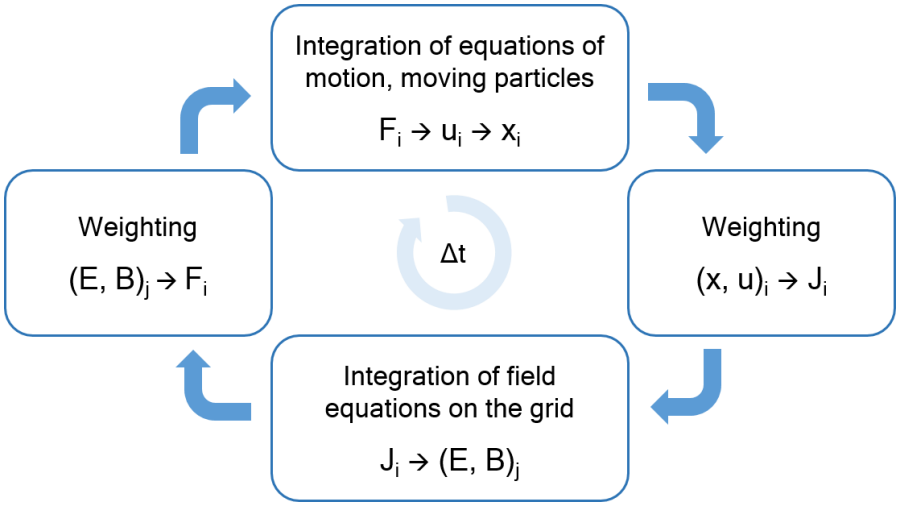

Figure 3.2: A typical cycle in a PIC simulation. From [53]. Particle and grid are respectively i and j.

spline has a better accuracy as the noise (statistical variations) can be reduced by averaging over couple of grids, which is called a cloud in cell (CIC) scheme. When particle motion is advanced through the equation of motion, $dx/dt = v$ and $mdv/dt = F$, a commonly used method to integrate these equations is the leap-frog method. In these first order differential equations, position, x, and velocity, v, are functions of each other. The leap-frog method calculates these two variables at different time steps, in a half step staggered manner. Likewise, this method can be applied to two variables, E and B, for advancing in time. This leap-frog method is straight forward and a fast explicit solver, but a smaller time step is required for stability. Once a magnetic field is involved, the advance of particle's velocity become complicated. The Boris scheme is a widely used method for the particle mover for providing long term accuracy in an explicit solver. The detailed introduction of this method will not be presented here. In the interpretation of plasma, there are restrictions on the PIC simulation. Basically, resolving a wave can be possible when the wave moves less than one cell per time step in EM field solving. Thus, the condition $c \times \Delta t < \Delta x$ is required. This time restriction becomes severe for higher dimensions. Time step restrictions regarding the plasma properties are $\Delta t < 1/w_{pe}$ and $\Delta t < 1/w_c$ where w_{pe} is the plasma frequency and w_c is the cyclotron frequency. Spatially Debye length and skin depth needs to be

resolved: $\Delta x < \lambda_d$, $\Delta x < c/w_p$. If the Debye length is not resolved, the temperature of plasma in PIC simulation will exponentially rise until it is resolved. All these temporal and spatial restriction are strict in explicit solver but those can be relaxed in implicit solver which will be discussed in the following sub-chapter.

3.1 LSP code and Algorithms

To simulate proton beam generation and beam-plasma interaction, Large Scale Plasma (Lsp) is used. The Lsp is the electromagnetic hybrid kinetic-fluid PIC code where the implicit method is included as well as all algorithms discussed in previous part. In this section, the algorithms in Lsp providing benefits to our work will be discussed following Welch [54] [55]

3.1.1 The Direct Implicit Method

The direct implicit algorithm employed in Lsp provides benefits of greatly relaxed limitation on time step indicating that resolving plasma and cyclotron frequencies are not mandatory. In the direct implicit algorithm, particle momenta are advanced twice: the electric field at the old position and time for the first half and new electric field from new position and time for the second half. This particle pushing is described as,

$$\mathbf{P}_{n+\frac{1}{2}} = \mathbf{P}_{n-\frac{1}{2}} + \Delta t[\mathbf{a}_n + (\mathbf{P}_{n-\frac{1}{2}} + \mathbf{P}_{n+\frac{1}{2}}) \times \frac{q}{2\gamma_n mc}\mathbf{B}_n(x_n)] \tag{3.1}$$

$$a_n = \frac{1}{2}[a_{n-1} + \frac{q}{m}\mathbf{E}_{n+1}(x_{n+1})] \tag{3.2}$$

where $\mathbf{P}$, $gamma$, m, q and c indicate momentum, Lorentz factor, particle mass, charge and light speed. $\mathbf{B}$ and $\mathbf{E}$ denotes the magnetic field and electric field. When the particle is pushed for the first time, theres no contribution of electric field, $\mathbf{E}_{n+1}(x_{n+1})$. For the second push, electric field is predicted using linear correction terms and gives a contribution to particle motion. The magnetic rotation is applied to solve the equation of motion that is described as, $\mathbf{P}_{n+1/2} = < \mathbf{T} > \cdot\mathbf{A}$, $< \mathbf{T} >$ is the magnetic field rotation tensor,

$$< \mathbf{T} >= \frac{1}{1+\Omega^2} \begin{bmatrix} 1+\Omega_x^2 & \Omega_x\Omega_y + \Omega_z & \Omega_x\Omega_z - \Omega_y \\ \Omega_x\Omega_y - \Omega_z & 1+\Omega_y^2 & \Omega_y\Omega_z + \Omega_x \\ \Omega_x\Omega_z + \Omega_y & \Omega_y\Omega_z - \Omega_x & 1+\Omega_z^2 \end{bmatrix} \tag{3.3}$$

where $\mathbf{\Omega} = \frac{q\mathbf{B}_n\Delta t}{2\gamma mc}$. $\mathbf{A}_1$ and $\mathbf{A}_2$ are used for the first and second push.

$$\mathbf{A}_1 = \mathbf{P}_{n-1/2} + \mathbf{a}_{n-1}\Delta t/2 + \mathbf{P}_{n-1/2} \times \Omega \tag{3.4}$$

$$\mathbf{A}_2 = \mathbf{E}_{n+1}(x_{n+1})\Delta t/2 \tag{3.5}$$

To calculate EM field before the second push, the susceptibility and perturbed current need to be given. The susceptibility determines the predictive electric field as its physical meaning of a material and is given as

$$< \mathbf{S} >= \frac{\rho q \Delta t}{2\gamma_{n+1/2}m}(< \mathbf{T} > -v_{n+1/2}v_{n+1/2}) \tag{3.6}$$

where v is the calculated new velocity. After these processes, the second particle push is applied. The current that is used in advancing electric field and the calculated current after the second push have a difference between two. This difference is accumulated during process and is corrected at a specified time steps. The EM field calculation follows Maxwell equation with the susceptibility term as shown below

$$\frac{\partial \mathbf{E}}{\partial t} = \nabla \times \mathbf{B} - \mathbf{J}^1 - < \mathbf{S} > \cdot\delta\mathbf{E}, \tag{3.7}$$

$$\frac{\partial \mathbf{B}}{\partial t} = -\nabla \times \mathbf{E} \tag{3.8}$$

These two equations are finite differenced as below

$$\frac{E_x|^{n+1}_{i+\frac{1}{2},j,k} - E_x|^{n}_{i+\frac{1}{2},j,k}}{\Delta t} = \frac{B_z|^{n+\frac{1}{2}}_{i+\frac{1}{2},j+\frac{1}{2},k} - B_z|^{n+\frac{1}{2}}_{i+\frac{1}{2},j-\frac{1}{2},k}}{\Delta y} - \frac{B_y|^{n+\frac{1}{2}}_{i+\frac{1}{2},j,k+\frac{1}{2}} - B_y|^{n+\frac{1}{2}}_{i+\frac{1}{2},j,k-\frac{1}{2}}}{\Delta z} - J_x|^{n+\frac{1}{2}}_{i+\frac{1}{2},j,k} - S_{xx}|^{n+1}_{i+\frac{1}{2},j,k} + E_x|^{n+1}_{i+\frac{1}{2},j,k} \tag{3.9}$$

$$\frac{B_x|^{n+1}_{i,j+\frac{1}{2},k+\frac{1}{2}} - B_x|^{n}_{i,j+\frac{1}{2},k+\frac{1}{2}}}{\Delta t} = \frac{E_y|^{n+\frac{1}{2}}_{i,j+\frac{1}{2},k+1} - E_y|^{n+\frac{1}{2}}_{i,j+\frac{1}{2},k}}{\Delta z} - \frac{E_z|^{n+\frac{1}{2}}_{i,j+1,k+\frac{1}{2}} - E_z|^{n+\frac{1}{2}}_{i,j,k+\frac{1}{2}}}{\Delta y} \tag{3.10}$$

where, n is the time step index and the index i, j, k represent Cartesian grid positions (x, y, z). Here only time derivative of EM field in x axis are shown. The one method to solve the above equation iteratively is using the Alternating Direct Implicit (ADI) solver where a large sparse matrix ends up a simple banded matrix. Non-iterative implicit electromagnetic field solver is also available. [55] The other method in Lsp is the Matrix solution which uses a matrix inversion procedure and a number of linear solution methods with pre-conditioning.

3.1.2 Hybrid-Fluid Method

Contrary to traditional PIC code, Lsp includes the nonrelativistic inertial fluid model. This hybrid-fluid scheme is more robust in terms of energy conservation which is particularly advantageous for long time simulations and the simulation with dense plasmas which generally cause problems of numerical cooling. This fluid model has the same equation of motion for electrons as the kinetic model except for scattering terms where the pressure gradient force term for collisions in a fluid and the frictional force term for collisions with other species are included, which accounts for the improved conservation. The equation including these terms is

$$\frac{3n_i}{2}\frac{dT_i}{dt} = -n_i T_i \nabla\cdot v_i + \sum_j \frac{2m_i n_i}{m_j \tau_{ji}}(T_j - T_i) + \nabla\cdot k\nabla T_i + \sum_j \nu_{ji}\frac{m_i m_i}{m_i + m_j}\left(\frac{P_i}{m_i} - \frac{P_j}{m_j}\right)^2 \tag{3.11}$$

In order, the each terms on the right-hand side are the pdV, energy exchange of species, thermal conduction and Ohmic heating rate where n_i, v_i and T_i are density, velocity and temperature. τ_{ji} is the thermalization time and k is the thermal conductivity. For some cases that hot electrons kinetic effects are important, electrons can be treated as either a free kinetic particle or a part of the fluid continuum in LSP. Using this option, an electron is treated kinetically if its kinetic energy, $\frac{m_e v_e^2}{2}$, is greater than the thermal energy, $\frac{3kT_e}{2}$, and treated as a fluid otherwise. It can switch between these treatments during the simulation.

3.1.3 Collisions and Stopping Calculation

In LSP, there are two built-in approaches to treat the collisions of charged particles. One is for relatively slow moving projectiles or particles in a background. The other approach is for high energy (relativistic) particles. The algorithm for collisions of slow-moving particles falls into one of two, statistical scattering method or a binary scattering method. The statistical scattering method, named "scattering" option in LSP, uses the Jones algorithm [56] [55] [57] which is a grid-based Coulomb collision model using a Maxwellian shape of the distribution of the momentum and temperature at each grid cell. For collision of interspecies, two pushes (momentum and energy) are applied shown as below

$$\Delta p_i = \Delta t m_i \sum_j \big[\frac{P_j}{m_j} - \frac{P_i}{m_i}\big]\nu_{ji} \tag{3.12}$$

$$\Delta T_i = \Delta t \sum_j 2m_i n_i \frac{2m_i n_i}{m_j \tau_{ji}}\big(T_j - T_i\big) + \frac{2}{3\gamma}\nu_{ji}\frac{m_i m_j}{m_i + m_j}\big\{\frac{P_i}{m_j} - \frac{P_i}{m_i}\big\}^2 \tag{3.13}$$

Where P, m, ν_{ij} and T are respectively the species average momentum, mass, interspecies collision frequency and temperature. With the equations above, the momentum and energy are transferred between two species by summing the changes from each interaction on grids. The Langevin equation describing Brownian motion is employed for collisions of intraspecies, and Spitzer formulation is applied to calculate the collision frequencies. The binary scattering method, the second option for non-relativistic particles, covers all the binary coulomb collisions between particles in each cell of the simulation grid. This method is especially beneficial for the particles having a non-maxwellian distribution but requires more computational resource. For the topic of this thesis, proton transport in a solid density matter, one thing that needs to be taken into account significantly is the protons stopping rate caused by collisions in a background medium. Because the protons considered here move fast (5MeV proton moves with the velocity similar to $0.1c$) and the solid medium is not fully ionized state, a continuous slowing down approximation of energy loss, "dedx" option in LSP, needs to be applied instead of the statistical scattering method or binary scattering method. This option

provides accurate stopping range of charged particles with energy loss calculation. The dedx option does not include intraspecies scattering but it can be very useful for the case that intraspecie scattering plays a small role. To verify that these options in LSP benchmark the physical stopping in an accurate way, test simulations were conducted to calculate proton stopping powers in LSP as measuring the energy loss and proton propagation distance every simulation time steps using low-density proton particles (test particle like). Those results are shown in Fig. 3.3. where the proton stopping power in solid aluminum using two options, "scattering" and "dedx", are compared to theoretical stopping calculation. As shown in Fig.3.3(a), simulation using the "scattering" option neglects the bound electrons' contribution to total stopping power. This is because the statistical scattering method is based on plasma condition. Whereas, "dedx" option, based on the Li and Petrasso [58] stopping power model, includes bound electronic stopping but still some distinctions are found as shown in Fig.3.3(b). Li and Petrasso model is based on Fokker Planck which is applicable for high temperature plasmas but is sensitive to coulomb logarithm [59]. For high density and low temperature background, coulomb logarithm < 2, this model may not be valid to cover this regime well.

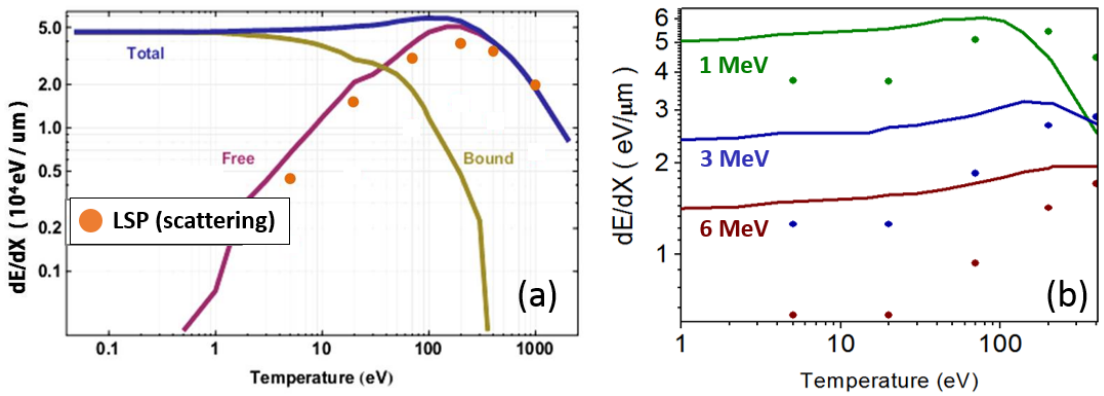

Figure 3.3: Comparison of theoretical stopping power with the measured stopping power from LSP simulation using scattering option (left) and dedx option (right). Solid lines represent theoretical calculation taken from [51] and lsp results are shown with circles.

To investigate proton transport in solid density or partially ionized warm

dense or hot dense matter, more accurate stopping power model in this regime was required to be implemented in LSP. In the following sub chapter, new stopping power module we implemented in Lsp will be discussed.

3.2 Implementation of Proton Stopping Power in LSP

The ion stopping calculation module we implemented in the LSP code is based on the electronic stopping, excluding nuclear stopping power. The nuclear stopping power is noticeable only at low ion energy ($< 0.1MeV$) and high target temperature ($\sim$ 1000 eV). For instance, the nuclear stopping power for a 0.1 MeV proton is less than 1% of the electronic stopping power in solid aluminum at 10 eV [60]. Through the transition of intense proton beams in a solid-density target, the target plasmas are often only partially ionized. The total stopping power of a proton beam in a target thus consists of contributions from two groups of electrons: those bound to the target ions and those that constitute the plasma free electrons. The commonly used approach for calculating ion stopping power in this regime is to formulate the two contributions separately, described as ad hoc bound + free model [47] [51] and reviewed in the previous chapter. This model is given as:

$$(\frac{dE}{dx})_{total} = (\frac{dE}{dx})_{bound} + (\frac{dE}{dx})_{free} = K \times N\{(Z_2 - Z_{eff}) \times f_{bound} + Z_{eff} \times f_{free}\} \tag{3.14}$$

where N is the ion density, Z_{eff} is the effective charge state with ionization, Z_2 is the target atomic number, f_{bound} and f_{free} respectively represent the bound and free electron contribution functions. $K = 4(Z_1 e^2)^2/m_e v^2$, where Z_1 is projectile particle atomic number (beam ions, $Z_1 = 1$ for proton beam). For bound electrons, we use the well-known Bethe-Bloch formula [42] with a shell correction [61] as $f_{bound} = ln(2mv^2/ < I >) - ln(1 - \beta^2) - \beta^2 - c/Z_2$, where v is the ion velocity, $\beta = v/c$ and $< I >$ is the averaged excitation potential per electron. For the averaged excitation potential, two scalings are used;

$< I > (Z_{eff}) = \frac{Z^2}{(Z-Z_{eff})^2} < I > (Z-Z_{eff})$ and $< I > (Z-Z_{eff}) = 16(Z-Z_{eff})^{0.9}$. The shell correction term C/Z_2 is based on the experimental shell correction method fitting bound electronic stopping power (for the cold state) to the NIST database. The density effect correction, which is only important for high-energy protons (>900MeV), [42] is excluded here. For the free-electron contribution, a stopping power model for plasma [47] [51] is considered by taking into account the contributions of both binary collisions and plasma oscillation excitation. This is formulated as $f_{free} = G(v/v_{th})ln(v/b_{min}\omega_P)$, where G is from homogeneous semi-classical Chandrasekhar approximation, b_{min} is the impact parameter, and the target thermal velocity, $v_{th} = \sqrt{T_e/m_i}$, which is determined by the target temperature T_e. The bound + free model requires the target charge state, z_{eff} due to the essential concept of separate contribution from bound and free electrons. In LSP, we used the prepared EOS table using the Prism Opacity and Equation of State (PROPACEOS) [62] for the update of Z_{eff} based on the instantaneous local density and temperature of a medium. PROPACEOS is modeled similar to the QEOS model for a regime of high density and low temperature and also provide the opacity data for elements of plasmas which include both LTE and non-LTE. Figure3.4 presents the zbar (charge state) in Aluminum as a function of temperature with different ion densities provided by PROPACEOS. With a decrease in the density, it is shown that Al ionized further as a target is heated.

By implementation of the above ion stopping calculation module in LSP, we now have the capability to model the proton stopping range and energy deposition profile as a function of density, temperature, and the degree of material ionization, which can vary from a cold solid target to a plasma state during proton beam transport. Fig.3.5 plots the proton stopping powers and projected ranges in Al targets from the LSP simulations with the new implementation. The contributions of bound and free electrons to the total proton stopping power at different temperatures are shown in Fig.3.5(a)-(b). We can see that the free electron contribution becomes more important and dominant as the target temperature increases. For a 50 eV fixed target temperature, the total stopping power decreases for protons with $<\sim 200keV$ and increases for higher energy protons compared to the cold

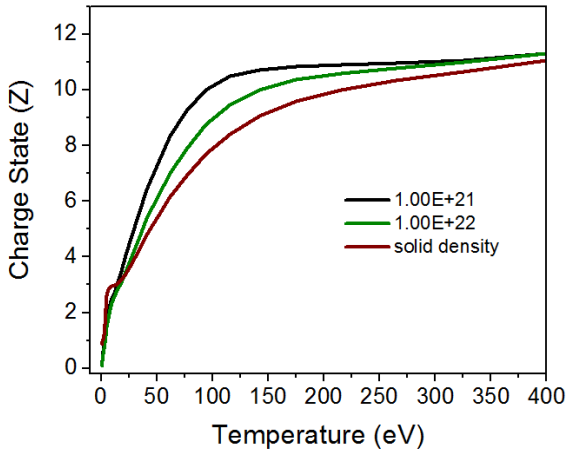

Figure 3.4: Ionization (charge) state curves of different densities in aluminum given by the equation of state (PROPACEOS)

stopping power (NIST data [63]) at room temperature, in which case bound electrons are the primary contributors to stopping power. Additionally, it can clearly be seen that when the target temperature increases, the peak of the proton stopping power shifts to higher energy ranges and becomes less steep. This is because the free electronic stopping power generally peaks when the beam proton velocity is near the background electron thermal velocity of the target [45]. Figure3.5(c) plots the calculated proton stopping power in solid aluminum as a function of proton energy for initial target temperatures of $T_e = T_i = 10$, 100, and 300 eV, using the new implementation of LSP. Correspondingly, the Bragg peak of the proton energy deposition curve obtained from the simulations, using a single test particle with energy 2 MeV, is flattened with increasing T_e, as shown in Fig.3.5(d).

Figure3.6 plots the projected ranges of protons in Aluminum (Al) and Copper (Cu) target as a function of target temperature for proton energies respectively of 2 and 5MeV. We can see that for both Al and Cu targets, the projected range of the low-energy protons at 2MeV increases monotonically with the rising target temperature, that is, they can propagate deeper into solid density matter by increasing temperature. In contrast, for protons with energy 5MeV, their projected ranges slightly decrease firstly with increasing target temperature ($< 100eV$), and

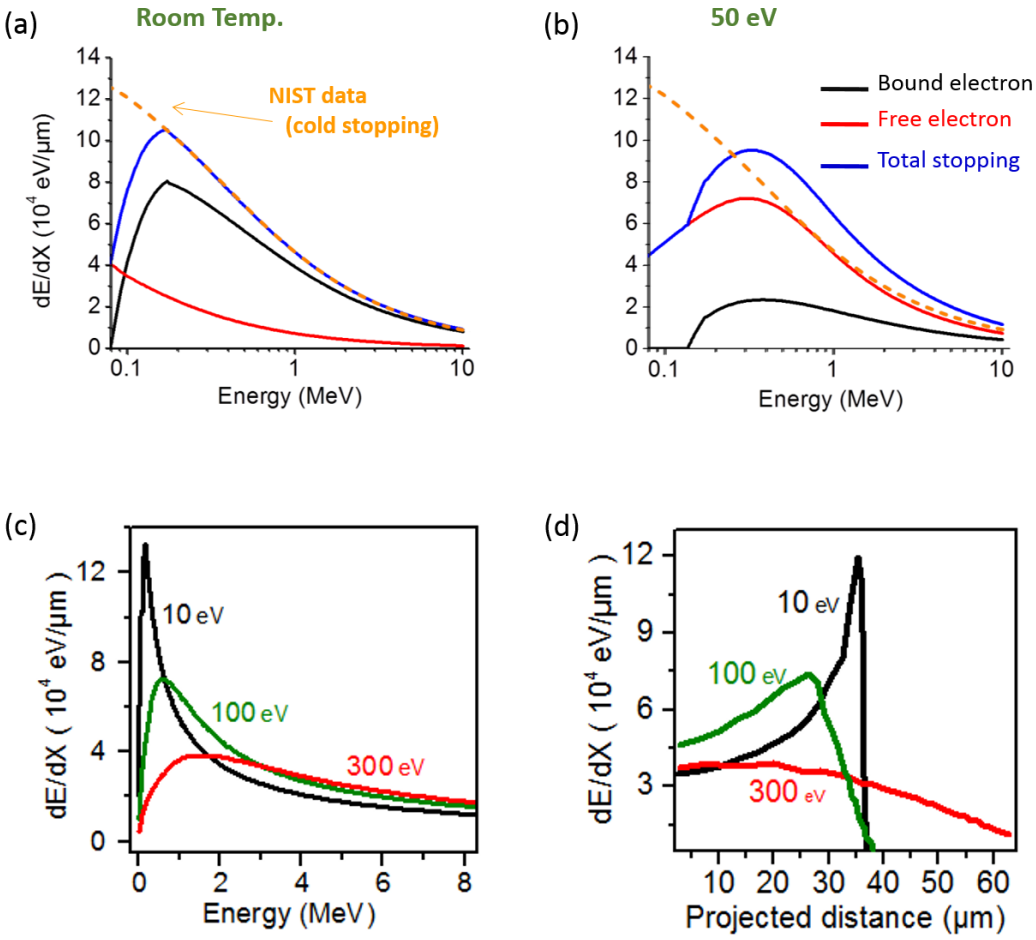

Figure 3.5: The contributions of bound (black, dotted-dashed) and free (red, dashed) electrons to the total (blue, solid line) proton stopping power in solid Al targets with temperatures of (a) room temperature and (b) 50eV from LSP simulation with the new implementation. The cold stopping power is shown as the orange dotted line [NIST]. (c) The calculated proton stopping power in LSP (with new implementation) as a function of proton energy with target temperatures of Te = Ti=10, 100, and 300eV; (d) Simulation results using 2MeV test proton particles showing stopping powers as a function of projected distance at different target temperatures.

then increases if the target temperature further increases ($> 100eV$). Since a copper target (higher Z material) has more electrons than a aluminum target, overall proton stopping power in Cu is higher showing lower projected range.

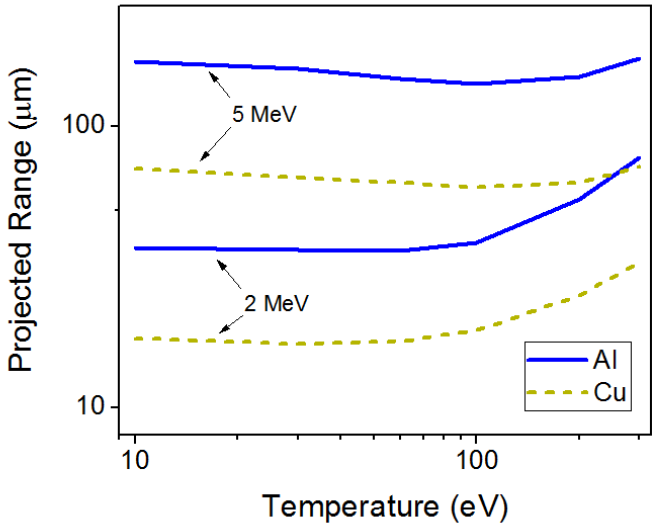

Figure 3.6: Proton projected ranges in Al and Cu targets as a function of target temperatures with different proton energies; 2MeV and 5MeV.

In order to benchmark the new implementation, we compare our simulation results with recent proton stopping calculation from a quantum theoretical model, self-consistent approach for astrophysical and laboratory plasmas (SCAALP), [45] which is based on the first-principles average-atom model and uses the dielectric formulation combined with local density assumption (LDA). [43] For stopping power calculations in the SCAALP method, inhomogeneous electron density (both bound and free) are taken into account by using sophisticated homogeneous stopping power values locally in an assumed spherically-symmetric confined ion. Obtaining such inhomogeneous densities requires the solutions to the nonlinear ordinary differential equations of density functional theory at every point in the simulation domain. This calculation in SCAALP is far more complicated to be coupled into a PIC code compared to our implemented module, where we make very different approximations as described above in order to have a stopping power expression that can be evaluated quickly.

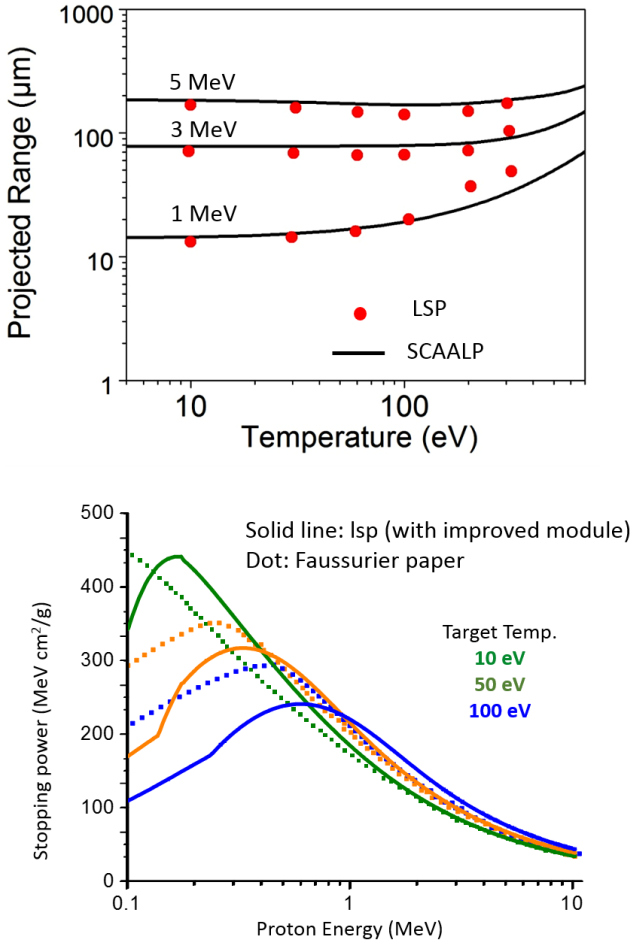

Figure 3.7: Comparisons of the proton projected ranges (top) and stopping power (bottom) in solid Al from LSP simulations with those from the SCAALP theory.

The results are plotted in Fig.3.7, for the projected ranges of protons in solid Al with different initial energies showing good overall agreement of both models. However, a little descrepancy exists for low energy proton (1MeV) at high temperature. This corresponds to stopping poewrs from both models shown in the plot (bottom) where stopping powers of two models show differences for proton energy below 1 MeV. Additionally, the empirical results of stopping power presenting nearly consistent to both two models were recently reported, [64] where proton stopping power for the solid density target in warm temperature (T_e 32 eV) slightly rises for high energy protons injected with initial energy of 15 MeV. We can see that the projected range of the low-energy protons (1MeV) increases with the rising target temperature above a few 10s of eV, that is, they can propagate deeper into a solid density sample by increasing its temperature. In contrast, for protons with energy ∼5 MeV, their projected ranges decrease for intermediate target temperatures (<100eV), and then increase if the target temperature further increases (>100eV). Note that this behavior of proton projected range varying with target temperature would happen automatically during the transport of intense proton beams in solid density matter, because the beam can heat the target up to several hundreds of eV, leading to complicated dynamics of beam transport which will be the topic of Chapter 5.

3.3 PIC Simulation of Ion Acceleration

Ion acceleration via TNSA mechanism has been modeled with PIC simulations including LSP [54] where contaminant layer or proton placed at the rear side of the foil are accelerated through electric fields formed by hot electrons. Analogous to previous works, we conducted LSP modeling of TNSA ion acceleration but here we focused on generation of two ion species in a curved target for focusing effect. Additionally, for efficient simulation (to reduce computational time), the electron source was used instead of sending an EM wave to accelerate hot electrons. The electrons sent in the target have a Maxwellian energy distribution of 3.2 MeV with the thermal spread of 1.7 MeV in 25 μm diameter (FWHM) area which are chosen

based on predictions of the electron population accelerated by a laser pulse with an intensity of 10^{20} W/cm^2 and a conversion efficiency of 30% from laser to electrons. The carbon hemi target with the mass density of 2.7 g/cm^3 has a diameter of 500 μm and thickness of 5 μm. The contaminants layer appended to the rear surface of the Hemi target includes both H+ and C4+. In reality, a thickness of contaminant layer on a target is only a few nm but in previous simulations modeling TNSA, various thicknesses ($50nm - 2\mu m$) were adopted in order to benchmark this layer and only a small distinction was found [65]. In this work, 0.25 μm (2 cells of the simulation) was used for the thickness of the contaminant layer. Accelerated protons and carbon ions are shown in Fig.3.8. As some of electrons passing through the Hemi target pile up at the back side a strong electric field (peak $E_z \sim 10^{12} V/m$ at early time, < 1 ps) is formed pulling protons and carbon ions out in z. Due to the mass difference, protons move much faster than carbon ions into a vacuum.

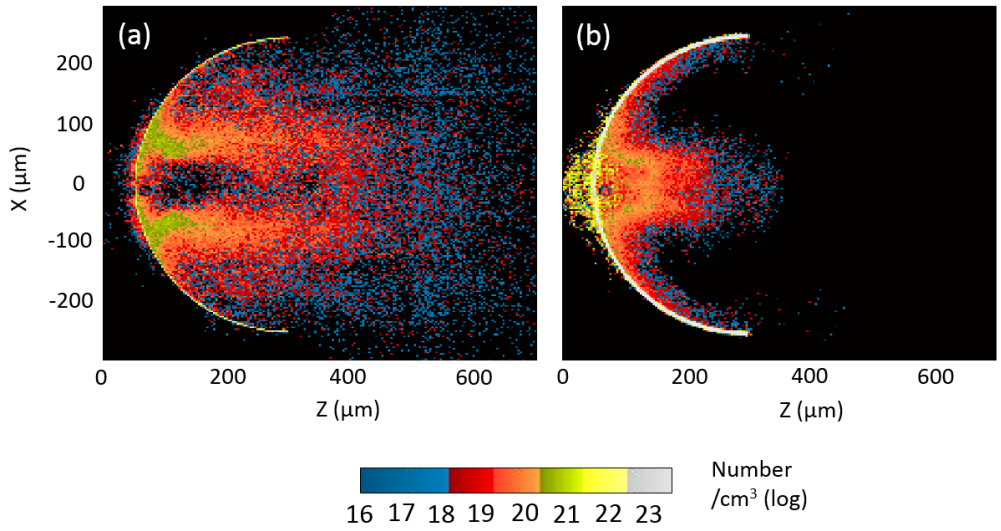

Figure 3.8: Simulation result of ion acceleration. Snap shots of proton density (a) and C4+ density (b) taken at 7 ps.

Proton trajectories that originate along the contaminant layer at different radial positions are also shown in Fig.3.9. It is clearly shown that proton particles are initially accelerated normal to the target, which is consistent with TNSA mechanism. Protons do not keep straight line as some of trajectories in the figure show, but they bend away from the axis. This phenomenon is more easily shown from

protons having relatively low energies produced from radially outer side from the axis. This bending effect has been studied in previous work [66] explaining that proton beam changes under the radial electric field which is set via hot electron pressure gradient described as

$$\mathbf{E}_r \approx -\Delta(P_e)en_e \approx kT_{ehot}/eR \tag{3.15}$$

where P_e, n_e, kT_{ehot} and R are respectively the hot electron pressure, hot electron density, hot electron temperature and radial scale length.

Fast moving (higher energy) protons have a relatively small divergence, presented in Fig.3.10(a). Similarly, Fig.3.10(b) shows a proton population with the divergence in Z direction where high energy protons behind the geometric focal distance ($250\mu m$) have a lower divergence ($< 45^o$) than ones close to the target. This PIC simulation as a prerequisite provided the confirmation that ion acceleration and focusing via geometry effect were modeled appropriately. Further LSP simulations performed to model experimental observations will be discussed in this dissertation.

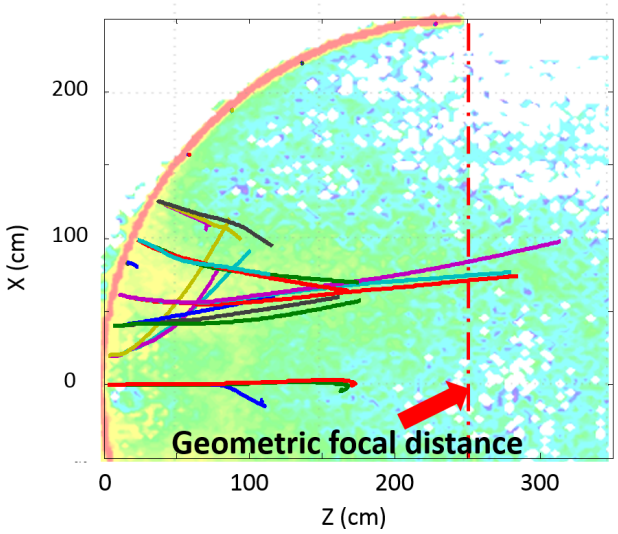

Figure 3.9: Trajectories of test proton particles originated at different radial positions.

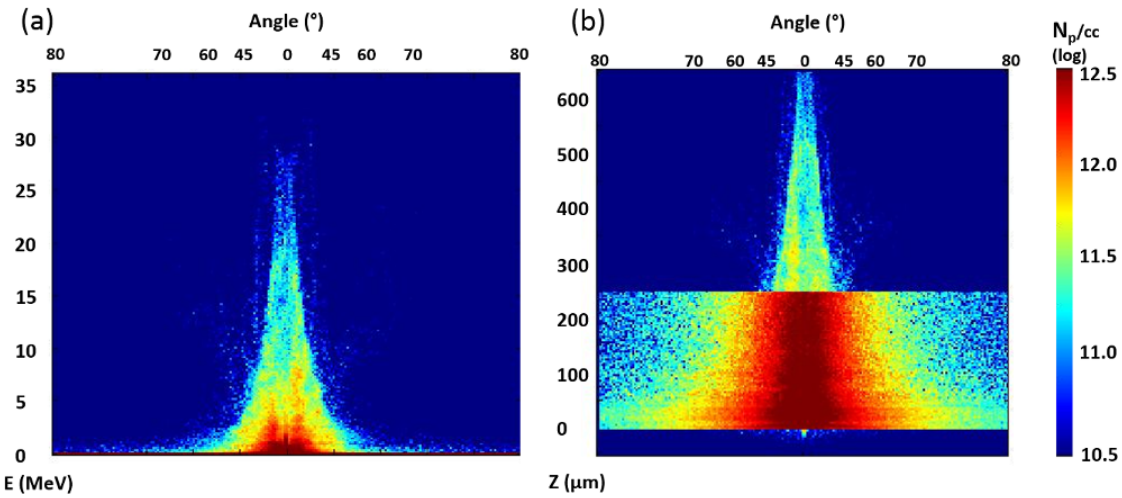

Figure 3.10: Characteristics of the proton beam generated from a Hemi target. Bean divergence vs proton energy (a) and beam divergence vs z (longitudinal axis) with proton density. Proton divergence angle is from arctan(Px/Pz).

Chapter 3, in part, is a reprint of the material as it appears in **J. Kim**, C. McGuffey, B. Qiao, M. S. Wei, P. Grabowski and F. N. Beg, "Varying stopping and self-focusing of intense proton beams as they heat solid density matter", *Physics of Plasmas 23, 043104 (2016)*. The dissertation author was the primary investigator and author of these papers.

Chapter 4

Intense Proton Beam Generation

As we discussed in Chapter 1, the generation of intense proton beams is important for applications such as the creation of warm dense matter and nuclear fusion energy. Particularly, for the fast ignition and heavy ion fusion scheme, many studies have been conducted to produce intense ion beams that can be useful for heating and compression of target fuel [29] [67] [68] [69]. When ion beams are produced by laser-solid interactions, the one way to make that beam intense is to collimate it efficiently. The other possible way is increasing the conversion efficiency of laser-to-protons to accelerate more protons from a given laser energy. In this chapter, we will discuss both methods for intense beam generation, while presenting results from both experimental and computational studies.

4.1 Proton Beam Focusing

Focusing of a TNSA beam was first demonstrated by Patel [29]. In his experiment, an intense laser irradiated either a flat Al foil or curved (hemispherical shell) Al foil. As the proton beams produced from these foils heated a secondary foil placed a fixed distance away, the spatial profile of heated region was observed via Planckian thermal emission on a secondary foil. In the flat foil case, the measured thermal emission region was broad (186 μm), while in the curved foil case, the emission size was narrow (46 μm) and its intensity was stronger than the flat foil case. These results clearly indicated the enhancement in beam flux by

focusing effects from the curved target. The further focusing effect has been found, with additional structure, along a curved target. In the experiments conducted by Bartal [67], different targets, including free standing and enclosed structure, were compared. In the case of an enclosed structure (cone shaped target), a smaller (more collimated) focal size of proton beam was found. PIC simulations [66], [70] explained the observed experimental results. Focusing effects with enclosed targets are due to hot electrons that escape the hemi-target and produce electric fields on the inside of the structure, pushing protons inward. Fig.4.1 presents the transverse electric fields for the two cases at 1.4 ps. For the hemi-cone target case, focusing fields are formed along the cone structure, while only weak fields are seen from the open-hemi target case. The hot electron population distributed on the target and cone structure (inset of the figure) correspond to the electric fields.

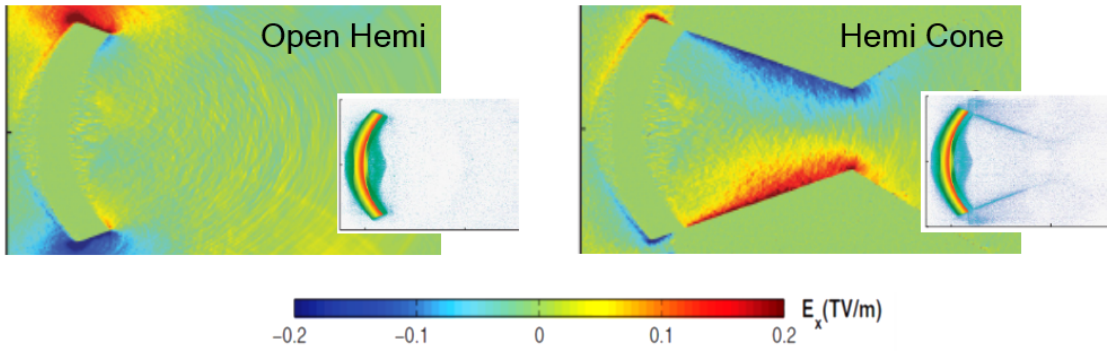

Figure 4.1: The transverse electric field at 1.4 ps on open-hemi target (left) and hemi-cone target (right). Hot electron density map at the same time is shown in insets. (Images extracted from [70])

In this thesis, further studies into beam focusing effects were conducted. We will first discuss the experiment carried out on the Omega EP laser facility. The basic concept of beam focusing, using an enclosed structure target, is similar to studies discussed above. The most unique feature of this work comes from the usage of a high energy and long pulse duration laser to produce intense proton beam. Also, measurement of a proton beam and visualization of a focused beam profile on a secondary foil are different from previous studies. Details of experimental and computational work will be presented in the following section.

4.1.1 OMEGA EP Experimental Setup

To produce intense proton beams, the experiment was conducted using the Omega EP laser facility with a 1 kJ laser energy and 10ps pulse duration. By using such a high energy laser, a high number of protons generated by TNSA mechanism are expected. Additionally, the laser continuously produces hot electrons during its long pulse duration of 10ps and electric fields maintained for a long time can be beneficial for collimating a proton beam while it propagates in the vacuum. In this experiment, two main diagnostics were employed to measure beam focusing effects. The usage of a Cu K_α imaging system aims to visualize the beam size at focus. For this imaging system, a foil with a Cu layer on its rear surface was placed at the beam focus. In addition, transverse proton radiography was used to watch the focusing fields associated with the target structures. Fig.4.2 shows a diagram of the experiment. One laser beam delivers an energy 1.25 kJ on the curved diamond-like-carbon (DLC) target within 35 μm radius R_{80} to produce a focused proton beam and another beam having an energy of 0.85 kJ heats the Si flat foil to generate protons for proton radiography. To record these probe protons (proton radiography), a RCF stack was placed 8cm away from the main target.

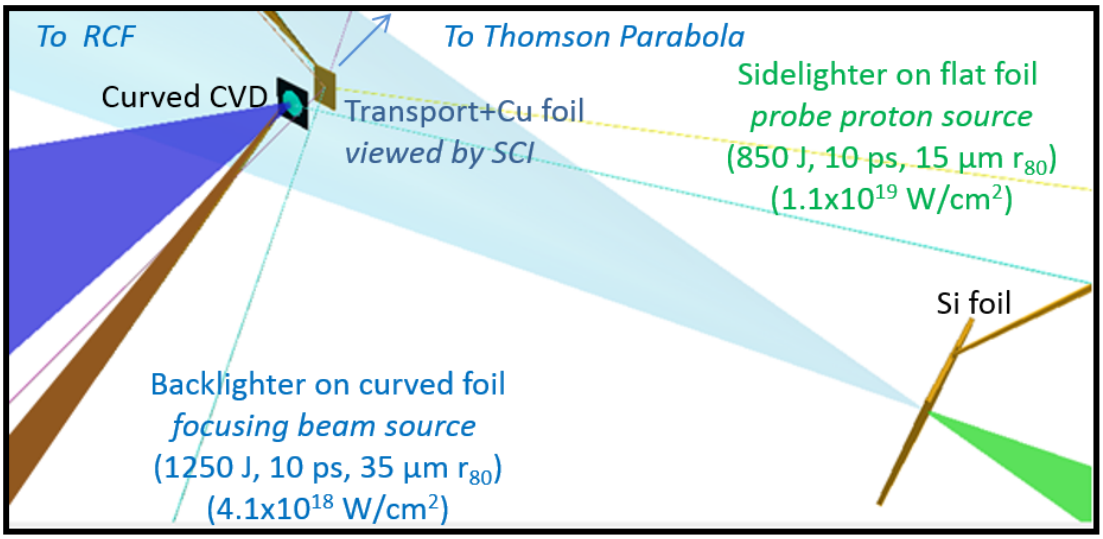

Figure 4.2: Diagram of the experiment set up. Two laser beams: Backlighter with $1.25kJ$, 10ps duration and $4.1\times10^{18}W/cm^2$ intensity. Sidelighter with $0.85kJ$, 10ps duration and $1.1 \times 10^{19}W/cm^2$ intensity.

For the comparison of proton beam focusing, freestanding and enclosed structure targets were used. As shown in Fig.4.3, structured targets have two types of geometries, the hemisphere-wedge assembled and hemisphere-cone assembled target. All targets have the identical hemisphere diamond like carbon (DLC) target with a $300\mu m$. diameter ($300\mu m$ geometric radius)

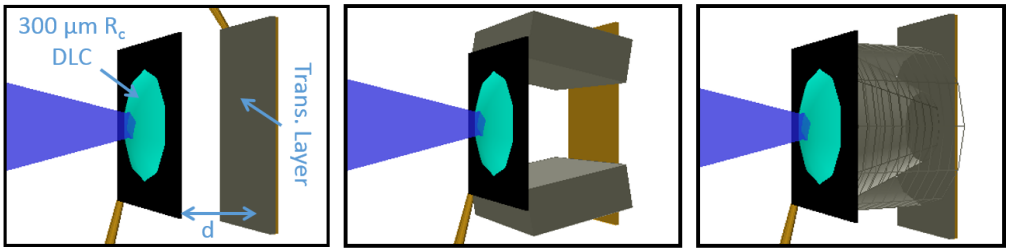

Figure 4.3: Target geometries. From left to right, freestanding target which is separated from the transport layer, wedge assembled target and cone assembled target. For all target types, the identical hemispherical target with $300\mu m$ diameter ($300\mu m$ geometric radius). Cu layer is added at rear surface of transport foils for Cu k_α detection.

We will briefly review two diagnostics, the Cu K_α imaging system and the Thomson parabola, as they were used in this experiment. Cu K_α is a type of x-ray emission. As illustrated in Fig.4.4, when an electron on the k-shell is kicked out by external energy source, such as electrons or protons, another electron positioned in the L-shell drops into the K-shell, releasing its surplus energy as radiation, called K_α photon, which has an energy near 8 keV. This Cu K_α signal has been widely used for characterizing the fast electrons produced by laser-solid interaction. When intense fast-electrons move in solid matter, electron impact ionizations (via the binary collisions) occur emitting K_α photons. This phenomenon indicates that Cu K_α radiation can provide, quantitatively, the amount of electrons passing through that region. The ionization can happen via proton collision with atoms, and this means that quantitative analysis of protons moving through the region is also possible. Figure4.5 shows the diagram of experimental setup of Cu K_α imager. For time integrated, spatially resolved (2D) emission image, a spherically bent crystal faces a target in which Cu K_α signal is produced by the interaction of the target with a laser pulse or particle beams. The angle for the crystal set up

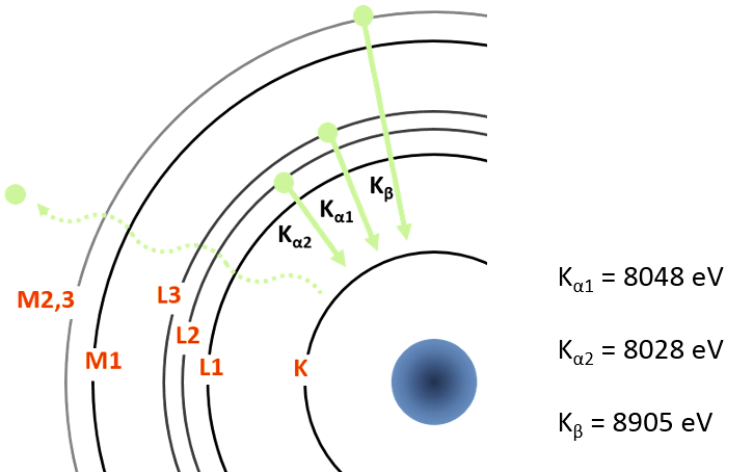

Figure 4.4: Illustration of Cu K_α radiation. When electron on K-shell is kicked out, an electron from L-shell falls down to the K-shell filling the vacancy and releases its energy in a form of X-ray photon. This Kalpha radiation has two energy states, 8048 eV and 8028 eV.

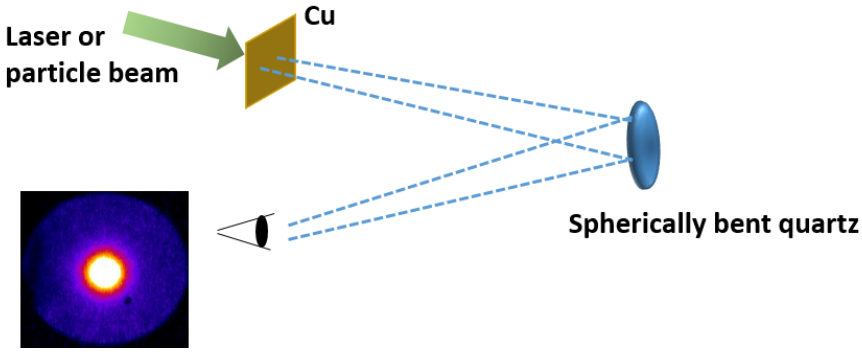

Figure 4.5: Sketch of the Cu k_α imager set up with a single crystal

is determined by the Bragg reflection.

The Thomson Parabola is a crucial diagnostic tool for detection and analysis of ions. With the Thomson Parabola, the energy spectrum of different ions can be measured through ions' different charge-to-mass ratios and velocities (energy). Essentially, the principle of this diagnostic can be described with the Lorentz force; the constant electric field deflects the ion path via the qE term of the Lorentz force, where the deflected range depends on the charge to mass ration. After separation by the electric field, ions experience a constant magnetic field in which the force given to ions is dependent on ion velocity. This composition of forces, driven with an orthogonal direction by electric and magnetic fields, makes a parabola shaped lines on the detector plane, as shown in Fig.4.6. Since each ion has a unique trace on a detector, ion species can be differentiated. However, the ions having a similar charge to mass ratio or high energies give a difficult identification due to the similar traces. For a detector, the highly sensitive image plate or microchannel plate (MCP) are widely used.

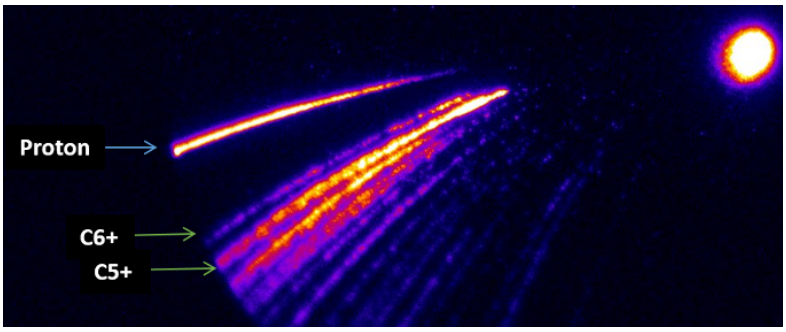

Figure 4.6: Ion species obtained from the Thomson Parabola.

The detailed ion position (parabola) on a detector plane can be described with a geometry parameters shown in Fig.4.7. As a particle having a mass m, charge Q and velocity v_o passes through a magnetic field, B_o, deflection of the particle to x-axis can be mathematically presented as

$$x = \sqrt{r_g^2 - w^2} - r_g - \frac{w(D-w)}{\sqrt{r_g^2 - w^2}} \tag{4.1}$$

where $r_g = v_0/\omega_c$ is the curvature radius of the trajectory and $\omega_c = QB_0/m$

Deflection in y-axis due to the electric field is

$$y = \frac{a_E u}{\omega_c(r_g^2 - w^2)}\left(\frac{u}{2\omega_c} + (d - w)\right) \tag{4.2}$$

where $a_E = QE_0/m$. Detailed derivation can be found in [71]

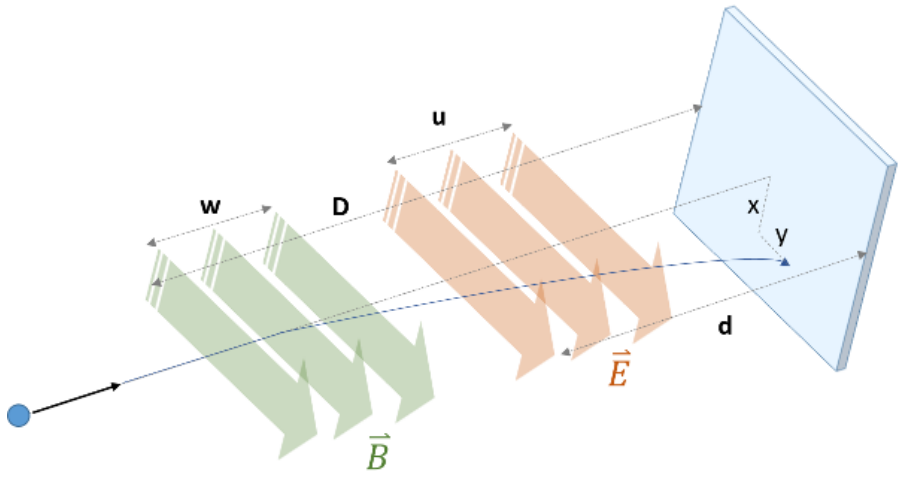

Figure 4.7: Schematic of a Thomson Parabola spectrometer. Charged particles are deflected by the electric field and the magnetic field showing a parabola trajectory on a detector.

4.1.2 OMEGA EP Experimental Results

The images of the Cu K_α emission on the Cu foil with different target types are shown in Fig.4.8, where the signals were corrected for differences in filters and laser energy for all shot data. From a comparison of these three cases, an increase in emission brightness with structured target is clearly visible. The weak emission over the entire Cu foil from the freestanding case and a stripe-shaped emission from the wedge assembled target were observed. The highest brightness was seen from the cone-assembled target. The quantitative analysis also shows that the total coupling to the foil was enhanced with the structured targets. Comparing to the freestanding case, the peak emission was increased for the wedge target by a factor of 5 and a factor of 8 for the cone target. Since a higher flux of particles traversing in Cu foil results in brighter emission signals, these results clearly indicate that proton

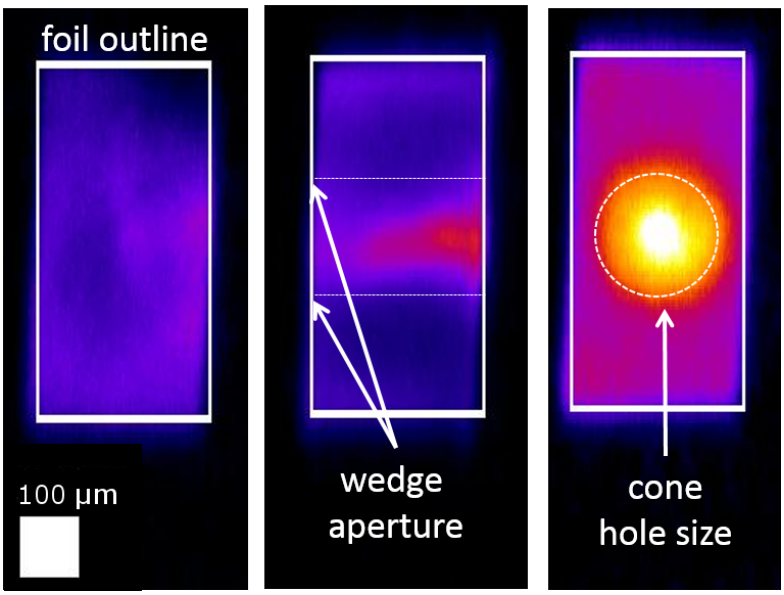

Figure 4.8: Cu K_α images detected on the Cu foil with different target types. The target types corresponding the images are (from left) free standing, wedge assembled and cone assembled target. All signals were corrected as the filter and laser energy were taken into account.

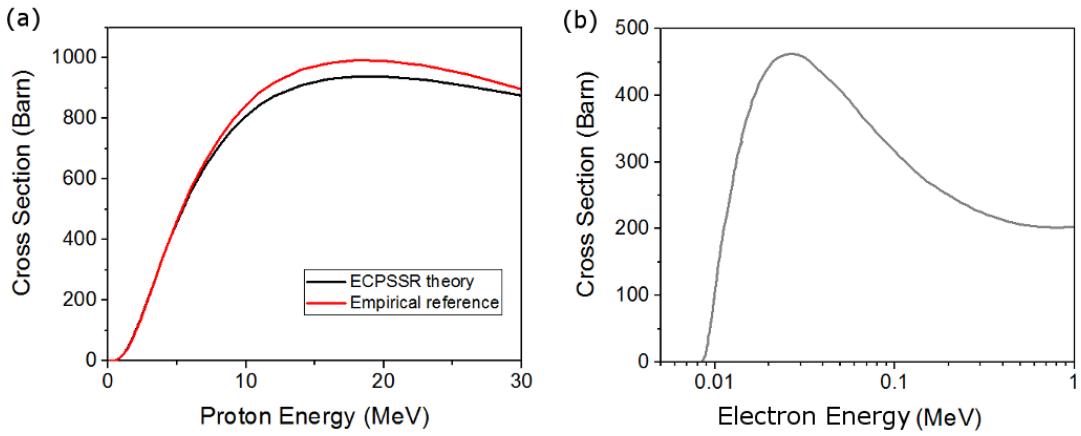

Figure 4.9: Cross-section for K-shell ionization in copper. (a) Proton induced ionization. Cross sections are obtained from ECPSSR theory and empirical data. (b) Electron induced ionization. The plot is extracted from [65]

beams with higher density are produced from structured targets. Fig.4.9 presents cross-sections for K-shell ionization in copper induced by protons and electrons. In the case of protons, cross sections from ECPSSR theory (energy loss coulomb repulsion perturbed stationary state relativistic theory) and empirical data are compared [72]. In proton beams generated by the TNSA mechanism, electrons co-moving with protons have much less energy ($<$ 100 keV) than simple proton energy (up to $\sim$20 MeV). For both proton and electron in those energy ranges of TNSA beam, the proton induced K-shell ionization has higher cross sections, as shown in the Fig.4.9. Thus, it can be inferred that the Cu K_α emission measured in the experiment is dominantly induced by protons, rather than co-moving electrons in the beam.

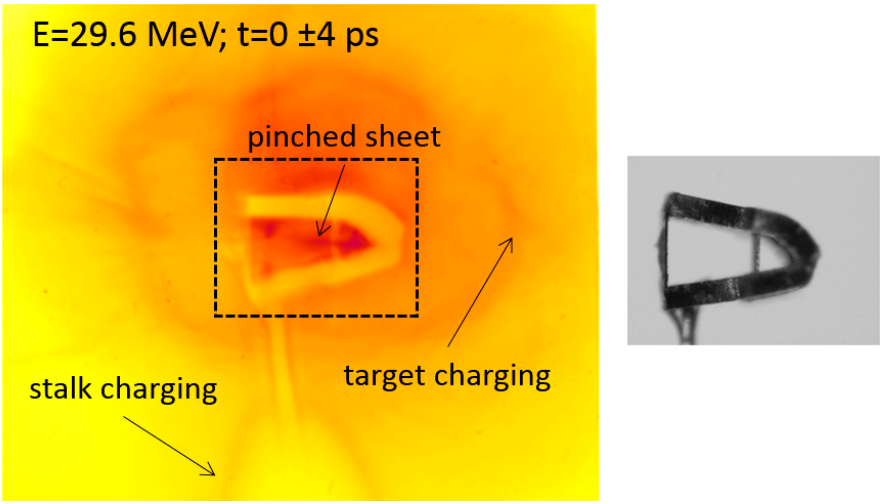

Figure 4.10: The results of proton radiography showing field effects around the wedge target and the target side view. The radiographpy image represents proton energy of 29.6 MeV.

The probe protons projecting the wedge target were recorded on the Radiochromic film (RCF) stacks that were placed 8cm away from the target. These probe protons (proton radiography) show field effects around the wedge target, and the evolution of fields (temporal resolution of several ps) can be analyzed since each RCF layer represents a specific proton energy. We will review the RCF diagnostic in the following subchapter. The probe proton image in the Fig.4.10 shows features of the wedge target at very early time (a few ps after the laser

interaction with the hemisphere target). As the main laser is incident to the hemisphere target, hot electrons are accelerated and move through out the structures, driving the charge fields. Corresponding to these fields, weak cloud-shape dark features are seen around the target structure where the projected probe protons are deflected outward. The stalk attached to the target also charges up, as shown in images. The most interesting feature is the dark horizontal band on the laser axis (plane of symmetry of the wedge), indicating that probe protons are deflected toward the laser axis. Thus, it can be inferred that radial electric fields driven from the wedge inside the walls pushes protons toward the plane of symmetry. Initially, the dark band originates from the rear of the wedge (near the transport foil), as shown in the figure, but eventually is seen from all over the plane, including the front side (near the hemi-target). For a better interpretation of these features, a computational modeling was required. Details of the simulation results will be discussed in the following subsection.

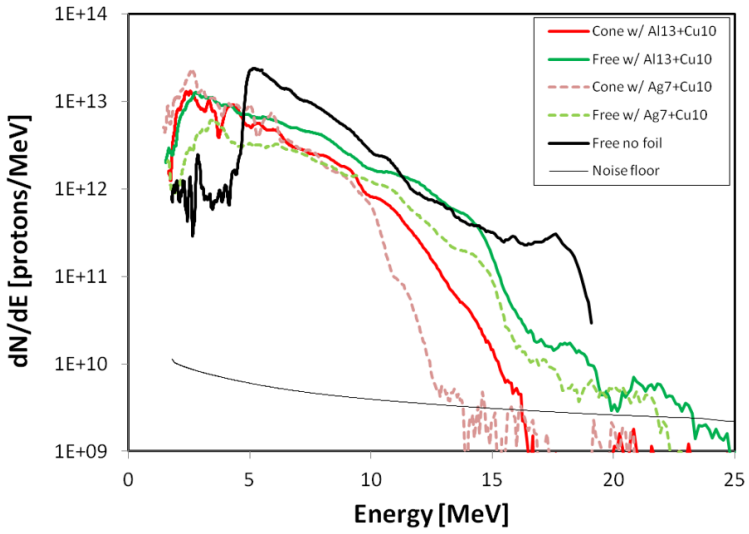

Figure 4.11: Proton energy spectrum measured by Thomson Parabola. Results of the cone target case and freestanding target case are presented with red and green respectively. The different materials of transport foils are shown with dotted line (Ag) and solid line (Al). Black solid line presents the result of freestanding target without a transport foil.

Focused intense proton beams were measured through the Thomson Parabola

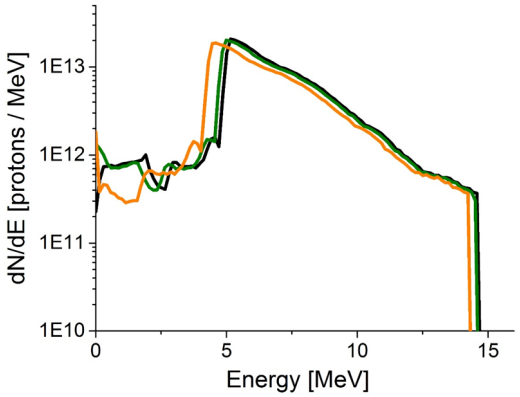

Figure 4.12: Proton energy spectrum obtained from the simulation (without field effects) where input proton data (shown in black) is from the freestanding target case without a transport foil. Energy spectrum of proton beam after passing through Al foil are shown in green (Al thickness of 6 μm) and yellow (Al thickness of 16 μm) .

to obtain the total proton beam energy and its energy spectrum. The source proton spectrum from the freestanding target without a transport foil showed a total energy of 46 J, which is approximately 3.5% of the laser energy, and a slope temperature of 2.7 MeV with a cutoff below 5MeV, as shown in Fig.4.11. An interesting feature from this proton spectra is the tailored energy distribution when proton beams traverse through the transport foil. This energy spectrum showing a decrease in proton numbers for high energy range ($> 5MeV$) and enhanced proton numbers for low energy ($< 5MeV$), and also shows the dependency of the foil materials. This energy variation is bigger than the proton energy loss expected with stopping power in the foil as plotted in Fig.4.12. For the analysis, an LSP simulation was run where the source proton spectrum was injected into Al foil and its varied energy recorded. Since this simulation was conducted without field effects, it provides only the influence of the stopping power. Therefore, it is inferred that the fields formed around transport foils could possibly affect proton beam profile. This is interesting physics, but is out of the range of the study for this section, future studies will be helpful for further explanations.

4.1.3 Computational Modeling

The experimental results were supported by LSP modeling that verified the focusing effect we found in the experiment. Concretely, understanding of a source for the Cu k_α signal on the foil and evolution of fields that can explain the proton radiography results are the objectives of simulation modeling. Since a PIC simulation with large solid density target structures in 3D is extremely expensive, in this work, 2D simulation was done. Thus, the wedge type target showing 2D effects was chosen to be modeled, instead of the cone assembled type. The electron source based on the laser parameters was injected in the hemi target assembly with a wedge structure with the same geometry of the experimental target, as shown in Fig.4.13. The electron source has a slope temperature of 0.5 MeV with 50 μm

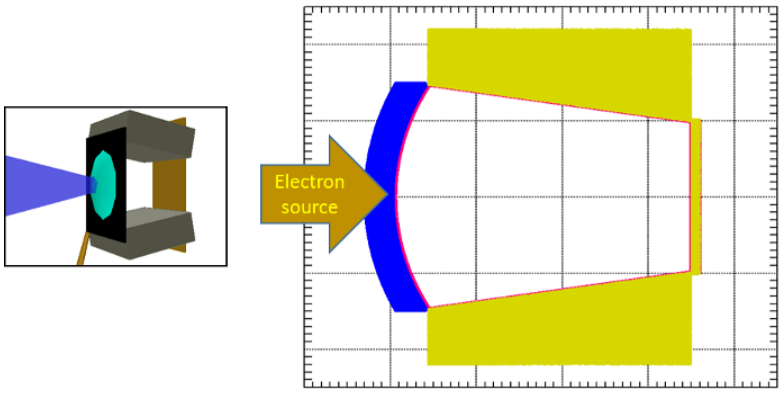

Figure 4.13: The diagram of the simulation modeling of the wedge target case. Simulation setup in 2D shows hemi-target and wedge structures

diameter (FWHM) and a total energy of 120 J, which is approximately 10 % of the laser energy. Since this electron source has a 10ps duration, the same as the laser pulse duration, the injection plane of the electron source to the target would be heated to unrealistic temperatures, and high density electrons inevitably locating around that region would require high resolution of PIC simulations. To avoid this problem, the electron source pulse was split into 3 sections (each section has a 3.3 ps duration) and injected from slightly different planes on the same longitudinal axis according to the order. In the simulation, the minimum grid size covering the hemi target region was 80 nm, and coarse non-uniform grids were set for vacuum area

in a time step of 0.2 fs. Injected hot electrons begin spreading toward z direction

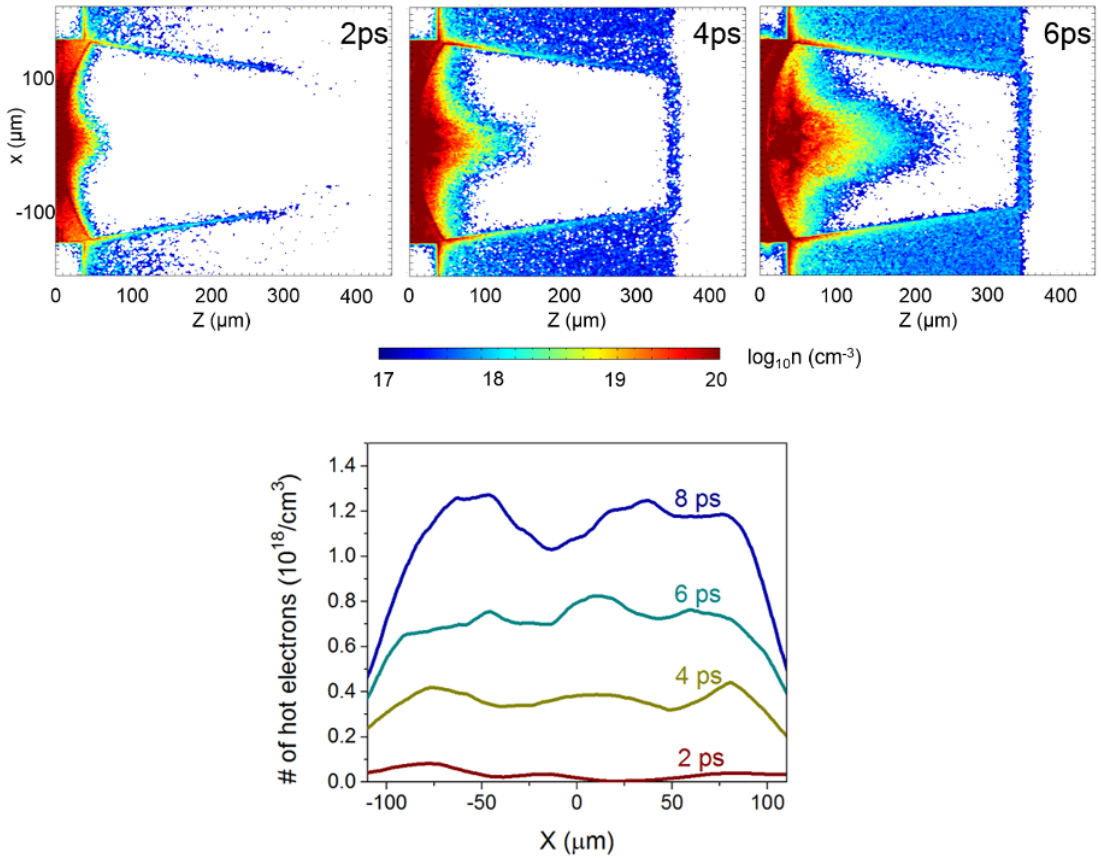

Figure 4.14: Injected hot electron density maps in different time showing electrons migrating to the foil through the wedge structure and dense slow-moving electrons in a beam. The lineouts of the electron density in the foil are plotted (bottom) with different time.

and along the wedge structure, as shown in Fig.4.14. Most electrons (high density electrons $\sim 10^{19}/cm^3$) are accumulated at the hemi-vacuum region, contributing to the proton acceleration (TNSA) and fewer electrons ($< 10^{18}/cm^3$) move towards the transport foil where we detected the Cu K_α signal in the experiment. The number of electrons reaching to the foil increases over time, as plotted in Fig.4.14, where the lineout of transverse (x direction) electron number density is taken from the middle depth of the transport foil. As shown in the plot, the electron density in the x-direction is uniform, giving an indication that the peak Cu K_α emission at central region does not include contributions from these pre-arriving

hot electrons. Additionally, the density of the driven proton beam (protons and co-moving electron) is an order higher than that of the electron density, which migrates through the wedge structure into the foil. Thus, it is quite obvious that the concentrated Cu K_α emission is representative of the proton beam, as shown in Fig.4.15

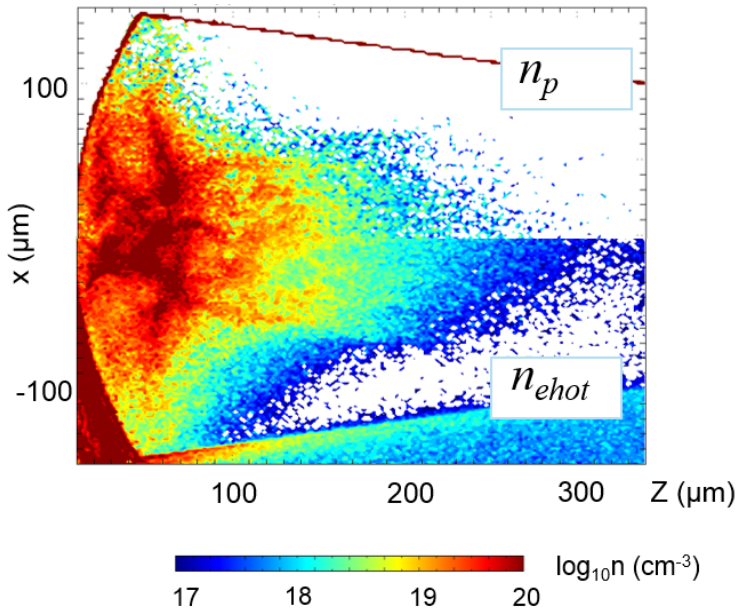

Figure 4.15: The density maps of protons and co-moving electrons at 8ps

The evolution of electric fields associated with hot electrons and proton beams is obtained from the simulation. Figure.4.16 presents longitudinal electric field (E_z) in time. 1ps after the hot electrons injection, a strong sheath field that accelerate protons (TNSA) is seen at the rear surface of the hemi target and get weaker over time. After hot electrons reach to the foil ($\sim 2ps$), negative fields are built at the inner surface of the foil (toward the hemi) where these fields may affect proton beam expansion in a vacuum. Both a strong TNSA sheath and fields near the foil gradually disappear over time. Electric fields in the transverse direction (E_x) are shown in Fig.4.17. The edge of the field moving toward the rear foil shows the position of the fastest hot electron moving through the wedge at 1 ps. We can see the uniform electric fields pointing the symmetry plane of the wedge and these fields are continuously maintained at times up to 8 ps. As the proton

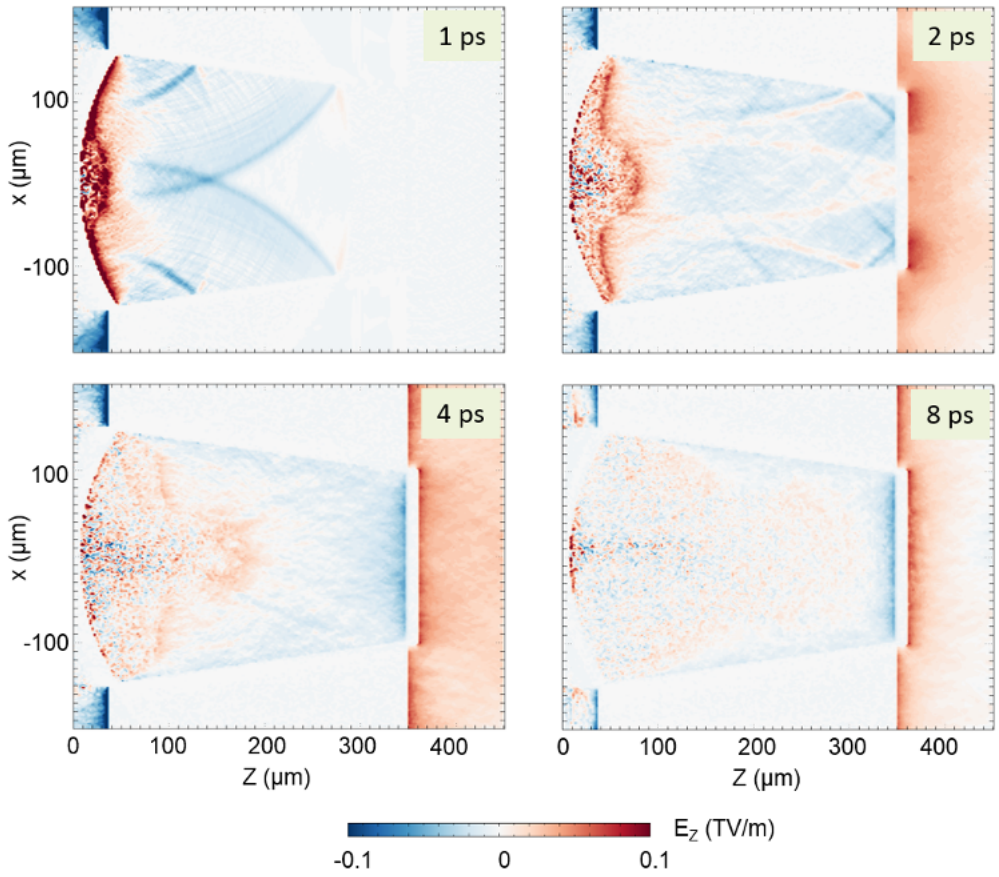

Figure 4.16: Snapshots of longitudinal electric field, E_z, in different time

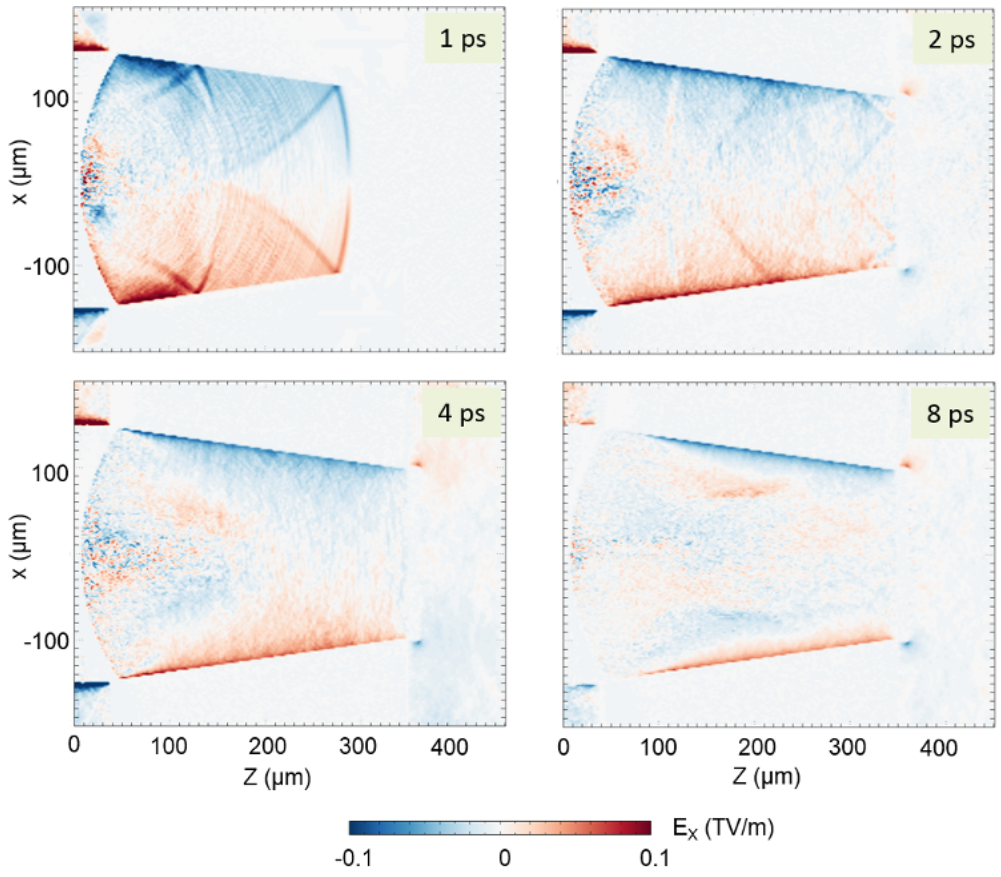

Figure 4.17: Snapshots of transverse electric field, E_x, in different time

beam expands, these (E_x) also get weaker.

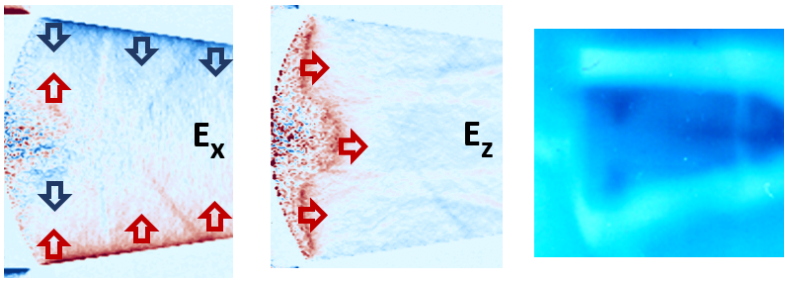

Figure 4.18: Electric fields in both directions (x and z) at 2ps compared with the proton radiography result. Drawn arrows estimate deflection directions of probe protons corresponding to fields direction

The electric fields seen from the simulation explains the proton radiography results of the experiment. For instance, the electric fields obtained at 2ps in the simulation, shown in Fig.4.18, correspond to the radiography image representing very early time. While continuous fields (E_x) point toward the symmetry plane of the wedge, the strong sheath field (E_z) of 'bell' shape points the rear foil. Therefore, probe protons moving across the wedge target are deflected by those electric fields. In other words, the dark horizontal band on the RCF image is due to focusing fields from the wedge and is disconnected near the hemi target because of the sheath field (E_z) pushing protons inward.

To summarize, our experiments demonstrate focused proton beam profiles as the measured Cu K_α signal clearly shows focused emission ($\sim 100\mu m$ FWHM) with high yield (8x higher peak) for the cone-assembled target. This focusability of a proton beam with a high energy (1 kJ) and long pulse duration (10 ps) laser is first demonstrated by this work. Features observed from proton radiography and simulation modeling explain the evolution of fields, including the transverse focusing field on a structured target. These results tell us that the long pulse duration of the laser is beneficial for collimating a proton beam, as electric fields formed by hot electrons are maintained for a long time contributing to focusing of the proton beam.

4.2 Improvement of Laser-to-Proton Conversion Efficiency in Isolated Targets

Acceleration of a high number of protons, as well as the beam focusing we discussed previously, are important for producing an intense proton beam. In a laser-driven proton beam, the total beam energy is limited by a given laser energy, but the laser-to-proton conversion efficiency can be improved. For the TNSA mechanism, significant work has been done to increase the conversion efficiency [73] [74]. Analogous to previous works, we experimentally studied the relation between the target geometry and conversion efficiency of laser-to-proton. The difference between this work and previous publications is the target design. The target in our work is the laser cut 2D target without dielectric stalks. This design can be beneficial for mass production, allowing a high repetition rate for proton generation. The main Cu target that interacts with a laser is supported by thin legs, and different widths of legs were used to compare proton production. The main hypothesis in this experimental design is to keep hot electrons at the main target by using an isolated target (with narrow legs) to generate strong sheath field in TNSA mechanism. Details of the target geometry is shown in Fig.4.19. The main target (150 μm square, 10 μm thick) is attached to a 10 μm thick surrounding Cu foil by using of 4 legs which have different widths (21, 42, and 84 μm) and 106 μm length.

The experiments were performed using the T-cubed laser at the University of Michigan. The laser is a CPA hybrid Ti:sapphire/Nd:phosphate glass having a wavelength of 1053 nm. The energy up to 4J was delivered on the target in a 400 fs (FWHM) with the laser focal spot of 20 μm, giving an average intensity of $3 \times 10^{18} W/cm^2$. Fig.4.20 shows the inside of T-cubed laser chamber with the laser path. The targets were placed with an angle of 22.5^o to the incident laser beam. For measuring protons produced from the isolated target, stacks of Radio-chromic film (RCF) of HD-810 were used. The RCF stack was placed 4 cm from the target rear with a target normal angle as shown in Figure4.20 and 12.5 μm thick Al foil filtered low energy protons ($< 1 MeV$) and other rays. As a main diagnostic in this

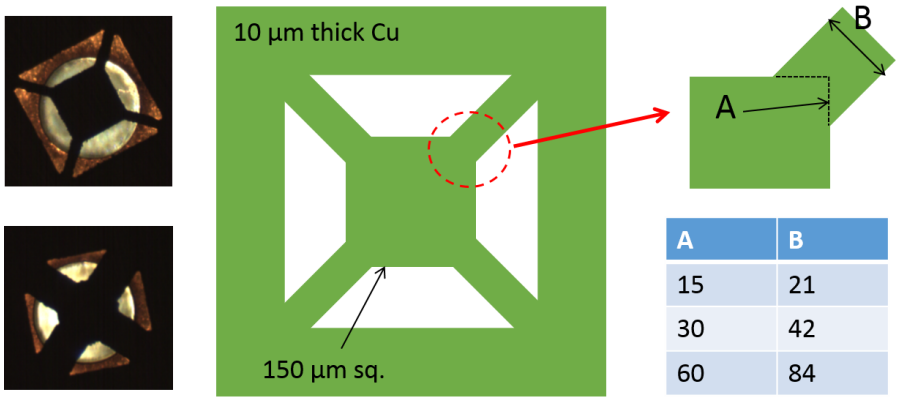

A	B
15	21
30	42
60	84

Figure 4.19: Target information. Images of targets used in the experiment are shown (left). Schematic of the isolated target with geometric parameters in scale μm (right).

experiment, a brief review of RCF and its application will be described in following sub-chapter.

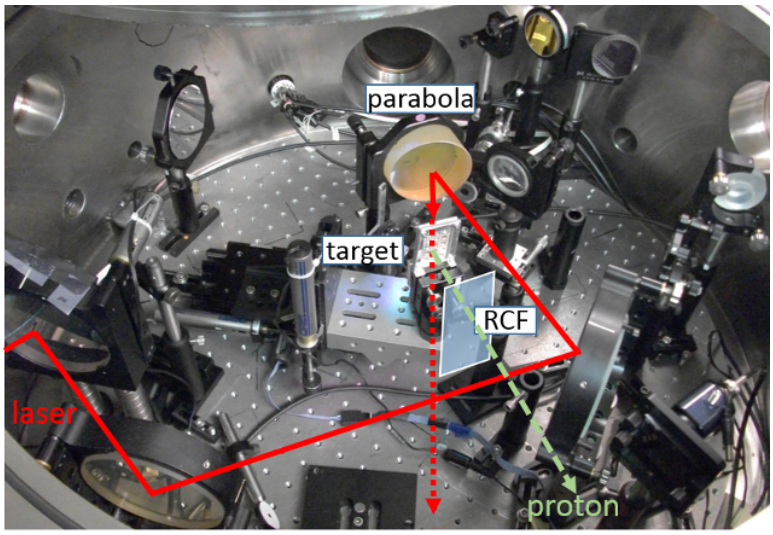

Figure 4.20: T-cubed laser chamber with a schematic of the experimental set up, showing a laser path and proton direction.

4.2.1 Radiochromic Film (RCF)

Radiochromic film (RCF) is a dosimetry film broadly used to measure ionizing radiation. For the experiments in this dissertation, RCF films were used as

a major diagnostic to analyze characteristics of the protons, including proton energy distribution and total proton numbers. RCF film consists of an active layer (radiation-sensitive organic monomer) and polyester layers. When the active layer is exposed to radiation, the color of the layer changes to a blue via a chemical reaction, and the darkness of the layer is proportional to the absorbed dose. The types of RCF we used are GAFCHROMICHD-810, HD-V2, and EBT3. The detailed compositions or these films are shown in Fig.4.21.

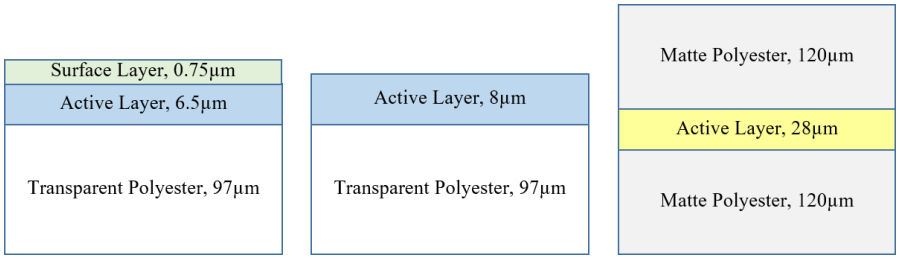

Figure 4.21: Composition of Radiochromic film. (from left) HD-810, HD-V2 and EBT3

In order to obtain a quantitative relation between the color values of the RCF and the dose of radiation, the calibration of the film with a known exposure dosage was required. Particles accelerated from a Cyclotron are generally used for a calibration because a Cyclotron provides particles with accurate energy control. Herein, we will go through the calibration of HD-810 described in [75] as this calibration was applied to our experiment. Various proton fluxes with an energy of 63.5 MeV produced from the Cyclotron were exposed on the RCF. Since the number of protons are given, the total dose deposited in a RCF layer can be calculated as, $Dose = E_{abs} \times (\frac{Proton/cm^2}{\rho\tau})$ where E_{abs}, is the deposited energy from a proton in the active layer. ρ and τ are the density and thickness of the active layer in RCF, respectively. The deposited energy from a proton is obtained from the stopping power calculations. For the calibration of digitized signal on RCF to the dose, an Epson Expression 10000XL scanner was used. After 48 hours from the exposure, the incubation time for stabilization of the chemical reaction, the film was scanned. Pixel values read from the scanner and calibrated dose values are shown in Fig.4.22.

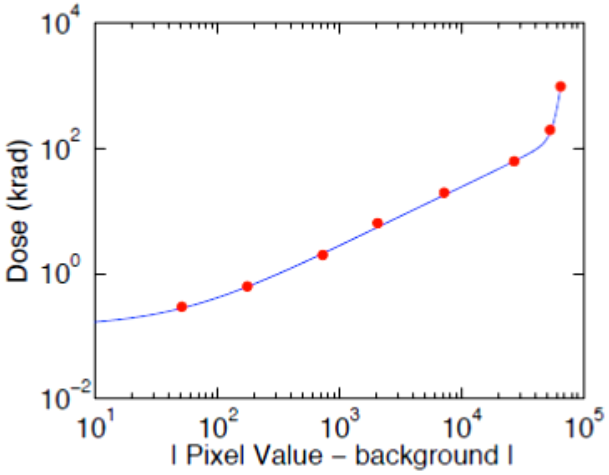

Figure 4.22: Calibration curve for converting the digitized value on HD-810 into a dose with a unit of krad. The calibrated dose values and its fit line are shown in red dots and the solid line. (from [75])

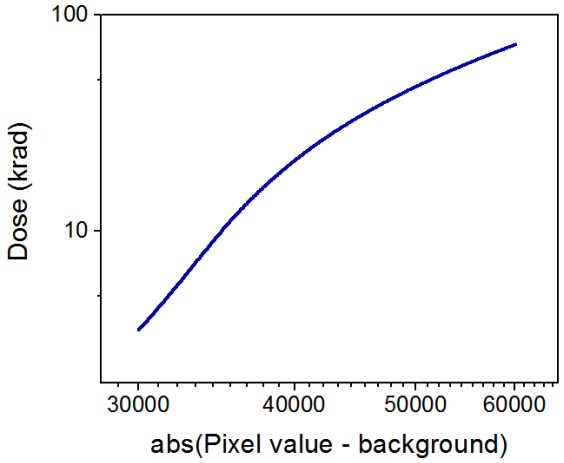

Figure 4.23: Calibration curve for the EBT3 film. Tandem accelerator in Dresden was used for the calibration. [76]

Compared to HD-810, the calibration curve for EBT3 radiochromic film, we used for other experiments in this dissertation, is shown in Fig.4.23 where the EBT3 is very sensitive to absorbed dose. Each proton particle deposits the most of its energy at the end of its propagation as called a Bragg peak. This characteristic of energy deposition can be useful for constructing a proton energy spectrum in a RCF stack since each film represents specific proton energy associated with proton stopping range. Metal foils are generally used with RCFs to build large energy steps in a spectrum and it plays a role of protecting other radiation as being placed in front of the RCF stack. An energy absorption curves based on SRIM stopping power [77] for HD-V2 films in a RCF stack is shown in Fig.4.24 as an example showing how each film represents the specific energy range of protons.

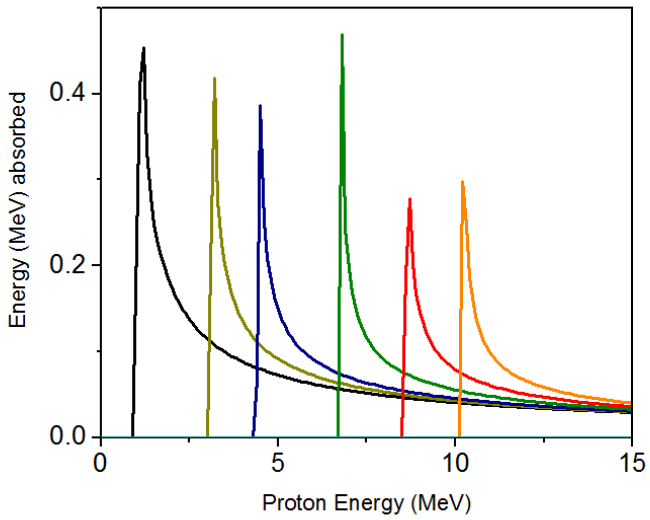

Figure 4.24: Energy absorption curves for HD-V2 films in a RCF stack. The each peak point of curve indicates energy representation of the film.

4.2.2 Results

The RCF data obtained from the experiment are presented in Fig.4.25 where RCF date from two different shots with similar laser energy using different targets ($21\mu m$ width legs and $84\mu m$ width legs) are shown in (a) and (b). The

energy ranges of the first and second layer of RCF correspond to 1 MeV and 3.1 MeV. The holes on RCF film are the path for small fraction of protons passing through RCF to reach Thomson Parabola diagnostic. As shown in the figure, strong proton signal is visible in the case of narrow leg ($21\mu m$ width) target showing a dependence of protons on the target leg size. In both cases, the proton signals on the second RCF layer are much weaker than the first layer indicating that reduced proton number with increase in proton energy.

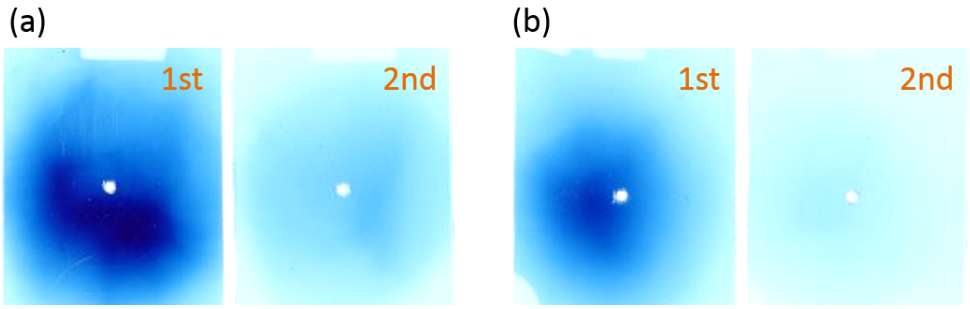

Figure 4.25: RCF data taken from the experiment using targets with narrow leg ($21\mu m$) and wide leg ($84\mu m$) are shown in (a) and (b), respectively. For each case, the 1st (left) and the 2nd (right) RCF are presented.

The detailed analysis of RCF and comparisons to simulation modeling were carried out by Morace and Bellei [78]. The digitized RCF data with a calibrated scanner was converted to the total dose in krads through calibration curves [79] and measured doses were normalized to the laser energy (red bars in Fig.4.26) to take into account the shot-to-shot variations. LSP simulation modeling of the experiment was performed for further interpret the protons, depending on an isolated target. The simulations were conducted in the 3D cylindrical coordinate with the maximum grid size of 0.25 μm. The target in the simulation is similar to the one used in the experiment: a $10\mu m$ thick Cu foil having different leg sizes was set with the initial temperature $T_i = T_e = 5eV$. Fully ionized hydrogen species as a contaminant layer were added to both the front and the back sides of the target. The thickness of the hydrogen layer was $2\mu m$, which is substantially larger than the real contaminant layer, and was used to provide enough particle statistics. To benchmark fast electrons produced via a laser, an electron source was injected into

the target with a slope temperature of 1.1 MeV and 400fs source duration. The total electron source energy was 1.46 J with an assumption of laser-to-electron conversion efficiency of 30%, with a spatial distribution of a Gaussian with $10\mu m$ (FWHM).

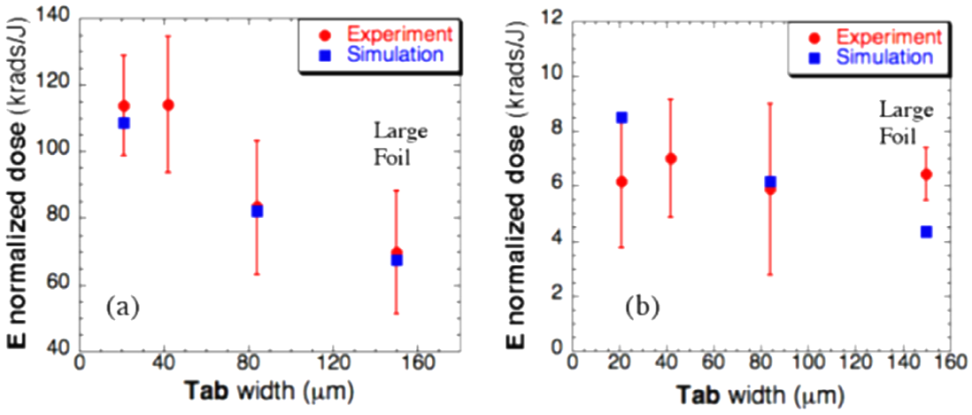

Figure 4.26: Integrated dose on RCF from the experiment (red) and simulation results (blue) showing a dependency of protons on the target leg size. (Plots from [78]

The simulation results quantitatively compared with the experiment are shown in Fig4.26. Both results are in good agreement, showing the dose enhanced with a smaller leg target. Also, a significant reduction of dose in the second layer is shown in both cases. However, the high experimental uncertainty (large error bars) inhibits a perfect comparison of trends. These results demonstrate the possibility of enhancing laser-to-proton conversion efficiency and allowing the proton beam to be more intense with a given laser energy.

Chapter 5

Computational study of Proton Beam Transport in Solid Density Matter

5.1 Dynamic Stopping of Proton Beams Depending on Beam and Target Conditions

In this chapter, using the LSP simulations with the new ion stopping calculation module we implemented, we systematically discuss the dependencies of proton beam transport in solid density matter on beam properties and target conditions. For simplicity, we first assume a beam having a monoenergetic spectrum. Simulations are conducted in two-dimensional (2D) Cartesian (XZ) coordinates with the grid size of 0.25 μm and the time step of 0.4 fs. The protons are treated kinetically, injected into the simulation box (size of 550 μm x 140 μm). The beam has an initial average energy of 5 MeV, a pulse duration of 3 ps with a flattop temporal profile and Gaussian spatial profile of 28 μm (FWHM). The solid density matter is setup with two fluid species of the background ions and electrons. With this hybrid setup, the overall energy and momentum are well conserved, and the prepared EOS table using Prisms PROPACEOS code can be used for dynamic update of target conditions during the beam transport. Since the target is heated

up very quickly by the intense proton beam or fast electrons which generally produced with protons via laser irradiation, the initial target temperature is chosen to be 10eV. The proton transport from different initial temperatures were also studies which will be discussed later. Note that here we include a population of electrons co-propagating with the proton beam which are presumably generated during the laser acceleration stage and cooled down to have the same moving velocity as protons. So, corresponding to MeV protons (project range of 10s of μm), the co-moving electrons have the energy of only several keV, which stop at a distance less than 1 μm in solid-density target. In the simulation, by injecting both protons and electrons we checked that the effect of these co-moving electrons only plays a role at the very early stage, different from those in low-density plasmas, after this confirmation, only protons are injected for all simulations.

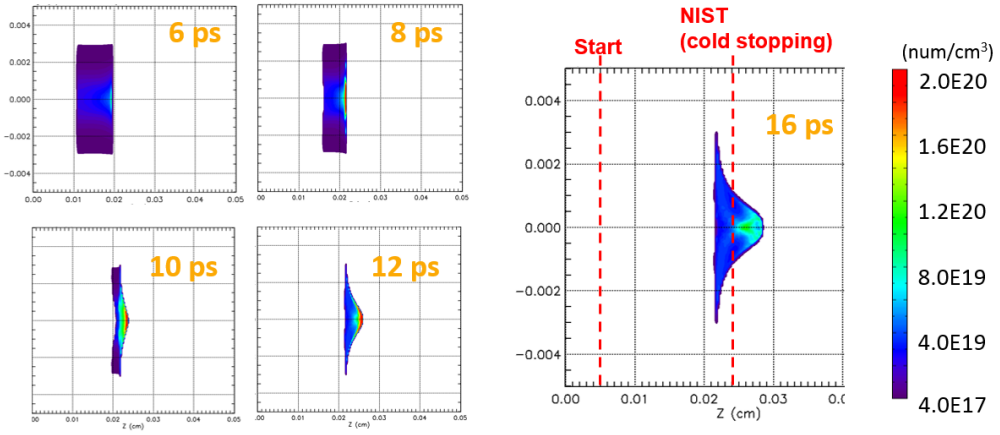

Figure 5.1: The density maps of a proton beam in Al solid target with different time. At 16 ps, proton beam is completely stopped showing final propagation distance which is longer than cold stopping range (NIST [63]).

Fig. 5.1 shows snap images of proton beam density in different time. Earlier time (6ps), protons continuously injected during 3ps propagate in the Al target showing quite uniform density in longitudinal direction (Gaussian profile in a transverse direction). As protons go deeply into the target, protons in the beam head part start slowing down first leading longitudinally compressed shape. Later time the beam finally shows the 'bell' shape where the beam is compressed in transverse direction as well. We will discuss what effects make variable beam shape via sys-

tematic studies with simulations in different conditions. When protons completely stop (at 16ps), the maximum projected distance is about 40 um deeper than the cold stopping range from NIST due to changing stopping power during the beam transport.

5.1.1 Beam Density

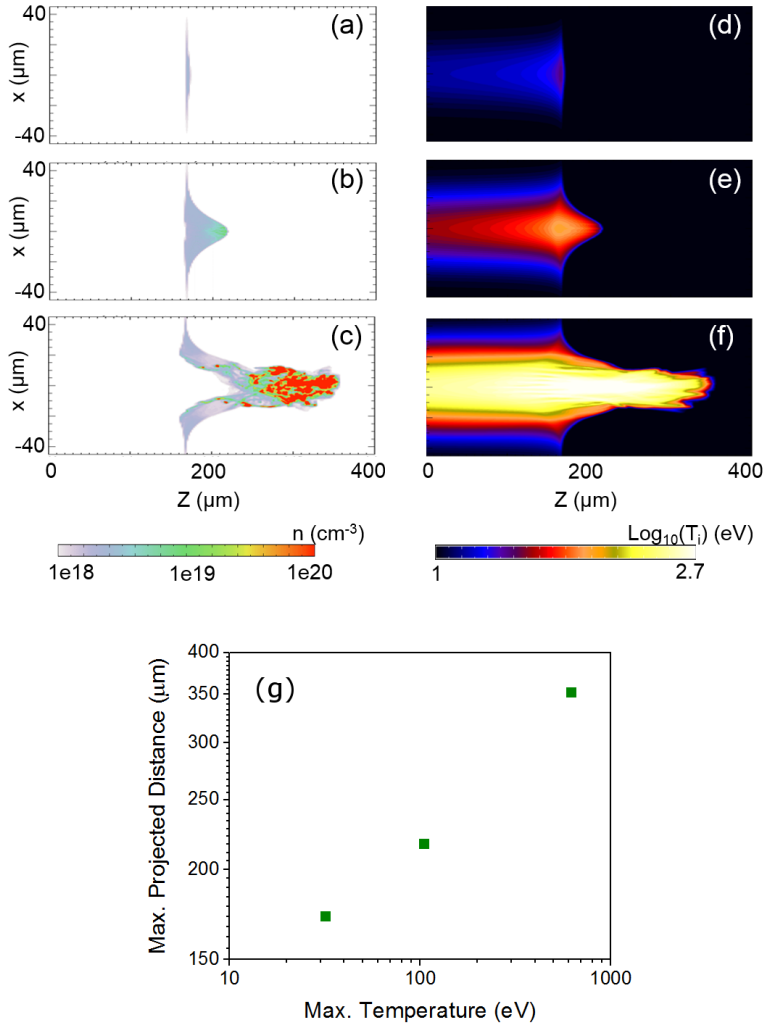

Figure 5.2: Simulation results of proton transport in Al target. Proton density (a-c) and Al target temperature (d-f) at 17 ps of proton beam transport. The proton beam current densities are respectively of 10^9(top), 10^{10} (middle), and $10^{11} A/cm^2$ (bottom). Maximum proton projected range vs maximum heated target temperature for different current densities are plotted in (g)

As we discussed above, it is obvious that the high number of protons in an intense beam can deposit enough energy to heat a target significantly enough to affect the proton stopping power. Here, we compare the beam dynamics including projected range and shape and its energy deposition in the target with different range of beam density. Fig. 5.2 plots the proton beam density and target temperature distributions at 17 ps after a proton beam with monoenergetic energy of 5MeV is injected in Al target, where the beam current densities are respectively (a, d) $10^9 A/cm^2$, (b, e) $10^{10} A/cm^2$, and (c, f) $10^{11} A/cm^2$, and the total currents are respectively about 6, 60, and 600 kA. The initial charge state of the Al is close to 3+ with initial target temperature of 10 eV as updated by the EOS. At 17 ps, this low density beam already lost all its energy and is completely stopped. For the low current density beam ($10^9 A/cm^2$), the target is weakly heated (< 30eV) during the beam transport, so the changes of the stopping power and the projected range are subtle resulting in quite uniform energy deposition and target heating. As shown in Fig. 5.2(a), the protons are stopped at nearly the same position after propagating 175 μm, which corresponds to the test result with single particles, and the peak of the heated region is also localized there, shown in Fig. 5.2(d). However, when the beam current density is increased to $10^{10} A/cm^2$, it is seen that the energy deposition starts to be nonlocalized following dynamical stopping power. Because the beam density in the central part is higher than in the wings due to its Gaussian spatial profile, protons in the central part heat the target more, some protons are able to propagate deeper in the target with reduced stopping power resulting in a bell shape, shown in Fig.5.2(b). For the case of $10^{11} A/cm^2$, the energy deposition is obviously nonuniform, non-localized, and also much deeper inside the solid target [Fig. 5.2(c)]. The reason is that when the target is strongly heated up to 100s of eV by the intense beam, the stopping power for protons changes dynamically. With this higher density beam, the heated region of the target is much broader, as shown in Fig. 5.2(f). Moreover, the most heated region is seen to be behind the beam front because the target is heated enough then the Bragg peak of stopping power is smoothed. This means the energy loss of denser proton beam is reduced after experiencing peak stopping power, then continues to propagate deeper with

slow velocity. Fig. 5.2(f) plots the distance of the farthest-penetrating proton versus the maximum target temperature for the three current density cases.

5.1.2 Beam Pulse Duration

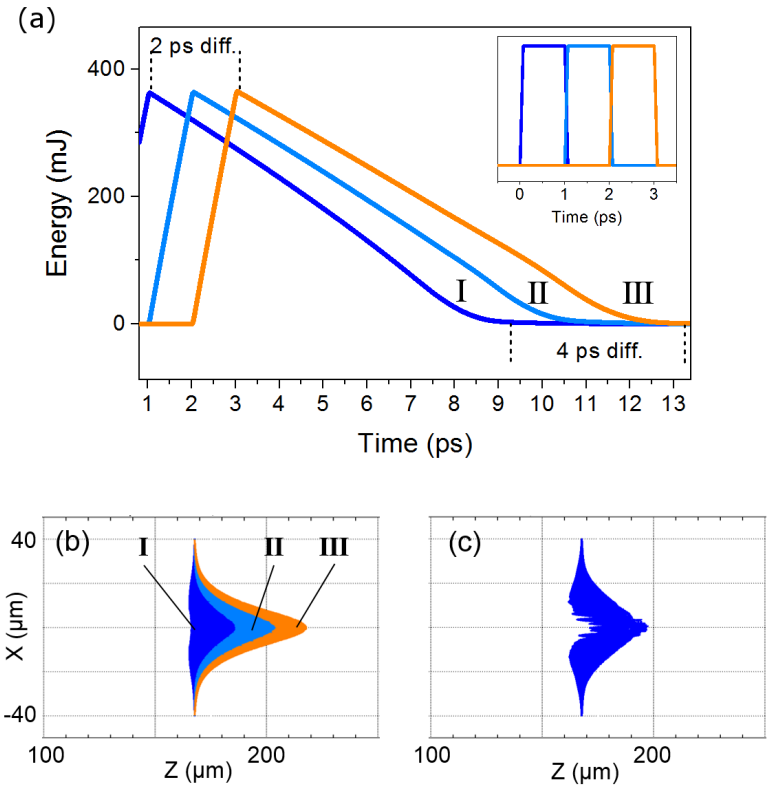

Figure 5.3: Variation of energy loss rate and projected range analyzed with proton beam temporal profile where the beam is broken into temporally-distinct 1 ps beam segments. (a) The instantaneous beam segment energy in the domain as a function of time for the 3 segments for a 3 ps proton beam pulse train shown in the inset (each portion has a current density of $10^{10} A/cm^2$). (b) The stopped position spatial extent of the segments of the same pulse train and (c) a 1 ps combined beam with a current density of $3 \times 10^{10} A/cm^2$ (c).

As we learned above, the proton energy loss rate is a function of temperature of the heated matter, decreasing with rising target temperature for low energy range. Therefore, the proton beam transport dynamics depend also on the beam pulse duration. Fig. 5.3 shows how and where the different time segments (every 1 ps) of the above beam pulse stop inside a solid Al target. Although the protons of

each segment [Inset of Fig. 5.3(a)] have the same beam energy and average particle energy of 5 MeV, the energy loss rate of each portion of the beam is different as shown in Fig. 5.3(a), where the earlier protons in the first 1 ps lose all energy at about 9 ps, however the later protons lose their energy over a longer time. For example, the protons in the last 1 ps (segment III) still have energy of about 50 mJ at t=11ps and they penetrate up to 40 μm deeper inside the target than the earlier protons in the first 1ps [portion I] as shown in Fig. 5.3(b). These differences of energy loss and projected range with pulse time are explained by stopping power as a function of energy with target temperatures. Proton stopping powers for higher energy than 1 MeV in different target temperature show relatively small differences, while the stopping power is dramatically reduced as target temperature increases for protons below 1 MeV. Since the maximum stopping peaks under 1 MeV range, protons, propagating in the target lose their energy gradually and when protons have less energy than 1 MeV, most of their energies are deposited into the target with target heating. Therefore, protons later in the pulse follow the path pre-heated by earlier protons and experience reduced stopping power, resulting in propagation deeper in the target region, with the biggest differences occurring in the heated region beyond the original Bragg peak, near the end of their propagation. If pulse duration of a beam is relatively short, there are less chances for protons to experience reduced stopping power in a pre-heated region. Fig. 5.3(c) shows the beam projected distance for a short pulse beam, 1 ps, with the current density of $3 \times 10^{10} A/cm^2$ which is three times higher than the current density of each segment of the beam in Fig. 5.3(b) to make total beam energy equivalent for both cases. As we see the 1 ps beam penetrated to shallower depth than the 3 ps beam, demonstrating that beam pulse duration is an important parameter along with beam density for the beam transport in terms of propagation distance and distribution of energy deposition. As we have seen the influences of both the beam density (from previous sub chapter) and beam pulse duration on the beam transport. The combination of these two effects is summarized with the beam stopping range (projected distance) and the maximum temperature in a target via beam heating as shown in Fig. 5.4. Three different proton beam densities

and 4 different pulse durations for each beam density are compared. The most visible trend is that proton beams with higher density and longer duration show longer stopping range and high heating. However, the dependence of the projected distance on beam duration is weak for the low density beam ($10^9 A/cm^2$), while high density beams clearly show the effect of the beam duration. For example, the stopping range of the beam with a density of $10^{11} A/cm^2$ and a duration 1ps is enhanced by a factor of 2 in the case of duration 4ps.

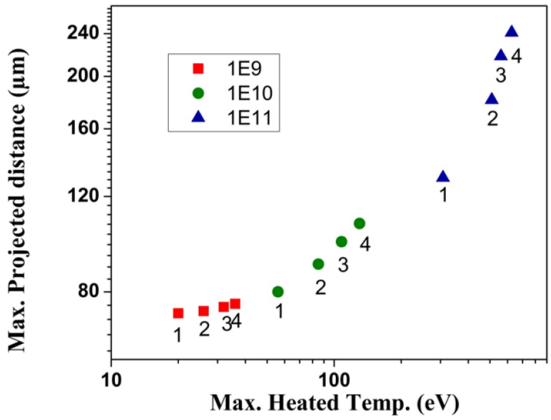

Figure 5.4: Comparison of maximum proton projected range and heated target temperature with different beam density and pulse duration. All cases, the kinetic energy of proton beams is 3 MeV. Each numbers indicate pulse duration with ps unit.

5.1.3 Target Material

Due to the different equation of state and ionization potentials for various materials, the proton beam transport and stopping dynamics in different solid materials changes significantly. Here, we compare protons in Al and Cu. First of all, the higher atomic number (Z= 29) of Cu initially causes higher stopping power than Al (Z= 13) due to greater contribution from bound electronic stopping. Then, as the targets' temperatures increase, the higher charge state of Cu than Al leads to higher free electronic stopping. Fig. 5.5 shows the proton beam energy losses as a function of the propagation distance inside the target for Al and Cu targets, where the proton beams have the same mono-energetic energy of 5 MeV and pulse

duration of 3ps in our simulations. We can see that the proton beam energy in Cu drops much more quickly [Fig. 5.5(a)] and it is stopped within a shorter distance, which is within our expectation because the stopping power in Cu is higher than in Al. Corresponding to these energy losses, protons are accumulated near the distance, in which protons completely lose their energy and stop, showing higher proton density in Cu at the beam front ($\sim 80\mu$m) comparing to the density in Al [Fig. 5.5(b)]. From the lineout of target temperature, deposited energy profiles of the beam in different materials are inferred; with higher stopping power, Cu target is heated to 60 eV at beam starting point on z-axis and has higher temperature peak ($\sim$110 eV at 80 μm where the most protons stop) as shown in Fig. 5.5(c). Note that the difference in integrals of these two plots is due to different heat capacity of the materials; with lower heat capacity, Al target is more easily heated up by the proton beam. This explains that different materials are likely to have different responses to intense proton beams.

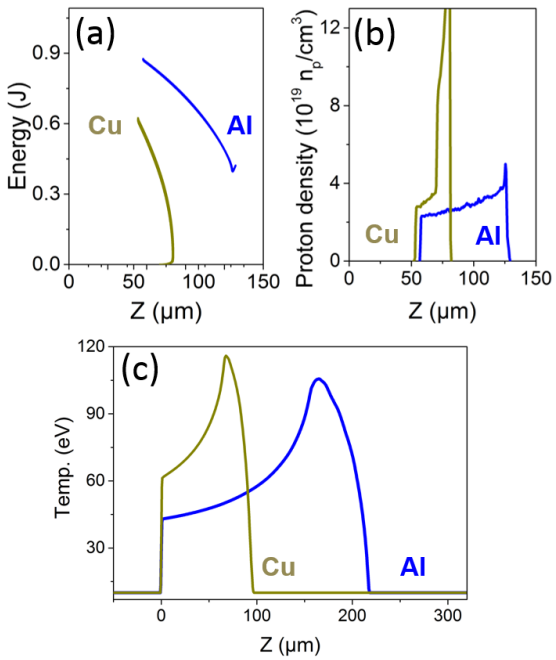

Figure 5.5: (a) and (b): the evolution of proton beam energy and density as a function of propagation distance in Al and Cu at t= 5 ps. (c) The lineout of the temperature profile of Al and Cu in longitudinal direction at t= 14 ps.

5.2 Charge and Current Neutralization in Proton Beam Transport

We clearly see that the proton beam undergoes changes in the beam shape, projected distance and energy deposition during its transport in solid targets, in particular, forming a bell-shaped profile with apparent beam narrowing. These changes are partially explained with dynamic stopping power but another important factor to contribute to change is the collective effects in intense beam-plasma interaction. For instance, as beam density increases, the heated target develops a strong magnetic field leading to beam focusing which also heats the target more. Before we discuss details of magnetic field induced in solid targets by the beam, it is necessary to understand more about the neutralization of the charge and current of beams in the solid targets. If a pure ion beam is propagating in a vacuum, it must be a space-charge dominant beam producing strong electric fields. Similarly, ion beams moving in a medium have the space-charge inhibiting the beam transport unless charge is neutralized. Many studies have done regarding the charge neutralization of ion beam in a plasma and solid density matter [68] [80] [81], and concluded that the beam charge can be easily neutralized with a condition of high (electron) density background as electrons shift in positions compensating a charge. One more important factor for charge neutralization is the beam pulse duration associated with electrons response time. Electrons response to an external charge perturbation on a time scale of ω_{pe}^{-1} meaning that if the pulse duration of the ion beam is longer than this time scale, electrons cancel out a positive charge [68]. The ion beam pulses studied in this dissertation have the time duration more than picosecond and this is much longer than the electron response time (femtosecond scale for solid Al), $\tau_b >> 2\pi/\omega_{pe}$. For the current neutralization, the ratio of ion beam density to background density is important. It needs to be pointed out that even though the range of beam density in this study is very high (extreme case is about $10^{21} protons/cm^3$), this beam density is still much lower than the electron density ($> 10^{23}/cm^3$) of the solid targets, and the heated solid target is a good conductor as a partially ionized warm dense or a plasma state providing enough

electrons (return current) to allow propagation of the proton beam. Thus, the current of the proton beam can be easily neutralized in a solid target. This current neutralization associated with densities of beam and background is scaled as [81]

$$\frac{I_{net}}{I_b} = \big[\frac{I_A}{I_b}(1-\chi^2)\big]^{1/2} B \tag{5.1}$$

where, I_A is the Alfven current, $I_A = 17\beta_b\gamma_b kA$, B is the geometric factor and $\chi^2 = 1/(1 + n_b/n_p)$. If the density of background plasma is much higher than the beam density, the ratio of beam-to-plasma density (n_b/n_p) decrease, the net current fraction falls close to 0 meaning that the beam current is completely neutralized. Another factor to be considered for the current neutralization is the beam radius (size in transverse direction) as discussed in [80]. If the beam radius is smaller than the skin depth c/ω_{pe} where electric field can reach by, the electron return current cover larger area than the beam size causing incomplete current neutralization. The scale $r_b > c/\omega_{pe}$ can be expressed as

$$I_b > \frac{1}{4\gamma_b} I_A(\frac{n_b}{n_p}) = 4.25(\frac{\beta_b n_b}{n_p})kA, \tag{5.2}$$

Where $\beta_b = v_b/c$ and γ_b are respectively the beam normalized velocity and relativistic factor. All the cases studied here, the beam current (> 10 kA) is higher than the neutralization limit. Therefore, the return current (neutralizing current) in the background target plasma is induced to sustain the beam propagation. Due to the higher charge to mass ratio, electrons generally respond faster than ions, so the target background electrons move in the same direction as the proton beam propagation direction. This return current effect is seen in LSP simulations of proton beam transport. Background electrons following a proton beam are shown as a negative electron current in Fig. 5.6(a) where proton beam with a density of $10^{10} A/cm^2$ is injected to Al target in LSP simulation and currents for each species are line outed along the longitudinal axis. The interesting feature shown for the long pulse duration beam (2ps) in Fig.5.6(b) is background Al ion current moving in opposite direction to the proton beam at the beam tail part. This is because the beam pulse duration is longer than background ion response time, $\tau_b < 2\pi/\omega_{pi}$ [68]. In the region where background ion moves, both background electrons and ions

enable the beam current neutralization.

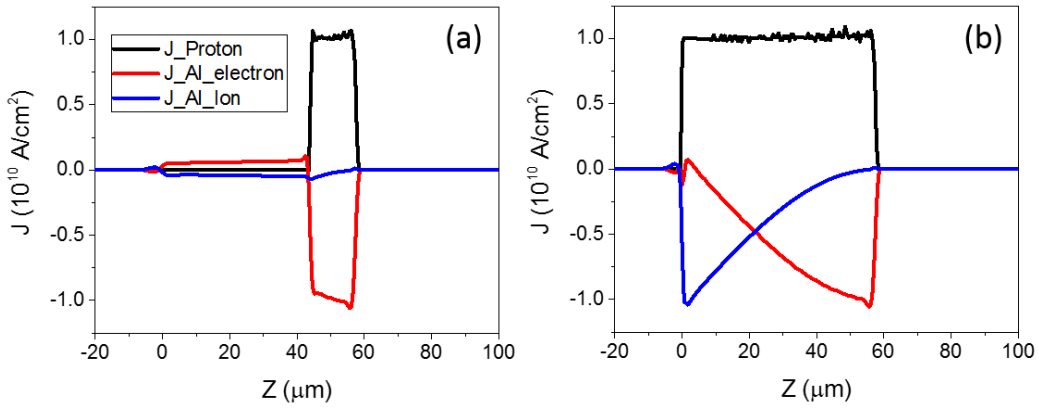

Figure 5.6: Lineouts of current density of proton, background electron and background ion taken from center of proton beam that has an initial current density of $10^{10} A/cm^2$. Current densities are measured at 500 fs (a) and 2 ps (b).

As shown in the results above, neutralization of the proton beam current is seen in simulations where the background Al plasma (both ion and electron) is set as a fluid and injected protons are treated as kinetic. To double check this current neutralization, results from a full kinetic simulation (all species are treated as kinetic) are shown here. Similar to previous fluid simulations, the injected proton beam has a current density $10^{10} A/cm^2$, but the density of the background Al plasma here is $10^{21}/cm^3$ (one order lower than solid density). In a kinetic setup, extremely high number of macro-particles are required to represent a solid density state for good energy conservation without artificial (numerical) effects. Thus, using a less density background is a way to avoid computationally expensive simulations, and it is still an acceptable condition for checking return current driven by the proton beam. Fig. 5.7(a) shows a net current density map ($J_{net} = J_{proton} + J_{background\ ion} + J_{background\ electron}$) at 30 fs. Since the proton beam current is canceled out by the electron return current, the net current (particularly central part) approaches zero. At wing sides (near edges of the proton beam in a transverse direction), weak currents (positive and negative layers) are seen, indicating that the proton beam current is not perfectly neutralized. This result corresponds to the background electron current shown in Fig.5.7(b) where electron current near

the proton beam edge (x$\sim 1\mu m$) is lower than the one at the central region. This is because fields driven by the proton beam spread into the background plasma over distance of approximately skin depth ($c/\omega_{pe} \sim 100nm$ for given plasma condition), causing a smaller and increasingly spread out electron return current at near the proton beam edge. However, most areas inside the proton beam clearly show current neutralization, the same current for background electron and proton, as shown in the lineout of current density in Fig.5.8. Consequently, both fluid and kinetic simulations represent current neutralization of proton beam by background electrons, showing good agreement with the theory.

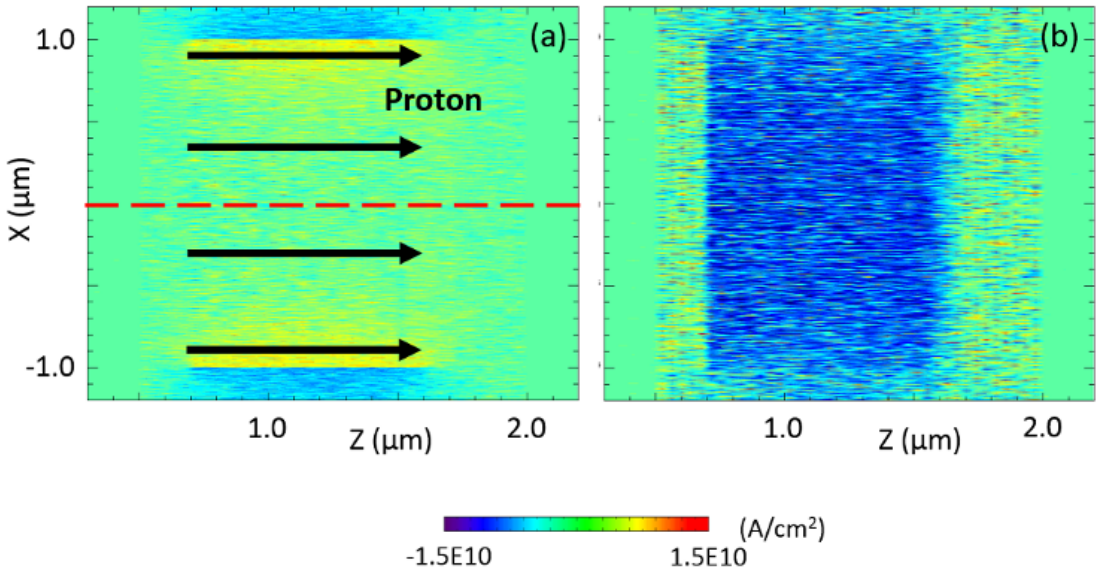

Figure 5.7: Current map at 30 fs from a full kinetic simulation where a proton beam of density $\sim 10^{19}/cm^3$ propagates into Al plasma of density $\sim 10^{21}/cm^3$. (a) Net current density map. $J_{net} = J_{proton} + J_{background\ ion} + J_{background\ electron}$ (b) Background electron current density map.

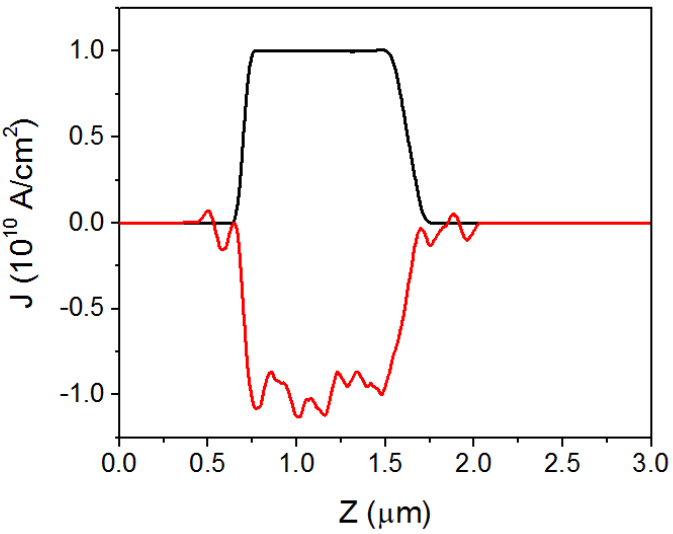

Figure 5.8: Lineouts of current density of proton beam and background electron taken from the center of proton beam ($X = 0$) in Fig.5.7 (dotted line). Proton and electron currents are presented in black and red lines respectively.

5.3 Beam Collective Effects

5.3.1 Self induced Magnetic Field

We have seen how easily proton beams are neutralized by return current (neutralizing electrons). With this condition of weak internal field of a beam, understanding the possible mechanisms for collective effects including magnetic field in the beam transport is crucial and will be an interesting topic for the intense beam dynamics.

Fig. 5.9 shows how inclusion of the dynamic stopping and the magnetic field affect transport and heating. For the fixed stopping case (a, e) stopping power calculations in the simulation are made assuming 10 eV temperature, regardless of the updating target temperature. A dynamic stopping case (b, f) uses updating stopping power with target temperature as implemented with the module. Neither of these cases experience electric and magnetic fields as the fields were deliberately switched off in the simulations, but for the case including fields and dynamic stopping (c, g), influences by the induced fields are apparent during transport.

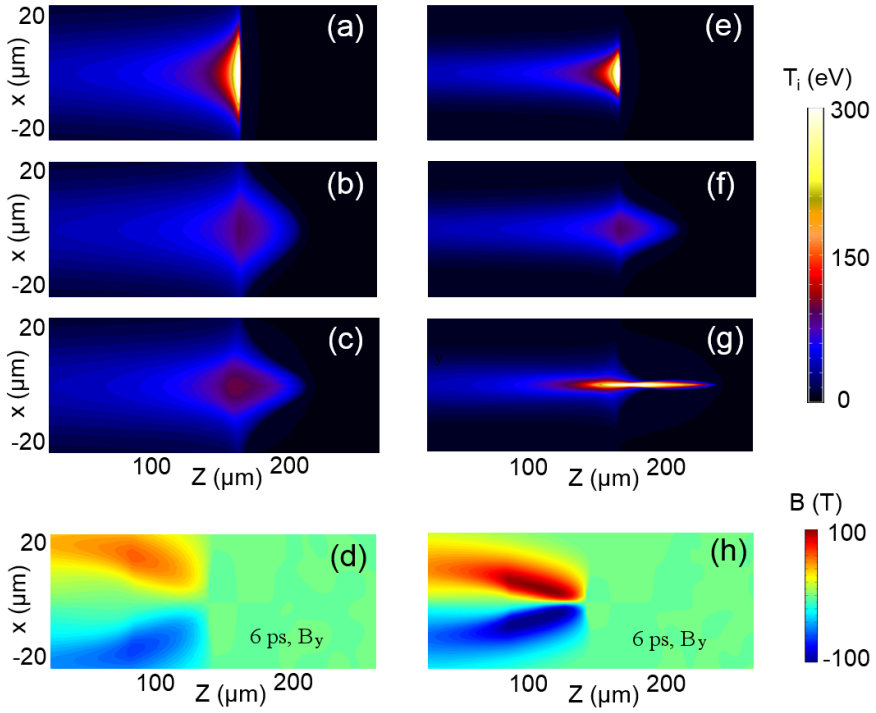

Figure 5.9: Heated Al target temperature maps are plotted at 17 ps when the proton beams are stopped. Top (a and e): No field and fixed stopping power. Middle (b and f): No field and dynamic stopping power. Bottom (c and g): With field and dynamic stopping power. (d and h) magnetic field map at 6 ps. The beam average energy for all cases is 5 MeV. Injected beam diameters (FWHM) are 28 μm for (a-d) and 14 μm for (e-h).

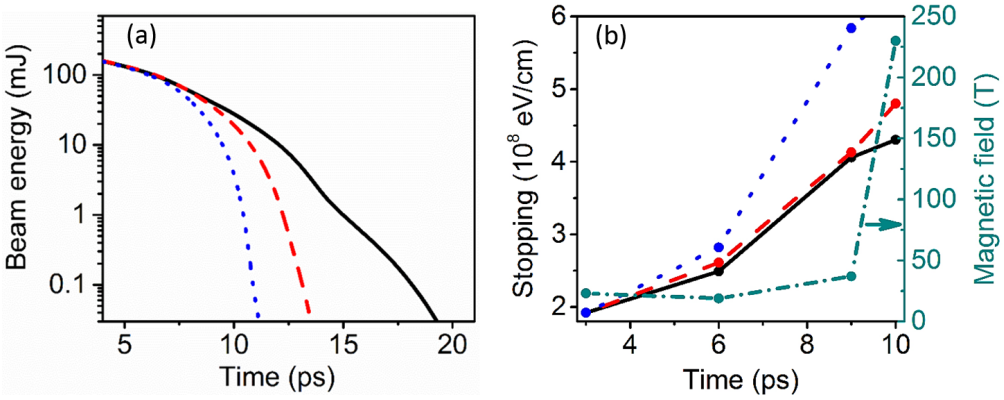

Figure 5.10: (a) is the temporal evolutions of the total beam energy depositions, where dotted, dashed and solid lines are for the cases (e), (f) and (g) in Fig. 5.9, respectively. (b) is the corresponding evolution of measured stopping power on axis and the evolution of self-generated magnetic field at $r = r_0/4$ in (g) in Fig. 5.9.

In all cases, monoenergetic proton beams with current density of $10^{10} A/cm^2$ are injected for 3 ps in Al target. For comparison, only one parameter is changed for the cases; beam average energy for all cases is 5 MeV and beam diameter (FWHM) is 28 μm (a-d) or 14 μm (e-h). Beams with fixed stopping power show similar heating profile such as a sharp peak at the end of beam propagation and maximum temperature of around 350 eV. This is because all of the beams have the same current density, the beams have the same amount of energies in identical dimensions. These results are similar to Monte Carlo simulations but once stopping power is varied with target temperature, the beams experience dynamic stopping and spread out resulting in smoothed peak values as shown in (b) and (f). For these results, without field in simulation, no significant differences are seen in the cases of different beam parameters. However, field-on simulations clearly show collective effects, i.e., beam focusing and highly heated temperature profiles are triggered by the induced magnetic field. The beam with smaller diameter, 14 μm, (g) experiences self-focusing by the induced strong magnetic field (h), which exponentially grows in time as the beam is collimated to the axis (higher current density). This beam focusing results in highly heated temperature of above 300 eV which is three times higher than the maximum temperature heated by the larger diameter, 28 μm, beam (c). An interesting result is that although the total beam energy of the wider beam is higher than the energy of the narrow beam by factor of 4, the maximum heated temperature for narrow beam is much higher than wider beam case. This result indicates strong influence of the beam diameter on beam focusing and localized target heating rather than total beam energy. Fig. 5.10 (a) plots the temporal evolution of the total beam energy deposition for the three cases (e, f and g) in Fig. 5.9, showing that by updating stopping power and collective beam-plasma interactions, the energy deposition rate of the beam is reduced and its deposition depth increases. This has two causes; (i) the stopping power drops relative to the cold stopping rate with a rising target temperature [compare the dotted (blue) and dashed (red) lines in Fig.5.10(a)] and (ii) the beam is focused by a self-generated magnetic field, leading to further increase of the target temperature and reduction of stopping power [compare the dashed (red) and solid (black) line

in Fig. 5.10(b)]. It should be noted that the additional dimension in 3D might bring some differences from 2D, in particular upon the impact of the self-generated magnetic fields.

As already discussed before, the charge and current of proton beams are neutralized by background electrons meaning that the net current in a target is zero. This arouses curiosity about the mechanism of generated magnetic field during proton beam transport. Note that protons in a target move fast, while the larger number of electrons move slowly resulting in $J_{net} \approx J_b + J_e \sim 0$, where these electrons experience the resistivity in a target. Therefore, we can estimate magnetic field generation during proton beam transport using the method of resistive magnetic field growth, which has been well studied for fast electron transport. The complex distributions of the background electron return currents eventually results in the strong azimuthal magnetic field By generation explained with combination of Faradays law and Ohms law $\partial B/\partial t = -\nabla \times (\eta J_{cold})$, where η is the target resistivity and J_{cold} is current density of target electrons. Assuming $J_{cold} \approx J$, in our simulation geometry, the azimuthal magnetic field generation becomes

$$-\frac{\partial B_y}{\partial t} = \eta(\frac{\partial J_z}{\partial x}) + (\frac{\partial \eta}{\partial x})J_z \tag{5.3}$$

For the estimation of magnetic field generated by proton beam, we will now employ the rigid beam model [82]. This model takes into account the ohmic heating for the target heating mechanism bringing the temperature scaling as $\partial T/\partial t = (\eta J^2)/C$, where a resistivity has the form as $\eta = \eta_0(T/T_0)^\alpha$. The magnetic field is derived from Eq. 5.3 to

$$B_y(x,t) = -\frac{dJ}{dx}\frac{ckn_eT_0}{J^2}\big(1 + \frac{1+\alpha}{1-\alpha}\frac{T}{T_0} - \frac{2}{1-\alpha}\frac{\eta}{\eta_0}\big) \tag{5.4}$$

where ckn_e is the heat capacity term, and subscript 0 indicates initial values. To apply this equation to our simulation case, the beam current density is assumed to be static with Gaussian radial profile, $J = -J_0 exp(-x^2/R^2)$ and α is set as -3/2 to obey the Spitzer resistivity because in LSP simulation, collision frequencies are calculated by the Spitzer model. Since the initial target temperature is set as 10 eV in the simulations and target temperature quickly increases with the beam transport, the Spitzer model is valid for these cases [83] [84]. Comparisons of

estimated magnetic field (calculated from Equation 5.4) to simulation results are shown in Fig. 5.11, where the simulation lineouts are taken at the beam tail parts at 3, 6 and 9 ps. At 3 ps (equals to the beam pulse duration) the magnetic fields in the simulation agree well with the calculation for both beams having different diameter of 28 μm and 56 μm. However, the magnetic field starts changing; once the beam is deflected toward the z-axis by the field focusing, its current density increases and the current density gradient increases resulting in additional magnetic field growth. Since the calculation does not include the changing current density caused by self focusing nor the protons drag heating (Ohmic heating is the only heating mechanism taken into account), it is not valid to apply this estimation for intense proton beam transport, especially at later times when the effects of beam pinching and target heating are not negligible

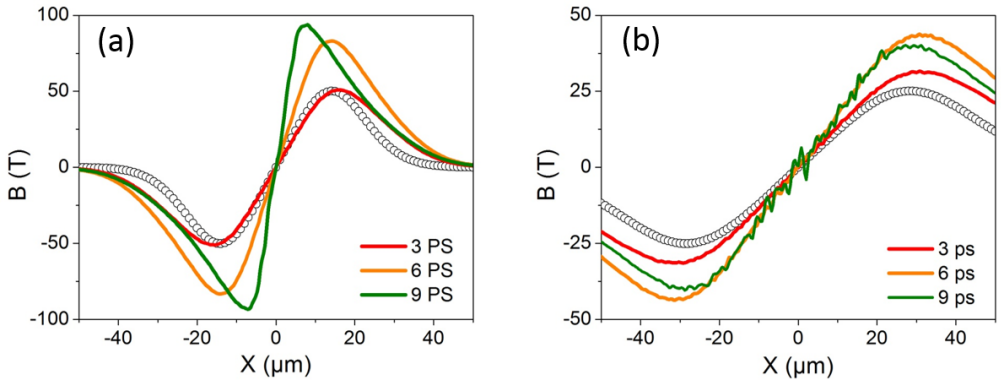

Figure 5.11: Profiles of magnetic fields from simulations and calculated estimation. The lineouts of magnetic field in transverse direction in simulation (solid lines) at different times, 3, 6, and 9 ps and with theoretical estimation (blank circle line) at 3 ps. (a) Beam diameter: 28 μm, Fig. 5.9 (e-g). (b) Beam diameter: 56 μm, Fig. 5.9 (a-c).

Interesting feature we could see for the narrow beam (28 μm diameter) is the magnetic field switching its polarity from focusing to defocusing when the proton beam is focused enough to generate sharp temperature gradient in transverse direction. In early time (proton beam is being focused), a sharp current gradient is shown while heated target temperature is quite uniform as shown in Fig. 5.12 (a). However, with tightly focused beam, high local heating causes a sharp temperature gradient, Fig. 5.12 (b) indicating that the second term of the equation 5.3 is

dominant resulting in switching of the direction of the azimuthal magnetic field. The current density profile showing uniform center region between two peaks also indicates that the beams further focusing is inhibited by the defocusing magnetic field and this phenomenon is described as the hollow of beam front in many studies of intense electron beam transport [85] [86] [87]. This field is shown in Fig. 5.12 (c); at the central region of the beam, the lineout of magnetic field in transverse direction shows the opposite directions comparing to outer side radially.

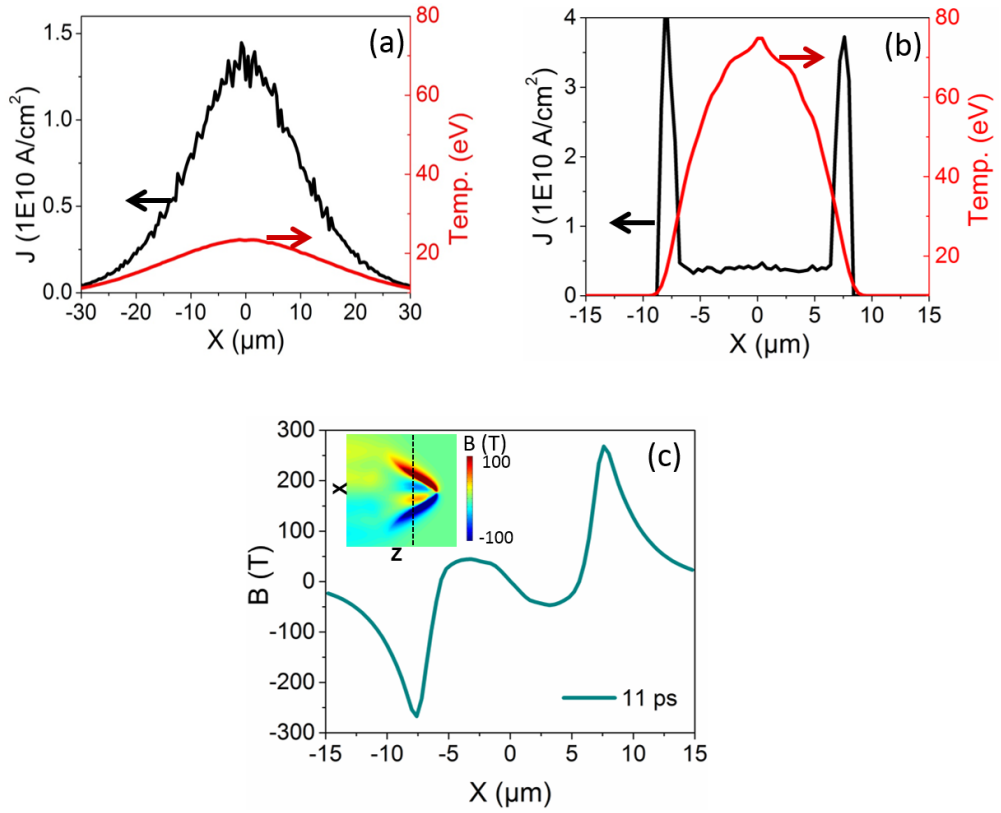

Figure 5.12: The lineouts of current density, temperature and magnetic field in transverse direction in simulation for the case of beam diameter: 28 μm, Fig.5.9 (e-g). Respectively (a), (b and c) are taken at time 6 ps and 11 ps

The evolution of magnetic fields driven by a proton beam of 8 MeV energy clearly shows the polarity change during the beam transport, 5.13. As the beam is focused, the opposite direction of magnetic field start growing from inside the beam where the target is locally heated and gradient of the resistivity becomes larger. However, the magnetic field outerside of pinched region keeps the same

field direction meaning that the current gradient contribute more than resistivity gradient to total magnetic field generation.

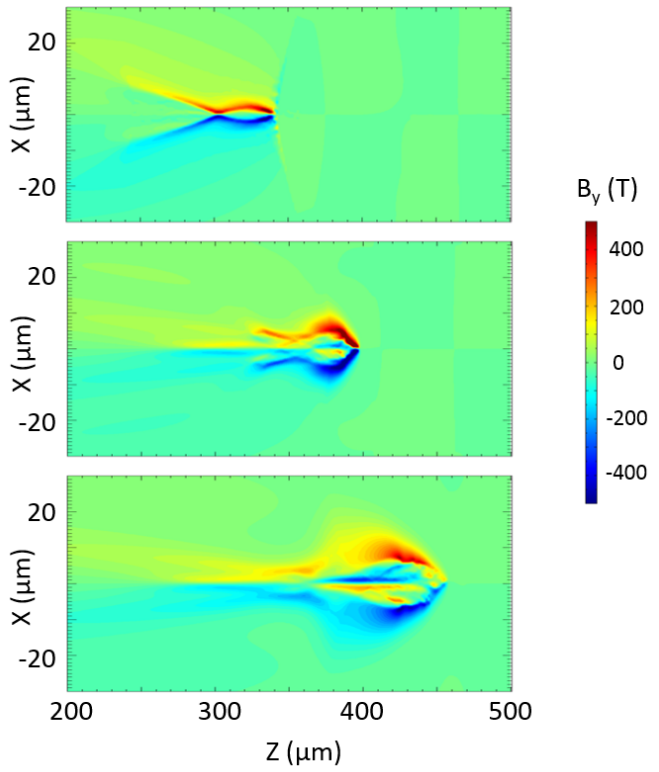

Figure 5.13: Magnetic field maps driven by the proton beam of 8 MeV kinetic energy with the beam diameter of 28 μm at 12ps, 15ps and 18ps.

5.3.2 Beam Pinching

5.3.3 Influence of the Proton Kinetic Energy

Another important factor for beam focusing is seen by comparing different beam average energies of 4, 6 and 8 MeV in Fig.5.14(a, b, and c), respectively, where beam diameter and current density are fixed for both cases. Although both beams start with the same initial current density, the higher average energy, 8 MeV, beam experiences lower stopping power than the 4 and 6 MeV beams, leading to a slower decrease in current density. This relatively sustained current density keeps inducing magnetic field growth, continuing the beam focusing. Furthermore, due

to its longer projected range, the 8 MeV beam has more chance to undergo self focusing in its path into the target. This effect is shown in Fig.5.14(c) where we see the 8 MeV beam is already pinched at 350 μm, heating the target to above 300 eV.

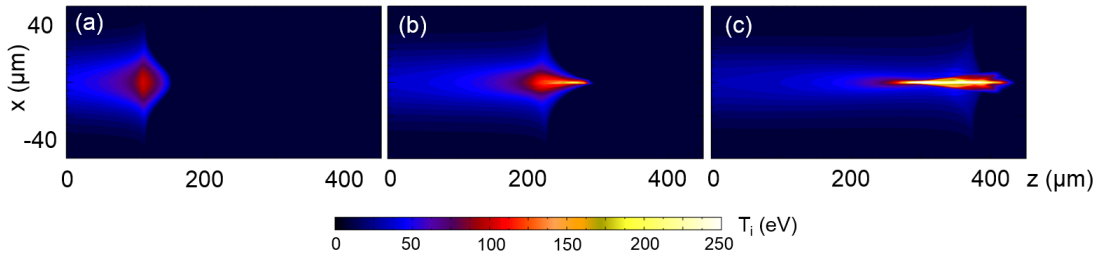

Figure 5.14: Heated Al target temperature maps are plotted at 17 ps when proton beam is stopped. Initial average energies of injected proton beams are respectively of 4 MeV (a), 6 MeV (b) and 8 MeV (c). Other beam parameters are identical for all cases.

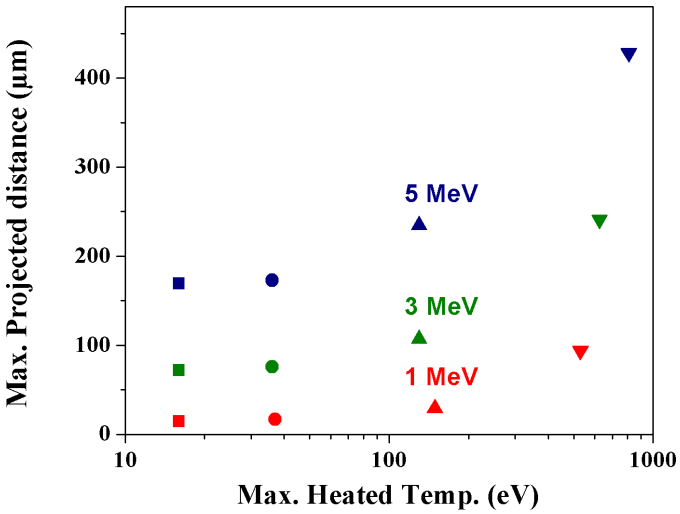

Figure 5.15: Maximum projected distance vs maximum heated temperature with different average proton energy (1, 3 and 5 MeV). The shape of dots indicate beam current density (A/cm^2); from left, 10^8(square), 10^9(circle), 10^{10}(up triangle) and 10^{11} (down triangle).

Influence of proton beam energies on the furthest projected distance and the maximum heated target temperature are compared with different beam densities in Fig.5.15. For all cases of beam energies, heating temperature is enhanced with the

beam density increase. For low initial beam densities ($10^8 A/cm^2$ and $10^9 A/cm^2$), beam propagation distances are similar to test particle results; projected ranges are nearly constant. However, as beam densities increase, projected ranges by initial energies have different slope showing the sharpest increasing slope for the 5MeV beam. From this combined effects of beam energy and density, it can be inferred that the projected distance of higher energy proton beam is sensitively changes once beam is dense enough ($> 10^{10} A/cm^2$).

5.3.4 Influence of the Target Temperature

We have learned that target resistivity is an important variable controlling current-driven magnetic field growth and further that the resistivity evolution can affect magnetic polarization in the targets. Thus it is also important to study proton beam transport in the targets of different initial temperatures to see how the beam is affected by magnetic field which is dependent on resistivity of the target. In another simulation where beam parameters are the same as above except higher initial temperature, 200 eV [Fig. 5.16 (b)], a weaker magnetic field develops than in the case of 10 eV [Fig. 5.16(a)], which is within our expectation because resistivity drops with rising temperature following the Spitzer scaling of $\eta \sim Z/T^{(3/2)}$. Corresponding to the induced magnetic field, higher particle momentum toward the beam axis (c) and more focused beam profile (e) are seen for the initial target temperature of 10 eV, comparing to the case of 200 eV (d) and (f).

5.3.5 Study on Transport with Realistic Proton Beams

More realistically, laser-accelerated proton beams have a broad energy spectrum with a Maxwellian-like distribution $dN/dE \sim exp(-E/T_p)$ fitting to a characteristic slope temperature, T_p. The transport and stopping dynamics of a more realistic laser-accelerated proton beam with Maxwellian energy spectrum is much more complex, because the effects of what we analyzed with monoenergetic beams will combine and play roles together during the beam transport.

To investigate how general laser-accelerated proton beams traverse in the

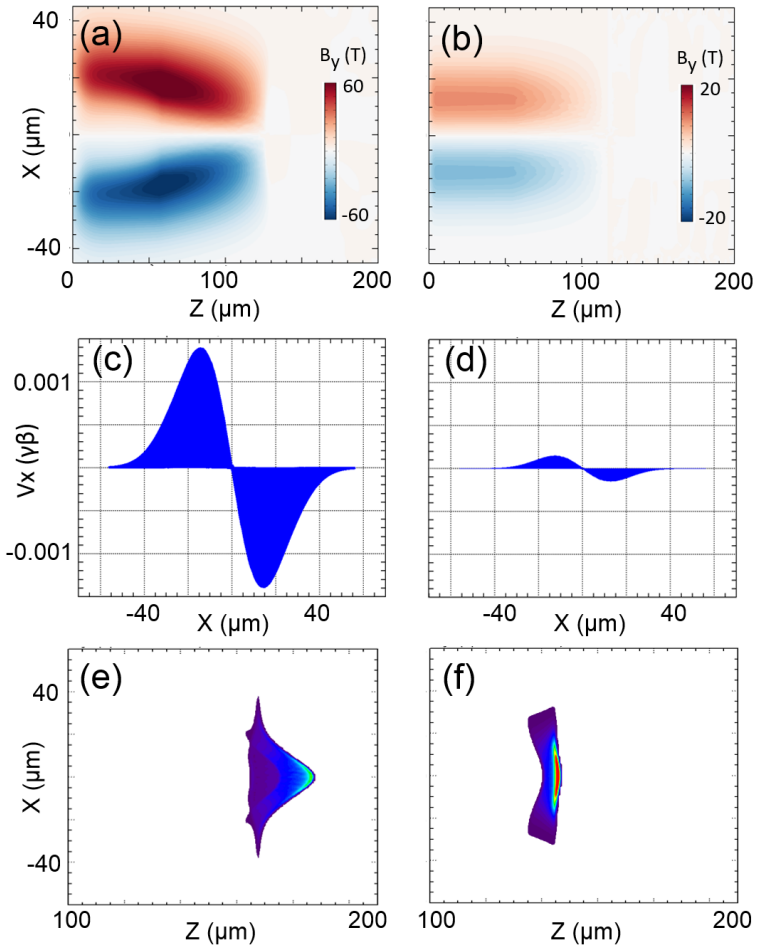

Figure 5.16: Proton beam propagation in Al target of different initial temperature for respectively 10 eV [(a, c and e)] and 200 eV [(b, d and f)], where (a) and (b) are the induced magnetic fields at 5 ps; (c) and (d) are particle phase space in the x dimension; (e) and (f) are the beam density maps at 10 ps.

solid-density target, in this work, both protons and electrons are injected in the target with the parameters representing characteristics mentioned above. Assuming laser intensity $\sim 10^{19} W/cm^2$, injected proton beam has Maxwellian energy distribution; 2.4 MeV for proton and 1.3 KeV for the co-moving electron which is relevant energies of each species for the same velocity in longitudinal direction. Other simulation setup is the same as previous monoenergetic beam study presented above in this chapter.

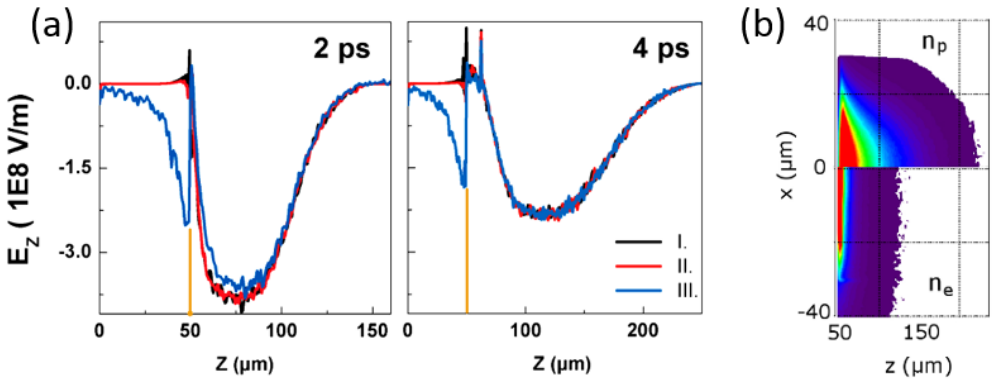

Figure 5.17: (a) Comparison of longitudinal electric field induced by proton beam in the Al target. Injected proton beams (injecting plane: 50 um) have different parameters; I: only proton, II: proton and electron (1.3 keV maxwellian), III: proton and electron (1.3 keV maxwellian with 100 keV thermal spread). Energy distribution of proton is common for the three cases as 2.4 MeV maxwellian. (b) density map of proton and electron in the Al target at 4 ps after the beam injection.

When the proton beam is injected in the target, co-moving electrons induce the negative electric field at near the injection plane. After then, only trivial difference is seen in the induced electric field comparing to other cases; injecting only the pure protons (I) and protons with electrons having energy distribution of 1.3 keV (II) and 100 keV (III), respectively as shown in Fig.5.17(a). Moreover, thermal spread of 100 keV is over estimated value than general case. Therefore, this results validate that the effect of co-moving electrons to the proton beam propagation is negligible. The is due to low stopping distance of co-moving electrons that have much lower energy comparing with the protons. As shown in Fig.5.17(b), most electrons stop at near the injection plane ($< 5\mu m$), less electron go further by thermal spread.

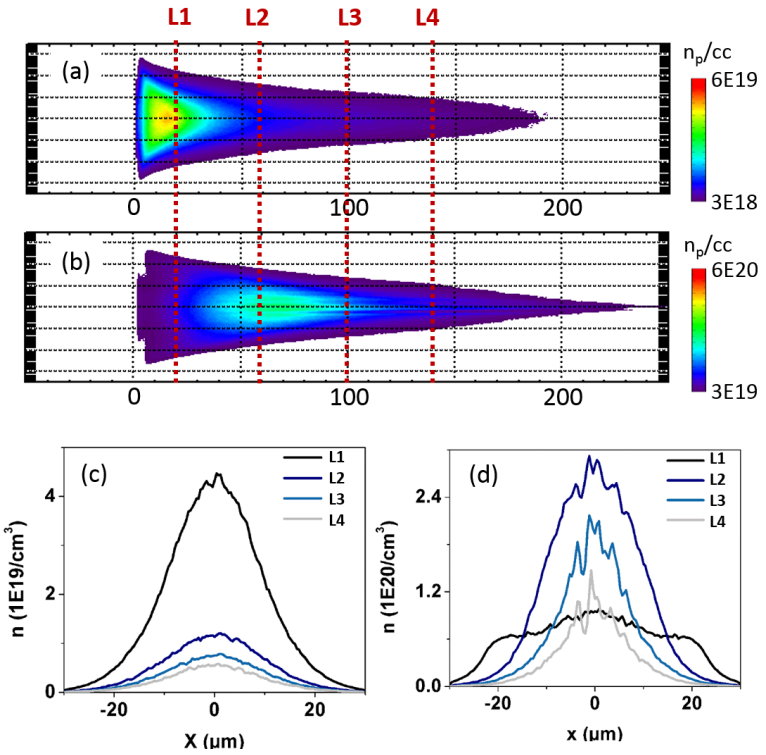

Figure 5.18: Dependence of proton beam (Maxwellian Energy) transport on the beam density. Proton density map is shown (taken in 8 ps); Injected beam current density is respectively $10^{10} A/cm^2$ (a), $10^{11} A/cm^2$ (b) in the Aluminum target. Lineouts of proton density in radial direction of (a) and (b) are shown in (c) and (d). The labeled lineout position: L1 (20 μm), L2 (60 μm), L3 (100 μm) and L4 (140 μm).

Using general parameters of laser-accelerated proton beam, dependencies of the beam transport on the beam density is studied. Since the beam has 2.4 MeV maxwellian energy distribution, the main body of the beam (dense part) locates around the tail of the beam, higher energy protons propagate further quickly. The beam main body is shifted depending on the beam density shown in (1) and (2) at Fig.5.18(a and b). This is because higher density beam heat the target more, stopping power changes as discussed in the monoenergetic beam case. Interest result here is denser beam is more focused with weak filaments, spatial density profiles show this result clearly in Fig.5.18(b and c). It is predicted that both geometric ionization affected by gaussian spatial profile of the beam and self-induced magnetic field contribute nonlinearly the beam focusing. This magnetic field effects to the beam transport is clearly shown in following comparison.

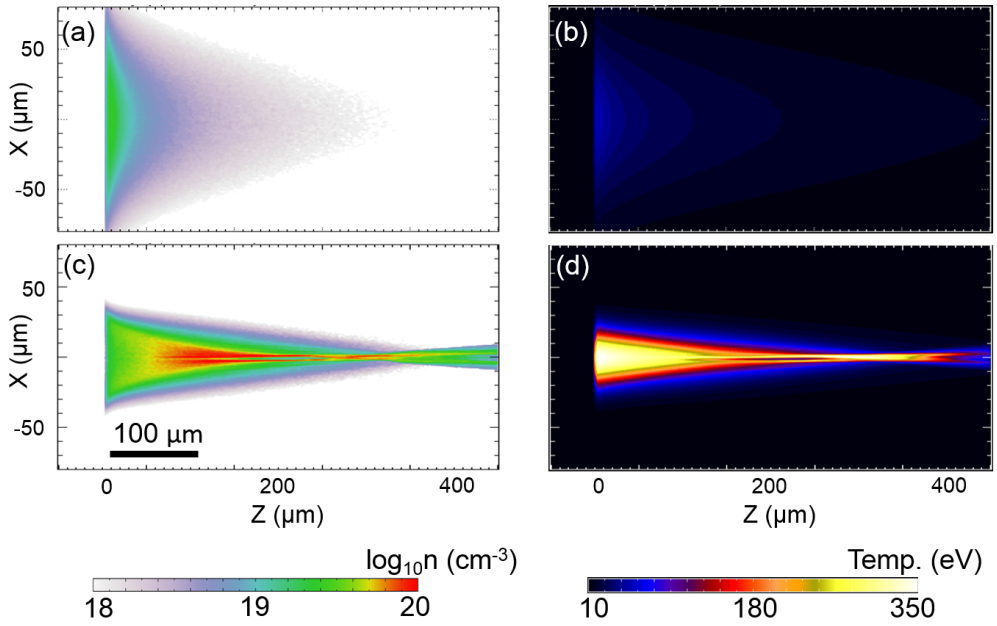

Figure 5.19: Proton density (left) and heated target temperature (right) of a Maxwellian proton beam in Al target at 20 ps. Current densities and injected beam diameter (FWHM) are respectively (a, b) $5 \times 10^9 A/cm^2$, 88 μm and (c, d) $5 \times 10^{10} A/cm^2$ and 24 μm. Both the beams have the same total energy of 6 J.

As we discussed before, laser accelerated proton beams from a spherically curved target can be focused to high enough density to heat the target to 10s eV and also further focusing of the proton beams with different target structures

have been studied. Thus, for the sake of practical beam heating applications it is important to investigate how a focused beam with Maxwellian energy distribution heats the target. Fig.5.19 compares simulation results of transport and energy deposition of a wide (current density $5 \times 10^9 A/cm^2$ and beam radius 44 μm) and a narrow ($5 \times 10^{10} A/cm^2$ and $12\mu m$) proton beam in an Al target, with the total energy being 6J in both cases. The protons are injected with only longitudinal momentum (not diverging nor focusing) and Maxwellian energy distribution having mean energy of 4 MeV and pulse duration of 5 ps for both beams. For the wide beam, the most heated region of the target is near the beam injection plane within a depth < 30 μm, and the maximum temperature is only 50 eV, shown in Fig.5.19(a) and (b). This corresponds to the fact that a large number of particles have low energy and fewer have high energy in a Maxwellian beam. However, once the beam is focused, by a product of larger current density and stronger self-generated magnetic field from small beam radius, the beam can heat the target to much higher temperature, above 350 eV, at deeper depths, $\sim 300\mu m$ [see Fig.5.19(c) and (d)]. We conclude that a focused Maxwellian beam will more efficiently heat a target to higher maximum temperature and farther distance than a divergent beam because its deposition is localized, and it is more likely to self-pinch. This result clearly shows how collective effects and nonlinearities significantly affect beam energy deposition in size-sensitive applications.

5.4 Target Heating Mechanism

Energy loss from individual protons during the beam transport is deposited in the target and causes increase in target temperature. As discussed before, these energy losses can be described in terms of stopping power which will be designated here as drag stopping, $(dE/dx)_{drag}$. Thus the temporal change rate of target temperature due to the drag heating in a beam-volume is given by

$$C_v \frac{dT}{dt}\bigg|_{drag} = \frac{j}{e}\left|\frac{dE}{dx}\right|_{drag} \tag{5.5}$$

where C_v is the targets volumetric specific heat capacity with an assumption of thermal equilibrium and j is the proton beam current density. Energy can also

deposited in the target by internal currents. As we discussed about ion beam neutralization by background electron current, proton beams draw an electron return current in a target, i.e. background electrons move in the beam propagation direction during the beams travel within the target. These electrons slowly flowing in a target experience the material's relatively high electrical resistivity, η, and the energy loss into the target from this process can be expressed with Ohms law.

$$\left.\frac{dE}{dx}\right|_{ohm} = -e\eta(T)j \tag{5.6}$$

where j is the proton current density with an assumption of current neutralization. This energy loss contributes to heating a target, and the temporal target temperature rate by the ohmic heating is expressed in the same form of equation 5.5 as

$$C_v\left.\frac{dT}{dt}\right|_{ohm} = \eta(T)j^2 \tag{5.7}$$

Therefore, in proton beam transport, drag heating by individual protons and return currents ohmic heating are the main mechanisms of the target heating as represented with equation 5.5 and 5.7 where ohmic heating depends more strongly on the beam current density as j^2. It is necessary to study what heating source is dominant in different beam density regimes for related applications that need appropriate heating in terms of quantity and position. For the electron beam transport in a solid density matter, it has been shown from theoretical and computational work that ohmic heating plays an important role when the beam current density is high ($> 10^{11} A/cm^2$). However, properties of proton beams in a solid target are different from those of electron beams, i.e. higher drag stopping power and Bragg peak-like deposition for protons, different contribution of the ohmic heating with proton beams are expected compared to electron beam cases.

In Fig. 5.20(a), the ratio of ohmic heating to drag heating in aluminum target calculated from equation 5.5 and 5.7 are plotted with various conditions of proton energy and target temperature as a function of proton beam density. For most cases with a beam density of below $10^{11} A/cm^2$, drag heating is the main heating source, while proportion of ohmic heating increases with higher density

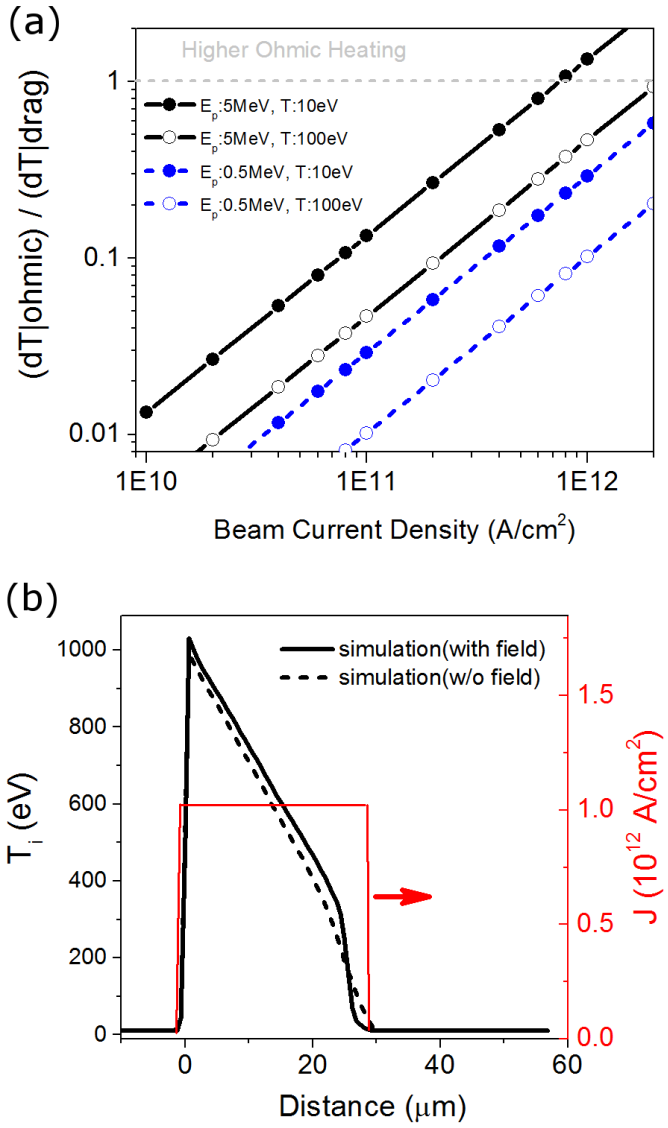

Figure 5.20: (a) Calculated proton beam heating in the Al target: the ratio of ohmic heating to drag heating as a function of beam current density with beam energies of 5 MeV and 0.5 MeV, and target temperature of 10 eV and 100 eV. (b) Measured target temperature (lineout in beam propagation direction) heated by a proton beam having a current density of $10^{12} A/cm^2$ and average energy of 5 MeV at t= 1 ps: simulation with field (solid line) and without field (dashed line).

beam, for example, both mechanisms equally contribute to the heating in a case of the beam having a current density of $7 \times 10^{11} A/cm^2$, energy of 5 MeV and background temperature of 10 eV. It is also shown that this ratio of heating source changes with proton energy with identical values for other conditions. This is because proton stopping power for low energy (see 0.5 MeV curves) is much higher than high energy (5 MeV) while ohmic heating term does not differ between the two cases. The other factor affecting the contribution of heating sources is the target temperature, i.e., as target temperature changes, the resistivity as well as the stopping power varies changing ohmic heating as shown in equation 5.7. Once a target is heated enough ($\sim$10 eV for Al target), the resistivity dependence on temperature follows the Spitzer behavior ($\eta \propto Z/T^{(3/2)}$), where resistivity drops with increase in temperature and ohmic heating is significantly reduced. From these results, it can be inferred that the ohmic heating is initially dominant but as a target is heated by the beam, and protons energies decrease during beam transport, its contribution to heating becomes insignificant compared to the drag heating. This trend is also found from the simulation results as shown in Fig. 5.20(b), where the proton beam having a current density of $10^{12} A/cm^2$ and 1 ps duration is injected into an Al target. Temperatures heated by proton beams are compared from the simulation with the field (return current included) and the one without the field updating module (i.e., the return current is not driven and drag stopping power is the only heating mechanism). At the beam front ($\sim 28\mu m$ at 1ps), the target is slightly heated to $\sim 30eV$ where ohmic heating can give significant contribution to total heating. However, the target is rapidly heated to hundreds of eV by intense protons, where lowered resistivity brings reducing ohmic heating. Therefore, little difference between heated temperature profiles by two simulations is seen.

In this chapter, we have numerically studied the stopping and transport of intense proton beams in solid-density matter by using the implicit hybrid PIC code LSP with a new implementation of an ion stopping calculation module. Both the collective beam-plasma interaction effects and proton stopping calculations were self-consistently considered in these simulations. Systematic studies with simula-

tions accounted for the dependences of proton beam transport in solid targets on the beam and target conditions. Deeper projected distances were seen for beams having higher density or longer pulse durations, which are associated with reduced proton stopping power in the target. When the proton beam was intense with a small beam radius and a high kinetic energy, the beam was tightly focused by self-generated magnetic fields, causing significant local temperature increases to hundreds of eV. Associated with the beam collective effects, the current neutralization of a proton beam by background electrons was studied, and both fluid and kinetic simulations showing good current neutralization agreed well with the theory. Proton beams with different target materials and initial temperatures also showed different transport dynamics. Lastly, two target heating mechanisms, the beam energy deposition and ohmic heating driven by the return current, were compared, and it was found that rapid target heating by an intense proton beam reduces the ohmic heating, resulting in beam energy deposition as the dominant target heating mechanism. All these results give guidelines for the energy deposition and the onset of collective effects, and thus will impact a wide range of applications, including ion/proton fast ignition and uniform volumetric heating in WDM studies.

Chapter 5, in part, is a reprint of the material as it appears in **J. Kim**, B. Qiao, C. McGuffey, M. S. Wei, P. Grabowski and F. N. Beg, "Self-Consistent Simulation of Transport and Energy Deposition of Intense Laser-Accelerated Proton Beams in Solid-Density Matter", *Physical Review Letters 115, 054801* (2015) and **J. Kim**, C. McGuffey, B. Qiao, M. S. Wei, P. Grabowski and F. N. Beg, "Varying stopping and self-focusing of intense proton beams as they heat solid density matter", *Physics of Plasmas 23, 043104* (2016). The dissertation author was the primary investigator and author of these papers.

Chapter 6

Proton Transport Experiment

6.1 Trident Experiment

To investigate the interaction of a proton beam with solid targets, the experiment was carried out on the Trident short pulse laser at the Los Alamos National Laboratory. The main object of this experiment was to measure the size of heated region after proton beams traversed through solid targets of different materials. This chapter describes the experiment setup including diagnostics and measurement results. Also, the LSP simulation of the experiment will be followed after that.

6.1.1 Experimental Setup

The Trident facility has a three beam laser system providing a wide operational range. The third beam line is a chirped pulse amplification (CPA) short pulse beam, which was used for proton generation in our work. The laser was seeded from a GLX-200 Nd:Glass (neodymium-glass) diode pumped oscillator. This output was stretched and amplified by 3 OPA (optical parametric amplification). A grating compressor recompresses the pulse and the optical parametric amplifier based pre-pulse eliminator (OPAPE) stage operates to create a cleaning the pulse. This pulse is amplified by again passing through the stretcher and amplifier chain. Provided a minimum beam, the spot size is 13 μm in diameter on target a high

quality focusing mirror. A pulse can be amplified to 100 J in 550 fs with peak intensity of $10^{20} W/cm^2$. [88] One of the great technical characteristics of this laser is its ultra-high contrast; low amplified spontaneous emission (ASE) intensity ratio. If a laser pulse has a high pre-pulse or laser pedestal, pre-plasma formed before the main laser pulse may change the conditions (specifically electron density) of the laser-target interaction. Also, a thin target has the risk being destroyed by the pre-pulse. In this experiment, laser pulses were focused through a f/8 parabolic mirror with 80 μm spot size, which was off focused to uniformly cover a large area of the target. The delivered laser had an energy of 70∼80 J, a pulse duration of 600∼700 fs, and an incidence angle of 22.5^o. For proton beam generation, a curved (partial-hemi) Au target was used to produce a focused proton beam by the TNSA mechanism. The proton beam was focused into a transport foil placed 1.7×radius away from the hemi target, as shown diagram in Fig. 6.1.

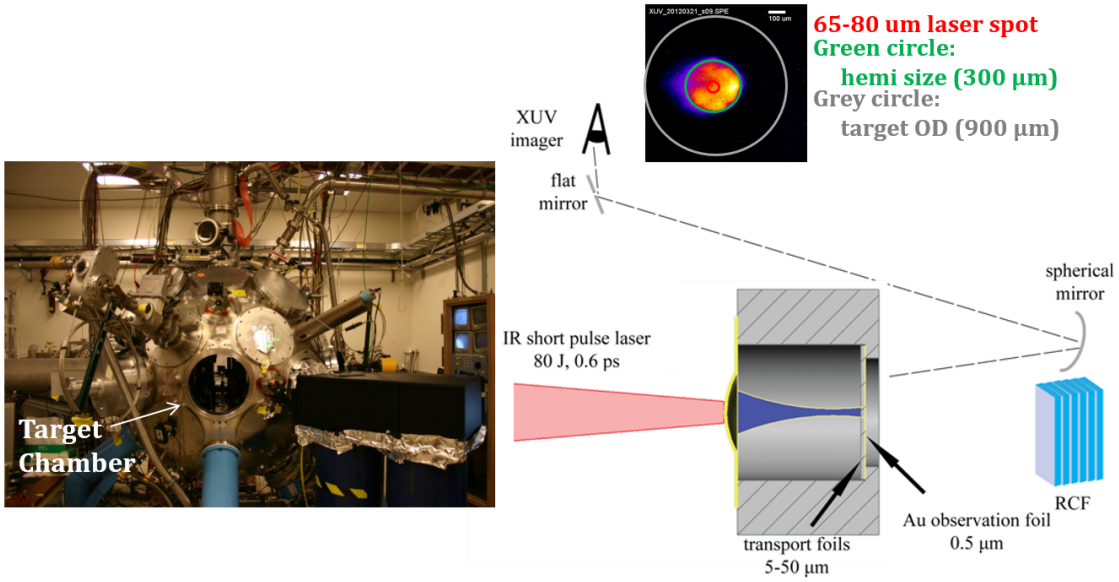

Figure 6.1: The picture of Trident laser (left). Diagram of experiment setup (right)

For a transport foil, various materials (CH, Al, Cu and Au) were used, and the foil thickness was determined with equivalent stopping range in cold matter where two energy groups (1.7 MeV and 1.0 MeV) were chosen. 0.5μm Au layer was deposited on the rear of the transport foil for imaging of the thermal emission

from the same surface. Table 6. 1 shows sets of transport foils.

Table 6.1: Transport foil sets. Various materials having different thicknesses were used based on equivalent stopping range in cold matter.

Series	**Trans. foil**	**Trans. foil**	**Trans. foil**	**Trans. foil**
High energy (1.9MeV stopped)	$50\mu m$Mylar $+0.5\mu m$ Au	$30\mu m$Al $+0.5\mu m$ Au	$15\mu m$Cu $+0.5\mu m$ Au	$12.5\mu m$Au $+0.5\mu m$ Au
Low energy (1.0MeV stopped)	$13\mu m$Mylar $+0.5\mu m$ Au	$12.5\mu m$Al $+0.5\mu m$ Au	$6\mu m$Cu $+0.5\mu m$ Au	$5\mu m$Au $+0.5\mu m$ Au

In this experiment, many diagnostic methods were used to obtain information about the electrons and protons produced during the laser-plasma interaction. The fast electron escaping from the first target was measured using an electron spectrometer, where the energetic electrons are deflected by a permanent magnet and the signal is recorded on an image plate, indicating the electrons energy distribution. To measure an energy spectrum of generated protons, RCF and Thomson Parabola were used. The main diagnostic for detecting thermal emission on the transport foil is an extreme ultraviolet (XUV) imager. As Planck found, the brightness of blackbody radiation is dependent on the temperature of a material. This phenomenon allows us to estimate a temperature of a medium by measuring its brightness of emission [89]. The Planckian emission sensitively changes; radiation intensity decreases rapidly as a target cools. Therefore, recording a time-integrated radiation signal provides the maximum surface temperature of a target. As shown in Fig. 6.1, an XUV imaging system has two mirrors. The first mirror is spherical and the second one is a flat mirror. A spherical mirror optimized for 68 eV consists of 21 pairs of layers of Mo2C and Si, and the flat mirror has 11 pairs of the same layers. [90] The spherical mirror placed with the target normal angle projects an image onto the flat mirror, where the path is deflected by 90^o. Then finally, the image passing the filter is recorded on the CCD. XUV imaging has a limitation for measuring emission brightness since the target that produces the emission expands rapidly, leading the reduction of absolute brightness. In order to find the relation between XUV brightness and the target temperature, LAS-

NEX (radiative-hydrodynamics code) simulations were run [90]. Fig. 6.2 plots the LAXNEX model results that shows the XUV brightness as a function of target temperature. Here, the detection threshold of the brightness is approximately $10^{-3} J/cm^2/sr$, which corresponds to a temperature near 20 eV.

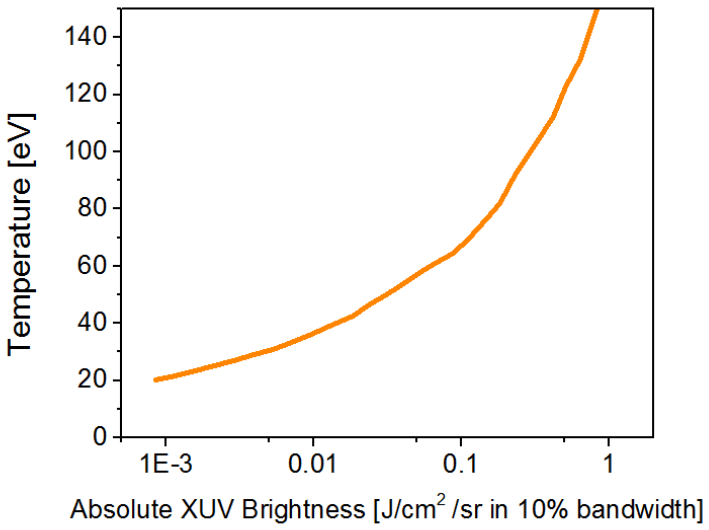

Figure 6.2: Peak target pre-expansion temperature vs absolute XUV brightness for a 25 μm Cu at 68 eV (Extracted from [90])

To measure protons produced from the Hemi target, the RCF stack was positioned behind the transport layer. Fig. 6.3 presents the RCF stack composition and proton spectrum analyzed from a RCF data for the case that a transport layer is not added. Proton slope temperature is about 2.6 MeV and, this value is similar to other shot data where dependence of protons on transport foils is not seen.

6.1.2 Measurement of XUV Emission

Fig. 6.4 presents the detected XUV images with different target and transport layers in the experiment. First of all, detected XUV emissions demonstrate the target geometry affecting the proton beam focusing. First, three XUV images (for hemi target case) show the localized emission regions due to heating by a focused proton beam. The last column shows another important test case in which

Layer	min. Energy (MeV)
Al25	
HDV2	1.5
HDV2	3.4
HDV2	4.7
HDV2	5.7
HDV2	6.6
Al100	
HDV2	8.4
HDV2	9.1
HDV2	9.8
Al100	

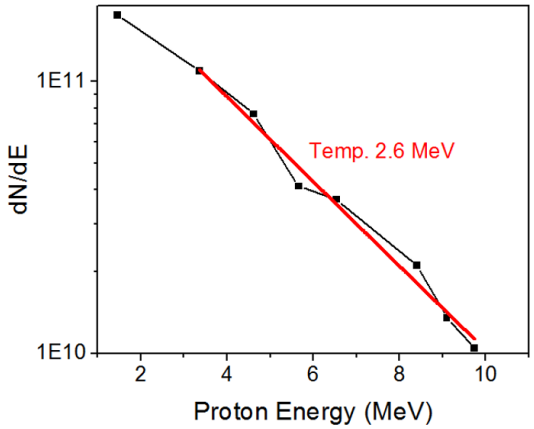

Figure 6.3: RCF stack composition (left) and analyzed proton spectrum (right) from Trident Experiment

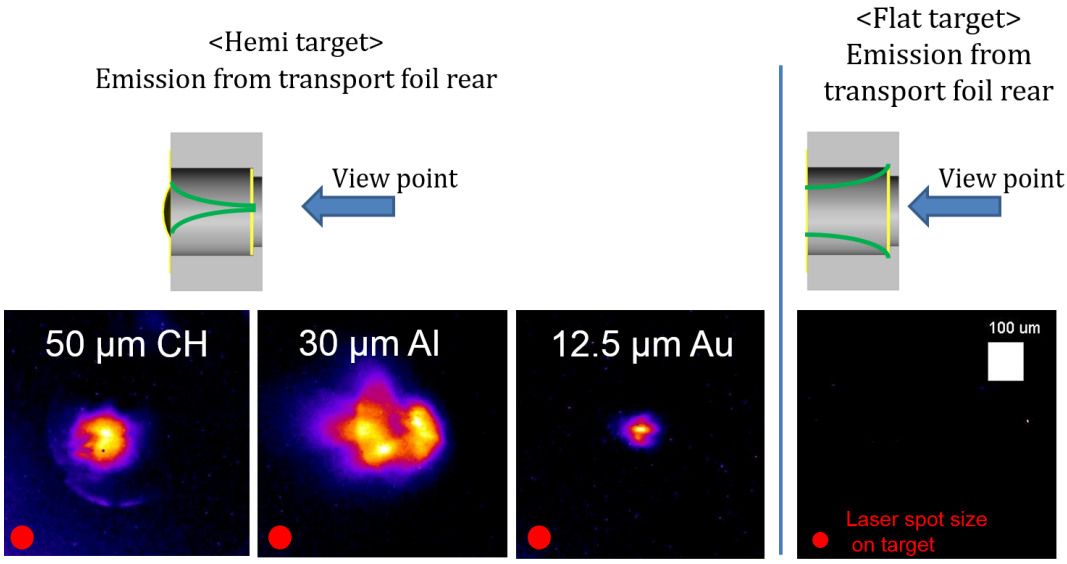

Figure 6.4: XUV emissions observed from transport foil with different materials. First three emission images are in the hemi target case and the last image is in the flat target case. Red circle indicates the laser spot size on target.

the target hemisphere was replaced with a flat Au target, meaning that the protons were not focused. No emission was detected even at a higher laser intensity with the weakest filter, which indicates at least a 3 orders of magnitude decrease in emission brightness. This demonstrates how focusing the proton beam allows the target to be isochorically heated to high temperatures.

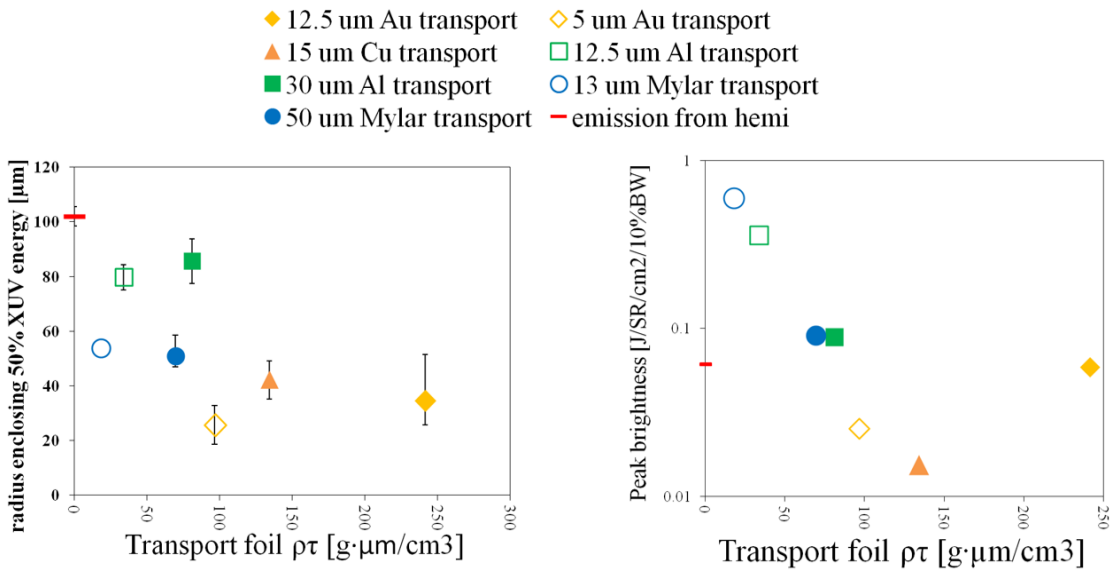

Figure 6.5: XUV emission images on different transport materials and thicknesses. Group1(equivalent stopping range: 1.7 MeV): 12.5 μm Au, 15μm Cu, 30μm Al and 50μm Mylar. Group 2(equivalent stopping range: 1MeV): 5μm Au, 12.5μm Al, 13μm Mylar. Measured XUV emission as a function of areal density of target. XUV emission size (left) and XUV peak brightness (right)

In Fig.6.5, two plots show the emission size and peak brightness as a function of areal density. On the left plot, comparing pairs of data for the same material, but different thicknesses, it is seen that the emission size is insensitive to the target thickness. For example, both the thin and thick Al (shown in green) have larger emission sizes than any other materials of various thicknesses. Au and Cu produced small spots, most of them below 50 μm FWHM, whereas the Mylar and Al were all larger than 75μm. Likewise, XUV peak brightness is plotted on the right. This comparison also shows how the dependence of brightness on thickness is not clear. However, what we can find from both plots is that low areal density (low z material) show larger emission size and brighter signal than

higher areal density materials. For these foils of whole materials, Monte Carlo and nuclear scattering formulas predicts a size increase of only ∼10 microns. But these data cover a much wider range, from 30 μm to 80 μm. For these results it can be concluded that transport for these high intensity beams cannot be explained by cold stopping and scattering models alone. Thus, for the interpretation of experimental observation, computational modeling was conducted using LSP. Details of this modeling will be discussed in the following subchapter.

6.2 Computational Modeling

Simulation modeling was conducted in two separate ways. First, proton beams produced in the experiment were modeled using a LSP simulation to obtain the proton beam source to be used in the transport simulations. The simulation method for the proton beam generation was identical to the one discussed earlier in this dissertation (see Chapter 3), except for parameters regarding the electron source injected into the target.

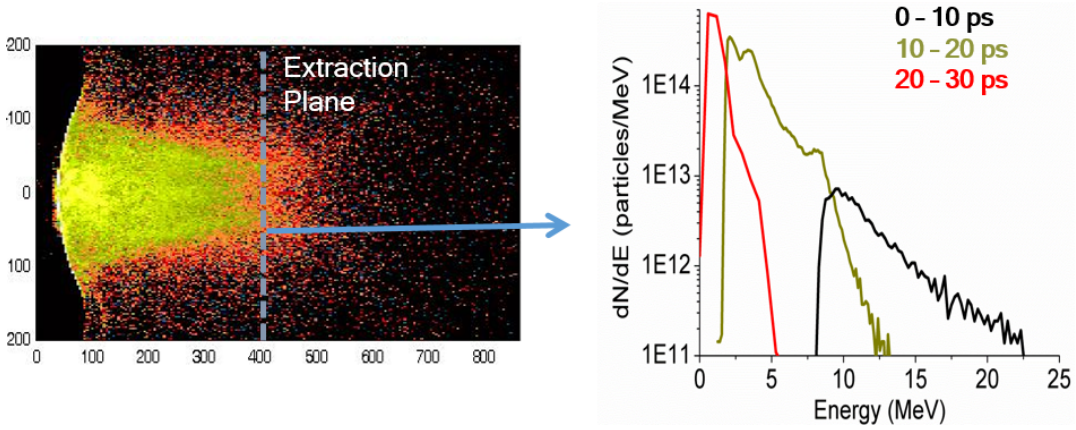

Figure 6.6: Snap image of protons produced from a hemi-target in the simulation (left). Proton energy spectra obtained from extraction plane (right). Each proton spectrum is time integrated with 10ps duration.

Two main characteristics of the proton beam found from the simulation modeling are that the proton energy distribution changes in time and the beam has a non-uniform energy spatial profile. As shown in Fig.6.6, the energy spectrum

varies with different time ranges. Here, spectra with three different time group were measured at the extraction plane ($400\mu m$). Fast moving protons, reaching the plane from 0 to 10 ps, have a higher slope temperature, while lower energy protons, for example, the third group (20-30 ps), shows relatively low slope temperatures. The second property of the proton beam is that higher energy protons are located closer to the z-axis (longitudinal axis). Whereas, lower energy protons are distributed broadly in a radial direction. Based on these spatial and temporal energy spectra, two proton beams were reconstructed for transport simulation. For onsidering a transport simulation time of approximately 30 ps, simulations including both proton beam generation and transport in different materials are computationally very expensive. Thus, simulations for transport studies were conducted using reconstructed proton beams. Detailed parameters of injected proton beams and schematic of the simulation are shown in Fig. 6.7. The first beam represents high energy protons having the 2.3 MeV Maxwellian energy distribution and 7ps duration. Note that this slope temperature is similar to the measured value from the experimental results, as shown in Fig. 6.3. The second beam has low energy protons ($<$ 2.2 MeV) with a 0.8 MeV slope temperature and 13ps duration. The total beam energy (summation of the two beams) is 1.2 J, which is about 1.5% conversion efficiency of laser-to-proton.

In the experiment, the most varying XUV emissions were seen from Al and Cu in the same stopping range ($30\mu m$ Al and $15\mu m$ Cu), as already shown in Fig.6.5. We compared these two transport layers in the simulation modeling. Once protons pass through a transport layer (Al or Cu), the proton data is recorded in the extraction plane and reinjected from that plane into an Au target. This separated simulation is due to the fact that the EOS for multi materials is not allowed in the LSP simulation. The last extraction plane is positioned at 0.5 μm inside the Au, where 0.5 μm is the thickness of Au layer added rear of the transport foil in the experiment. The proton energy fluxes are compared in Fig.6.8 where the number of proton and its energy are measured when protons leave the transport layer, Al or Cu. For the simulation using dynamic updating stopping power, Fig.6.8 (a) a distinction is found (higher energy flux for Al transport layer)

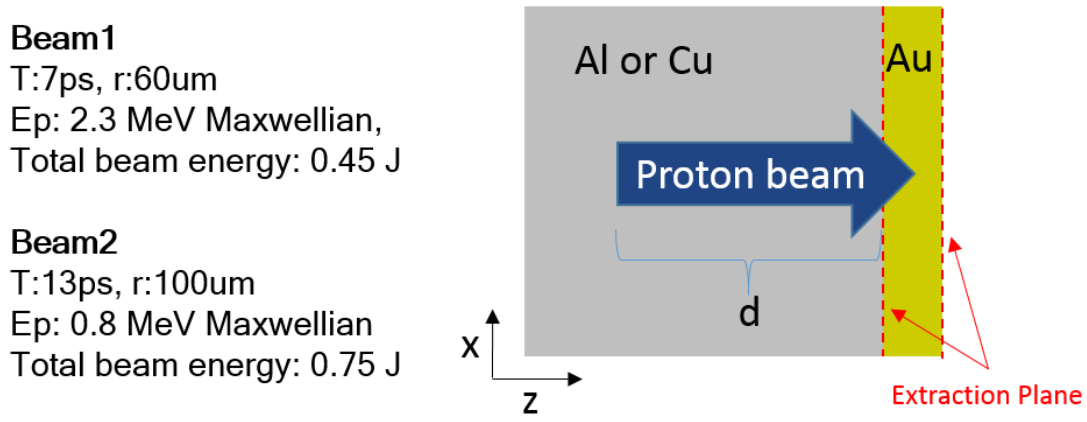

Figure 6.7: Schematic of the transport simulation. The parameters of two beams are characterized by previous proton generation simulation. Distance, d, varies with transport layer; Al case: $30\mu m$, Cu case: $15\mu m$. Extraction plane is set at $0.5\mu m$ in the Au target.

between two material cases, while similar results are shown in the case of fixed stopping power (cold stopping is applied) Fig.6.8 (b). Since the thicknesses of the two materials were determined by cold stopping range, similar energy fluxes with cold stopping is not surprising, but different energy fluxes with updating stopping power is an unexpected result. It is inferred that proton stopping power changes during the beam transport in a layer (particularly, in the Al layer), with the varying thermodynamic states of the layer. As an example, Fig.6.9 shows the temperature of the Al transport layer changing over time. At 7 ps (a), only fast moving protons are in the layer (the first beam injected), and the heated temperature is low (< 10 eV) due to that stopping power of protons for high energy range being relatively low. In other words, most of the protons pass through the layer without energy deposition. When low energy protons are injected (the second beam after 7 ps), the Al layer is heated up to 20 eV in14ps, which is hot enough for protons to move deeply with reduced stopping power and, finally, the layer is heated up to 40 eV near the injection plane.

Total proton energy fluxes deposited in the Au layer after passing through transport layers (Al and Cu) are shown in Fig. 6.10. This result indicates that protons through Al layer deposit more energy than the ones through Cu layer into

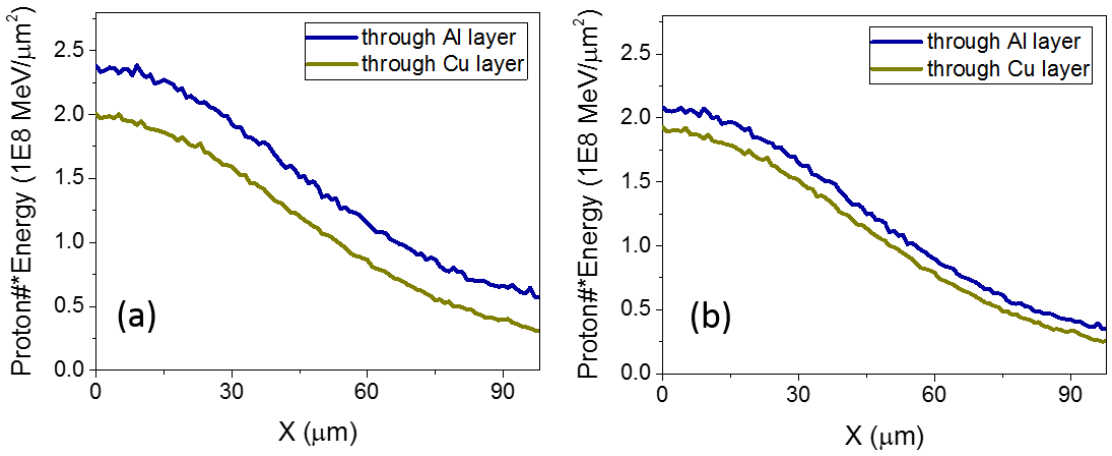

Figure 6.8: Time integrated proton energy flux in x-axis measured when leaving from transport layer ($30\mu m$ Al or $15\mu m$ Cu). The simulations are conducted with the dynamic changing stopping power (a) and cold stopping power (fixed stopping) (b).

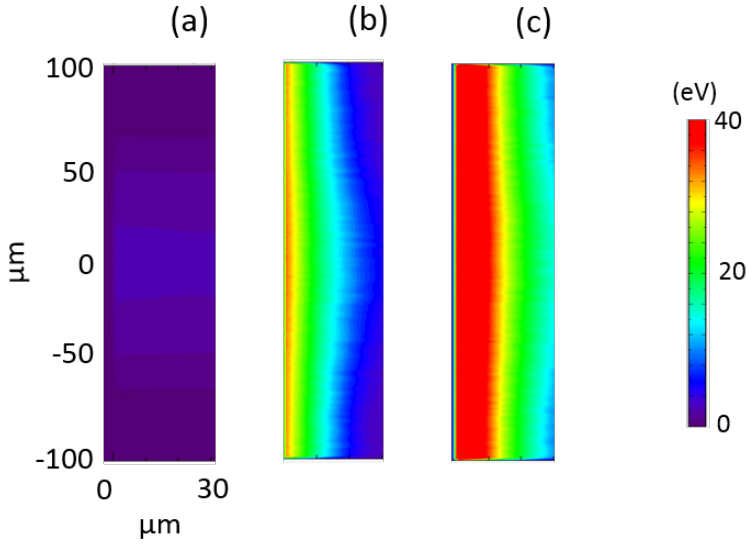

Figure 6.9: Aluminum target temperature varying with the proton transport. Time for snap images are 7ps (a), 14ps (b) and 21ps (c), respectively.

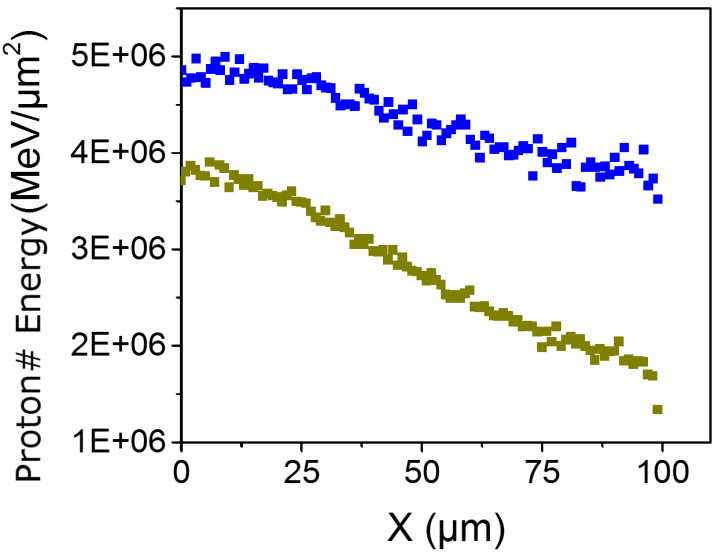

Figure 6.10: Time integrated proton energy flux that is deposited in Au layer (up to 50 μm). Proton energy flux through Al layer and Cu layer are shown in blue and dark yellow dots.

the Au layer. The heated temperature via the energy flux can be calculated. For example, energy flux through Al layer is 4.8e6 $MeV/\mu m^2$ at the first bin (0-1 μm) which can be converted to $7.68 \times 10^{-7} J/\mu m^2$ meaning that total proton energy deposition in Au (volume of $0.5 \times 1 \times 1 \mu m^3$) is 3.84×10^{-7}J. From the specific heat capacity and density of solid Au, volumetric heat capacity can be driven as $2.43 \times 10^{-12} J/(K\mu m^3)$. Using this capacity, calculated Au temperature from deposited proton energy, 3.84×10^{-7} J is 27 eV.

Corresponding to the energy flux deposited in the Au layer, the Au layer is heated more in the case of Al transport, as shown in Fig.6.11. The one important feature we can find from these results is the gradual temperature slope in the transverse direction in the Al case compared to the Cu case. If we look at the heated temperature above the XUV detection level, the Al case has a much broader area, which is identical to the trend we observed in the experiment (see Fig.6.5). This pattern is also found in the simulations that use a cold stopping, plotted with a dashed line in the figure. Interestingly, temperatures in both cases (Al, Cu) are below detection levels, indicating that we may not have observed any emission

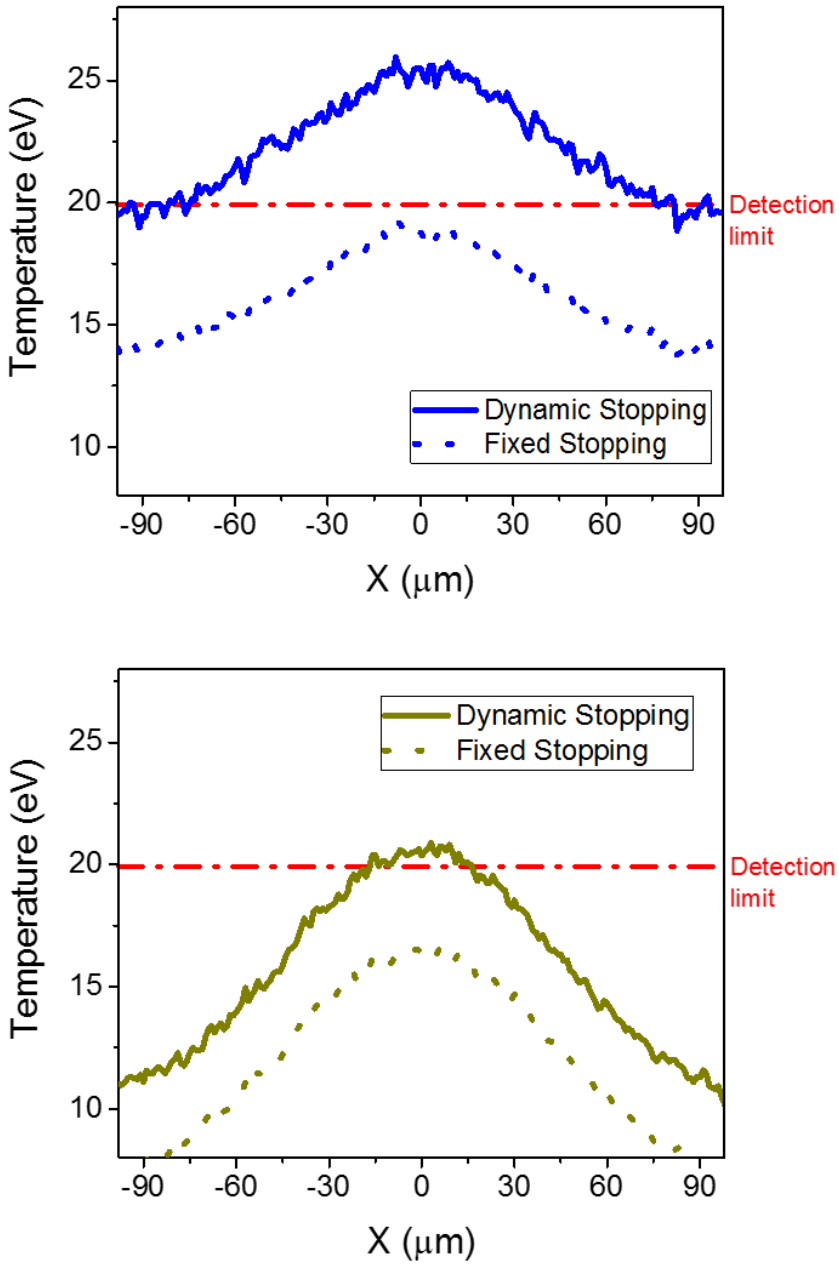

Figure 6.11: Spatial temperature profile of Au target at $0.5\mu m$ depth. Through Al transport layer (Top) and Through Cu transport layer (Bottom). Solid line and dotted line respectively indicate the simulation with dynamic stopping power and simulation with fixed stopping (NIST stopping).

unless the stopping power changes with a target thermodynamic state. Remember that the first proton beam and second proton beam have beam diameters of $60\mu m$ and $100\mu m$, respectively. The beam central area is heated by both beams, but only the second beam (low energy protons) contributes to the heating of the wing side (radially outer side). From spatial temperature profiles of these two cases [see Fig.6.11], it can be drawn that low energy protons (the second beam with larger diameter) result in a clear distinction of heating profile at the wing side for the two different material cases.

The peak temperatures of the Au for two cases are approximately 26 eV (Al case) and 20 eV (Cu case), as shown in Fig.6.11. The temperature difference of 6 eV enhances the brightness of XUV emission by a factor of 3, according to the LASNEX simulation shown in Fig.6.2. This increased brightness is also consistent with a prediction using the Stefan-Boltzmann law, which describes the total power of black-body radiation depending on the object's temperature with the relation $j = \sigma T^4$, where j, σ and T are irradiance, Stefan-Boltzmann constant and temperature, respectively. In the experiment, 3-4 times higher XUV brightness was measured from Al case compared to the Cu case. Thus, a good overall agreement is found between the theoretical prediction and the experimental result. Additionally, the induced magnetic field during proton beam transport was measured in the simulation to see if the magnetic field had any influence on beam profiles in different materials. However, the proton beam was not intense enough to produce high magnetic fields, (the maximum magnetic field is below 10 Tesla for a given proton beam) and it can not affect the beam transport in a thin foil (10s of micron thickness).

In this work, the experiments showed that the size and brightness of XUV emissions produced by proton beams vary with the target material, and this result thus demonstrated the dependence of material on proton beam transport. Simulation modelling of the experiments appeared to be consistent with the experimental measurements in terms of heating profile and temperature for different material. These simulations gave an explanation why varying stopping power with temperature in different materials can significantly change the heating profile rather than

the effects of beam scattering or induced magnetic field for the given proton beam density.

Chapter 7

Summary and Conclusions

Intense proton beams are appealing for their potential applications in the fast ignition of inertial confinement fusion and a broad range of nuclear research fields. Moreover, they are widely used to achieve isochoric heating, as they can penetrate deeply into a medium and provide volumetric heating profiles compared to other resources, such as the laser and electron beams. This volumetric, isochoric heating enables fundamental material studies, including electron-ion equilibrium and equation of state measurement. For those applications, an understanding of both the proton beam transport and the target heating is crucial. Additionally, further investigation of intense beam generation is of particular interest to the proton fast ignition of ICF among those applications. In this dissertation, both intense proton beam generation and transport in solid density matter have been studied through experiments and numerical simulations.

Previous studies, including experiments and PIC simulations, have shown that the enclosed structures attached to the curved target can result in focusing of proton beams. This focusability is due to hot electrons accelerated by the laser-target interaction. As hot electrons escape into the enclosed structures, transverse electric fields are induced and protons are pushed inward. In this work, discussed in Chapter 4, the experiments were carried out using the Omega EP laser, which has a high energy (1 kJ) and long pulse duration (10 ps). These laser parameters are the most unique feature of this work, compared to previous studies. Additionally, measurement of Cu K_α radiation on the secondary foil was included to

visualize the focused beam profile. Experimental results clearly showed the dependence Cu K_α emissions on the target geometry, indicating higher beam focusability from enclosed structure targets. Compared to a free standing target (without enclosed structures), the cone-assembled target presented a focused Cu K_α signal ($\sim 100\mu m$ FWHM) with a higher yield (8x higher peak). Numerical modeling of the experiment using hybrid-PIC code LSP showed an order higher number density of particles in focused proton beams than in the case of hot electrons located on the secondary foil. This simulation result validates that Cu K_α signal as mostly driven by focused proton beam rather than hot electrons traveling through the structure. Furthermore, images observed on proton radiography indicate the existence of transverse fields on a structured target, and this evolution of fields appears to be consistent with simulation results. These results demonstrate that the focusability of a proton beam with the enclosed target is improved by a long pulse duration of the laser, because electric fields driven by hot electrons can be maintained for a long time and provide a contribution to the beam focusing.

Along with beam focusing, another way to make the proton beam intense is to enhance the conversion efficiency of laser-to-protons. The second experiment in Chapter 4 showed the dependence of conversion efficiency on target geometry. The smaller leg target (isolated target) exhibited higher dose on RCF measurement, indicating that more protons were produced from the isolated target. The high experimental uncertainty (large error bars) inhibit a perfect comparison of trends. However, these results demonstrate the possibility of an increase in the conversion efficiency of laser-to-proton.

Regarding proton beam transport, the stopping power of individual protons in cold materials is well understood, and many studies have been conducted on the transport of relatively low density proton beam in plasmas. However, an intense proton beam interacting with solid-density matter is still not well understood. When intense beams enter into matter, the thermodynamic state of the matter significantly changes and beam collective behavior becomes important. Thus, both the matter's response to the beam and the beam response to the matter need to be considered simultaneously for accurate estimation of beam transport. To study

this regime, a new proton stopping power module covering both cold solid density and WDM regimes was implemented in the hybrid PIC code LSP, as presented in Chapter 3. With this capability, self-consistent simulation of transport and energy deposition of intense proton beams in solid density matter have been investigated. Firstly, as shown in Chapter 5, systematic studies under various conditions of beam and targets showed the dependences of proton beam transport on beam density, beam pulse duration, target material, and target initial temperature. Deeper projected distances were seen from higher density beams ($> 10^{18}/cm^3$) and longer beam pulse duration ($> 1ps$). This increase in projected ranges is associated with varying proton stopping power. Specifically, in a target region heated by an intense proton beam, the stopping power of protons (especially the relatively low energy proton) decreases, causing enhanced projected range in a target. Note that all simulations in this dissertation were done in 2D coordinates. Although 3D PIC simulations are very computationally expensive, it may be important to extend our work to the 3D case to see effects that possibly come from the additional dimension. In particular, this may be important to the observed magnetic field growth and beam pinching.

Both kinetic and fluid simulations showing charge and current neutralization of the proton beam during transport were consistent with theory. Background electrons (return current) enabling beam neutralization appeared to be important for beam collective effects as they affect the generation of magnetic field. The self-induced magnetic fields were stronger in the case of high density and narrow beam spot size. Moreover, given the same total beam energy, a narrow (small spot size) proton beam heats the target much deeper and to a higher temperature because the beam is tightly focused by strong magnetic fields, resulting in increased local temperatures to hundreds of eV. These results inform us that the collective effects need to be considered for the intense beam applications requiring high energy deposition in a small area, such as proton fast ignition ($< 40\mu m$). Additionally, these results provide guidelines for the onset of collective effects. This guidance will be useful for a wide range of applications, including uniform volumetric heating for creation of WDM state samples for exotic material studies. Simulations

in this work showed that even beams with an energy lower than 10J can heat a target up to 100s of eV if that beam is tightly focused. Existing world-class lasers, such as the OMEGA EP, are capable of delivering energies > 1 kJ, which could potentially produce proton beams with up to 100J if the conversion efficiency is approximately10%. Therefore, applying the techniques of proton beam focusing, beam collective effects and heating (up to 100s eV) will be observable at existing facilities.

The experimental results conducted on the Trident laser, in Chapter 6, presented material effects on proton beam transport as the size and brightness of the XUV emissions produced by proton beam varied with the target material. Simulations of the experiments appeared to be consistent with experimental measurements, in terms of heating profile and temperature in a different material (wider, brighter emission with low Z material). These simulations give an explanation for how varying stopping power with temperature in a different material can significantly change beam heating profiles, rather than effects of beam scattering or beam collective effects. Proton beams produced during the experiment were not intense enough to induce strong magnetic fields (the maximum magnetic field observed in the simulation is below 10 Tesla for the proton beam investigated), and this weak magnetic field hardly affected the proton beam transport in the thin target ($< 50\mu m$). Therefore, under these conditions, varying stopping power played the major role in different heating profiles, depending on the materials. However, in future experiments on tightly focus intense proton beams into thicker transport targets, significant stopping range modifications and beam collective effects may be observable and studied as functions of target material.

Bibliography

[1] R. P. Drake, *High-Energy-Density Physics*. Springer, 2006.

[2] A. Pelka, G. Gregori, D. O. Gericke, J. Vorberger, S. H. Glenzer, M. M. Gunther, K. Harres, R. Heathcote, A. L. Kritcher, N. L. Kugland, B. Li, M. Makita, J. Mithen, D. Neely, C. Niemann, A. Otten, D. Riley, G. Schaumann, M. Schollmeier, A. Tauschwitz, and M. Roth, "Ultrafast melting of carbon induced by intense proton beams," *Physics Review Letters*, vol. 105, p. 265701, 2010.

[3] T. G. White, N. J. Hartley, B. Borm, B. J. B. Crowley, J. O. Harris, D. C. Hochhaus, T. Kaempfer, K. Li, P. Neumayer, L. K. Pattison, F. Pfeifer, S. Richardson, A. P. L. Robinson, I. Uschmann, and G. Gregori, "Electron-ion equilibration in ultrafast heated graphite," *Physics Review Letters*, vol. 112, p. 145005, 2014.

[4] G. M. Dyer, A. C. Bernstein, B. I. Cho, J. Osterholz, W. Grigsby, A. Dalton, R. Shepherd, Y. Ping, H. Chen, K. Widmann, and T. Ditmire, "Equation-of-state measurement of dense plasma heated with fast protons," *Physics Review Letters*, vol. 101, p. 015002, 2008.

[5] S. Atzeni and J. Meyer-Ter-Vehn, *The physics of inertial fusion: Beam plasma interaction, hydrodynamics, hot dense matter*. Oxford University Press, 2004.

[6] M. H. Key, "Status of and prospects for the fast ignition inertial fusion concept," *Physics of Plasmas*, vol. 14, p. 055502, 2007.

[7] R. Betti, V. N. Goncharov, R. L. McCrory, and C. P. Verdon, "Growth rates of the ablative rayleigh-taylor instability in inertial confinement fusion," *Physics of Plasmas*, vol. 5, no. 5, p. 1446, 1998.

[8] H.-S. Park, O. A. Hurricane, D. A. Callahan, D. T. Casey, E. L. Dewald, T. R. Dittrich, T. Doppner, D. E. Hinkel, L. F. B. Hopkins, S. L. Pape, T. Ma, P. K. Patel, B. A. Remington, H. F. Robey, J. D. Salmonson, and J. L. Kline, "High-adiabat high-foot inertial confinement fusion implosion experiments on the national ignition facility," *Physical Review Letters*, vol. 112, p. 055001, 2014.

[9] O. A. Hurricane, D. A. Callahan, D. T. Casey, P. M. Celliers, C. Cerjan, E. L. Dewald, T. R. Dittrich, T. Dppner, D. E. Hinkel, L. F. B. Hopkins, J. L. Kline, S. L. Pape, T. Ma, A. G. MacPhee, J. L. Milovich, A. Pak, H.-S. Park, P. K. Patel, B. A. Remington, J. D. Salmonson, P. T. Springer, and R. Tommasini, "Fuel gain exceeding unity in an inertially confined fusion implosion," *Nature*, vol. 506, pp. 343–348, 2014.

[10] T. Ma, O. Hurricane, D. Callahan, M. Barrios, D. Casey, E. Dewald, T. Dittrich, T. Doppner, S. Haan, D. Hinkel, L. B. Hopkins, S. L. Pape, A. MacPhee, A. Pak, H.-S. Park, P. Patel, B. Remington, H. Robey, J. Salmonson, P. Springer, R. Tommasini, L. Benedetti, R. Bionta, E. Bond, D. Bradley, J. Caggiano, P. Celliers, C. Cerjan, J. Church, S. Dixit, R. Dylla-Spears, D. Edgell, M. Edwards, J. Field, D. Fittinghoff, J. Frenje, M. G. Johnson, G. Grim, N. Guler, R. Hatarik, H. Herrmann, W. Hsing, N. Izumi, O. Jones, S. Khan, J. Kilkenny, J. Knauer, T. Kohut, B. Kozioziemski, A. Kritcher, G. Kyrala, O. Landen, B. MacGowan, A. Mackinnon, N. Meezan, F. Merrill, J. Moody, S. Nagel, A. Nikroo, T. Parham, J. Ralph, M. Rosen, J. Rygg, J. Sater, D. Sayre, M. Schneider, D. Shaughnessy, B. Spears, R. Town, P. Volegov, A. Wan, K. Widmann, C. Wilde, , and C. Yeamans, "Thin shell, high velocity inertial confinement fusion implosions on the national ignition facility," *Physical Review Letters*, vol. 114, p. 145004, 2015.

[11] T. R. Dittrich, O. A. Hurricane, D. A. Callahan, E. L. Dewald, T. Doppner, D. E. Hinkel, L. F. B. Hopkins, S. L. Pape, T. Ma, J. L. Milovich, J. C. Moreno, P. K. Patel, H.-S. Park, B. A. Remington, and J. D. Salmonson, "Design of a high-foot high-adiabat icf capsule for the national ignition facility," *Physical Review Letters*, vol. 112, p. 055002, 2014.

[12] S. Atzeni, "Inertial fusion fast ignitor: Igniting pulse parameter window vs the penetration depth of the heating particles and the density of the precompressed fuel," *Physics of Plasmas*, vol. 6, no. 8, p. 3316, 1999.

[13] M. Tabak, J. Hammer, M. E. Glinsky, W. L. Kruer, S. C. Wilks, J. Woodworth, E. M. Campbell, and M. D. Perry, "Ignition and high gain with ultrapowerful lasers," *Physics of Plasmas*, vol. 1, p. 1626, 1994.

[14] R. Kodama, P. A. Norreys, K. Mima, A. E. Dangor, R. G. Evans, H. Fujita, Y. Kitagawa, K. Krushelnick, T. Miyakoshi, N. Miyanaga, T. Norimatsu, S. J. Rose, T. Shozaki, K. Shigemori, A. Sunahara, M. Tampo, K. A. Tanaka, Y. Toyama, T. Yamanaka, and M. Zepf, "Fast heating of ultrahigh-density plasma as a step towards laser fusion ignition," *Nature*, vol. 412, pp. 798–802, 2001.

[15] M. H. Key, R. R. Freeman, S. P. Hatchett, A. J. MacKinnon, P. K. Patel,

R. A. Snavely, and R. B. Stephens, "Proton fast ignition," *Fusion Science and Technology*, vol. 49, no. 3, pp. 440–452, 2006.

[16] J. J. Honrubia, J. C. Fernandez, M. Temporal, B. M. Hegelich, and J. M. ter Vehn, "Fast ignition of inertial fusion targets by laser-driven carbon beams," *Physics of Plasmas*, vol. 16, p. 102701, 2009.

[17] S. Atzeni, M. Temporal, and J. J. Honrubia, "A first analysis of fast ignition of precompressed icf fuel by laser-accelerated protons," *Nucl. Fusion*, vol. 42, 2002.

[18] A. P. L. Robinson, M. Zepf, S. Kar, R. G. Evans, and C. Bellei, "Thin-foil expansion into a vacuum," *New Journal of Physics*, vol. 10, p. 013021, 2008.

[19] H. Daido, M. Nishiuchi, and A. S. Pirozhkov, "Review of laser-driven ion sources and their applications," *Rep. Prog. Phys*, vol. 75, p. 056401, 2012.

[20] J. C. Fernandez, B. J. Albright, F. N. Beg, M. E. Foord, B. M. Hegelich, J. J. Honrubia, M. Roth, R. B. Stephens, and L. Yin, "Fast ignition with laser-driven proton and ion beams," *Nucl. Fusion*, vol. 54, p. 054006, 2014.

[21] P. Gibbon, *Short pulse laser interactions with matter*. Imperial college press, 2005.

[22] W. L. Kruer, *The physics of laser plasma interactions*. West view press, 2003.

[23] S. C. Wilks and W. L. Kruer, "Absorption of ultrashort, ultra-intense laser light by solids and overdense plasmas," *IEEE Journal of Quantum Electronics*, vol. 33, p. 1954, 1997.

[24] F. Brunel, "Not-so-resonant, resonant absorption," *Physical Review Letters*, vol. 59, pp. 52–55, 1987.

[25] W. L. Kruer and K. Estabrook, "J x b heating by very intense laser light," *Physics of Fluids*, vol. 28, pp. 430–432, 1985.

[26] S. C. Wilks, W. L. Kruer, M. Tabak, and A. B. Langdon, "Absorption of ultra-intense laser pulse," *Physical Review Letters*, vol. 69, no. 9, p. 1383, 1992.

[27] F. N. Beg, A. R. Bell, A. E. Dangor, C. N. Danson, A. P. Fews, M. E. Glinsky, B. A. Hammel, P. Lee, P. A. Norreys, and M. Tatarakis, "A study of picosecond laser-solid interactions up to $10^19 w/cm^2$.," *Physics of Plasmas*, vol. 4, p. 447, 1997.

[28] R. A. Snavely, M. H. Key, S. P. Hatchett, T. E. Cowan, M. Roth, T. W. Phillips, M. A. Stoyer, E. A. Henry, T. C. Sangster, M. S. Singh, S. C. Wilks, A. MacKinnon, A. Offenberger, D. M. Pennington, K. Yasuike, A. B. Langdon, B. F. Lasinski, J. Johnson, M. D. Perry, and E. M. Campbell, "Intense high-energy proton beams from petawatt-laser irradiation of solids," *Physical Review Letters*, vol. 85, p. 2945, 2000.

[29] P. K. Patel, A. J. Mackinnon, M. H. Key, T. E. Cowan, M. E. Foord, M. Allen, D. F. Price, H. Ruhl, P. T. Springer, and R. Stephens, "Isochoric heating of solid-density matter with an ultrafast proton beam," *Physical Review Letters*, vol. 91, no. 12, p. 125004, 2003.

[30] S. C. Wilks, A. B. Langdon, T. E. Cowan, M. Roth, M. Singh, S. Hatchett, M. H. Key, D. Pennington, A. MacKinnon, and R. A. Snavely, "Energetic proton generation in ultra-intense lasersolid interactions," *Physics of Plasmas*, vol. 8, p. 542, 2001.

[31] P. Mora, "Plasma expansion into a vacuum," *Physical Review Letters*, vol. 90, no. 18, p. 185002, 2003.

[32] S. P. Hatchett, C. G. Brown, T. E. Cowan, E. A. Henry, J. S. Johnson, M. H. Key, J. A. Koch, A. B. Langdon, B. F. Lasinski, R. W. Lee, A. J. Mackinnon, D. M. Pennington, M. D. Perry, T. W. Phillips, M. Roth, T. C. Sangster, M. S. Singh, R. A. Snavely, M. A. Stoyer, S. C. Wilks, and K. Yasuike, "Electron, photon, and ion beams from the relativistic interaction of petawatt laser pulses with solid targets," *Physics of Plasmas*, vol. 7, p. 2076, 2000.

[33] J. E. Crow, P. L. Auer, and J. E. Allen, "The expansion of a plasma into a vacuum," *J. Plasma Physics*, vol. 14, pp. 65–76, 1975.

[34] P. Mora, "Thin-foil expansion into a vacuum," *Physical Review E*, vol. 72, p. 056401, 2005.

[35] P. Mora and T. Grismayer, "Rarefaction acceleration and kinetic effects in thin-foil expansion into a vacuum," *Physical Review Letters*, vol. 102, p. 145001, 2009.

[36] Y. Sentoku, T. E. Cowan, A. Kemp, and H. Ruhl, "High energy proton acceleration in interaction of short laser pulse with dense plasma target," *Physics of Plasmas*, vol. 10, no. 5, p. 2009, 2003.

[37] L. Robson, P. T. Simpson, R. J. Clarke, K. W. D. Ledingham, F. Lindau5, O. Lundh, T. McCanny, P. Mora, D. Neely, C.-G. Wahlstrom, M. Zepf, and P. McKenna, "Scaling of proton acceleration driven by petawatt-laser-plasma interactions," *Nature Physics*, vol. 3, pp. 58–62, 2007.

[38] S. A. Gaillard, T. Kluge, K. A. Flippo, M. Bussmann, B. Gall, T. Lockard, M. Geissel, D. T. Offermann, M. Schollmeier, Y. Sentoku, and T. E. Cowan, "Increased laser-accelerated proton energies via direct laser-light-pressure acceleration of electrons in microcone targets," *Physics of Plasmas*, vol. 55, p. 056710, 2010.

[39] T. Esirkepov, M. Borghesi, S. V. Bulanov, G. Mourou, and T. Tajima, "Highly efficient relativistic-ion generation in the laser-piston regime," *Physical Review Letters*, vol. 92, p. 175003, 2004.

[40] T. Schlegel, N. Naumova, V. T. Tikhonchuk, C. Labaune, I. V. Sokolov, and G. Mourou, "Relativistic laser piston model: Ponderomotive ion acceleration in dense plasmas using ultraintense laser pulses," *Physics of Plasmas*, vol. 16, p. 083103, 2009.

[41] P. Sigmund, *Particle penetration and radiation effects*. Springer, 2006.

[42] J. F. Ziegler, "Stopping of energetic light ions in elemental matter," *Journal of Applied Physics*, vol. 85, p. 1249, 1999.

[43] J. Lindhard and A. Winther, "Stopping power of electron gas and equipartition rule," *Mat. Fys. Medd. Dan. Vid. Selsk*, vol. 34, no. 4, 1964.

[44] P. Wang, T. M. Mehlhorn, and J. J. MacFarlane, "A unified self-consistent model for calculating ion stopping power in icf plasma," *Physics of Plasmas*, vol. 5, no. 8, 1998.

[45] G. Faussurier, C. Blancard, P. Cosse, and P. Renaudin, "Equation of state, transport coefficients, and stopping power of dense plasmas from the average-atom model self-consistent approach for astrophysical and laboratory plasmas," *Physics of Plasmas*, vol. 17, p. 052707, 2010.

[46] G. Maynard and C. Deutsch, "Energy loss and straggling of ions with any velocity in dense plasmas at any temperature," *Physical Review A*, vol. 26, no. 1, p. 665, 1982.

[47] T. A. Mehlhorn, "A finite material temperature model for ion energy deposition in ion driven inertial confinement fusion targets," *Journal of Applied Physics*, vol. 52, p. 6522, 1981.

[48] T. Peter and J. M. ter Vehn, "Energy loss of heavy ions in dense plasma. i. linear and nonlinear vlasov theory for the stopping power," *Physical Review A*, vol. 43, no. 4, p. 1998, 1991.

[49] E. Nardi, E. Peleg, and Z. Zinamon, "Energy deposition by fast protons in pellet fusion targets," *Physics of Fluids*, vol. 21, p. 574, 1978.

[50] K. A. Brueckner and L. Senbetu, "Stopping power for energetic ions in solids and plasmas," *Physical Review B*, vol. 25, no. 7, p. 4377, 1982.

[51] D. S. Hey, *Laser-accelerated proton beams: Isochoric heating and conversion efficiency*. PhD thesis, University of California, Davis, 2007.

[52] J. Denavit and W. L. Kruer, "Simulation techniques for heavy ion fusion chamber transport," *Physics of Fluids*, vol. 14, p. 1782, 1971.

[53] C. K. Birdsall and A. B. Langdon, *Plasma physics via computer simulation*. McGraw-Hill, 1985.

[54] D. Welch, D. Rose, M. Cuneo, R. Campbell, and T. Mehlhorn, "Integrated simulation of the generation and transport of proton beams from laser-target interaction," *Physics of Plasmas (1994-present)*, vol. 13, no. 6, p. 063105, 2006.

[55] D. R. Welch, D. V. Rose, R. E. Clark, T. C. Genoni, and T. P. Hughes, "Implementation of an non-iterative implicit electromagnetic field solver for dense plasma simulation," *Computer Physics Communications*, vol. 164, pp. 183–188, 2004.

[56] M. E. Jones, D. S. Lemons, R. J. Mason, V. A. Thomas, and D. Winske, "A grid-based coulomb collision model for pic codes," *Journal of Computational Physics*, vol. 123, no. 14, pp. 169–181, 1996.

[57] A. J. Link, *Specular reflectivity and suprathermal electron measurements from relativistic laser*. PhD thesis, The Ohio State University, 2010.

[58] C.-K. Li and R. D. Petrasso, "Charged-particle stopping powers in inertial confinement fusion plasmas," *Physical Review Letters*, vol. 70, no. 20, p. 3059, 1993.

[59] D. Li, "New coulomb logarithm and its effects on the fokker-planck equation, relaxation times and cross field transport in fusion plasmas," *Nuclear Fusion*, vol. 41, no. 5, p. 631, 2001.

[60] G. Faussurier, C. Blancard, and M. Gauthier, "Nuclear stopping power in warm and hot dense matter," *Physics of Plasmas*, vol. 20, p. 012705, 2013.

[61] H. Bichsel, "Shell corrections in stopping powers," *Physical Review A*, vol. 65, p. 052709, 2002.

[62] PROPACEOS, "http://www.prism-cs.com/software/propaceos/propaceos.htm," 2016.

[63] NIST, "http://physics.nist.gov/physrefdata/star/text/pstar.html," 2016.

[64] A. B. Zylstra, J. A. Frenje, P. E. Grabowski, C. K. Li, G. W. Collins, P. Fitzsimmons, S. Glenzer, F. Graziani, S. B. Hansen, S. X. Hu, M. G. Johnson, P. Keiter, H. Reynolds, J. R. Rygg, F. H. Seguin, and R. D. Petrasso, "Measurement of charged-particle stopping in warm dense plasma," *Physical Review Letters*, vol. 114, p. 215002, 2015.

[65] D. P. Higginson, *Ultra-high-contrast laser acceleration of relativistic electrons in solid targets*. PhD thesis, University of California, San Diego, 2012.

[66] M. E. Foord, T. Bartal, C. Bellei, M. Key, K. Flippo, R. B. Stephens, P. K. Patel, H. S. McLean, L. C. Jarrott, M. S. Wei, and F. N. Beg, "Proton trajectories and electric fields in a laser-accelerated focused proton beam," *Physics of Plasmas*, vol. 19, p. 056702, 2012.

[67] T. Bartal, M. E. Foord, C. Bellei, M. H. Key, K. A. Flippo, S. A. Gaillard, D. T. Offermann, P. K. Patel, L. C. Jarrott, D. P. Higginson, M. Roth, A. Otten, D. Kraus, R. B. Stephens, H. S. McLean, E. M. Giraldez, M. S. Wei, D. C. Gautier, and F. N. Beg, "Focusing of short-pulse high-intensity laser-accelerated proton beams," *Nature Physics*, p. 2153, 2011.

[68] I. D. Kaganovich, E. A. Startsev, A. B. Sefkow, and R. C. Davidson, "Controlling charge and current neutralization of an ion beam pulse in a background plasma by application of a solenoidal magnetic field: Weak magnetic field limit," *Physics of Plasmas*, vol. 15, p. 103108, 2008.

[69] A. Friedmana, J. Barnarda, R. Briggsb, R. Davidsonc, M. Dorfc, D. Grotea, E. Henestrozab, E. Leeb, M. Leitnerb, B. Loganb, A. Sefkowc, W. Sharpa, W. Waldronb, D. Welchd, and S. Yub, "Toward a physics design for ndcx-ii, an ion accelerator for warm dense matter and hif target physics studies," *Nuclear Instruments and Methods in Physics Research Section A*, vol. 606, pp. 6–10, 2009.

[70] B. Qiao, M. E. Foord, M. S. Wei, R. B. Stephens, M. H. Key, H. McLean, P. K. Patel, and F. N. Beg, "Dynamics of high-energy proton beam acceleration and focusing from hemisphere-cone targets by high-intensity lasers," *Physical Review E*, vol. 87, p. 013108, 2013.

[71] M. Gauthier, *Experimental study of ion stopping power in warm dense matter: charge-state distribution measurements of ions leaving warm dense matter*. PhD thesis, Ecole Polytechnique ParisTech, 2013.

[72] H. Paul and J. Sacher, "Fitted empirical reference cross sections for k-shell ionization by protons," *Atomic Data and Nuclear Data Tables*, vol. 42, no. 1, pp. 105–156, 1989.

[73] O. Tresca, D. C. Carroll, X. H. Yuan, B. Aurand, V. Bagnoud, C. M. Brenner, M. Coury, J. Fils, R. J. Gray, T. Kuhl, C. Li, Y. T. Li, X. X. Lin, M. N. Quinn, R. G. Evans, B. Zielbauer, M. Roth, D. Neely, and P. McKenna, "Controlling the properties of ultraintense laserproton sources using transverse refluxing of hot electrons in shaped mass-limited targets," *Plasma Physics and Controlled Fusion*, vol. 53, no. 10, p. 105008, 2011.

[74] C. M. Brenner, A. P. L. Robinson, K. Markey, R. H. H. Scott, R. J. Gray, M. Rosinski, O. Deppert, J. Badziak, D.Batani, J. R. Davies, S. M. Hassan, K. L. Lancaster, K. Li, I. O. Musgrave, P. A. Norreys, J. Pasley, M. Roth, H.-P. Schlenvoigt, C. Spindloe, M. Tatarakis, T. Winstone, J. Wolowski, D. Wyatt, P. McKenna, and D. Neely, "High energy conversion efficiency in laser-proton acceleration by controlling laser energy deposition onto thin foil targets," *Applied Physics Letters*, vol. 104, p. 081123, 2014.

[75] T. Bartal, *Investigation of proton focusing and conversion efficiency for proton fast ignition.* PhD thesis, University of California San Diego, 2012.

[76] A. Schreiber, *RGB-color-calibration of radiochromic films.* PhD thesis, Technical University Darmstadt, 2012.

[77] SRIM, "http://www.srim.org," 2016.

[78] A. Morace, C. Bellei, T. Bartal, L. Willingale, J. Kim, A. Maksimchuk, K. Krushelnick, M. S. Wei, P. K. Patel, D. Batani, N. Piovella, R. B. Stephens, and F. N. Beg, "Improved laser-to-proton conversion efficiency in isolated reduced mass," *Applied Physics Letters*, vol. 103, p. 054102, 2013.

[79] D. S. Hey, M. H. Key, A. J. Mackinnon, A. G. MacPhee, P. K. Patel, R. R. Freeman, L. D. V. Woerkom, and C. M. Castaneda, "Use of gafchromic film to diagnose laser generated proton beams," *Review of Scientific Instruments*, vol. 79, p. 053501, 2008.

[80] I. D. Kaganovich, R. C. Davidson, M. A. Dorf, E. A. Startsev, A. B. Sefkow, E. P. Lee, and A. Friedman, "Physics of neutralization of intense high-energy ion beam pulses by electrons," *Physics of Plasmas*, vol. 17, p. 056703, 2010.

[81] D. R. Welch, D. V. Rose, B. V. Oliver, T. C. Genoni, R. E. Clark, C. L. Olson, and S. S. Yu, "Simulations of intense heavy ion beams propagating through a gaseous fusion target chamber," *Physics of Plasmas*, vol. 9, p. 2344, 2002.

[82] J. R. Davies, "Electric and magnetic field generation and target heating by laser-generated fast electrons," *Physical Review E*, vol. 68, p. 056404, 2003.

[83] Y. T. Lee and R. M. More, "An electron conductivity model for dense plasmas," *Physics of Fluids*, vol. 27, p. 1273, 1984.

[84] Y. Sentoku and A. J. Kemp, "Numerical methods for particle simulations at extreme densities and temperatures: Weighted particles, relativistic collisions and reduced currents," *Journal of Computational Physics*, vol. 227, pp. 6846–6861, 2008.

[85] A. P. L. Robinson, M. H. Key, and M. Tabak, "Focusing of relativistic electrons in dense plasma using a resistivity-gradient-generated magnetic switchyard," *Physical Review Letters*, vol. 108, p. 125004, 2012.

[86] J. R. Davies, J. S. Green, and P. A. Norreys, "Electron beam hollowing in lasersolid interactions," *Plasma Phys. Control. Fusion*, vol. 48, pp. 1181–1199, 2006.

[87] B. E. R. Williams, R. J. Kingham, and J. J. Bissell, "Heat flux effects on magnetic field dynamics in solid density plasmas traversed by relativistic electron beams," *Plasma Phys. Control. Fusion*, vol. 55, p. 095005, 2013.

[88] D. Jung, *Ion acceleration from relativistic laser nano-target interaction.* PhD thesis, Ludwig Maximilians University, 2012.

[89] D. Attwood, *Soft X-rays and extreme ultraviolet radiation.* Cambridge University Press, 1999.

[90] T. Ma, A. G. MacPhee, M. H. Key, S. P. Hatchett, K. U. Akli, T. W. Barbee, C. D. Chen, R. R. Freeman, J. A. King, A. Link, A. J. Mackinnon, D. T. Offermann, V. Ovchinnikov, P. K. Patel, R. B. Stephens, L. D. V. Woerkom, B. Zhang, and F. N. Beg, "Determination of electron-heated temperatures of petawatt laser-irradiated foil targets with 256 and 68 ev extreme ultraviolet imaging," *Review of Scientific Instruments*, vol. 79, p. 093507, 2008.